UiO : University of Oslo

Christopher Friedemann

Simulations of two-phase gas-liquid flow in concentric and eccentric annuli at 0 to 90 degrees inclination using the volume of fluid method

Thesis submitted for the degree of Philosophiae Doctor

Department of Mathematics
The Faculty of Mathematics and Natural Sciences

Institute for Energy Technology

2021

Series of dissertations submitted to the
The Faculty of Mathematics and Natural Sciences, University of Oslo
No. 2377

ISSN 1501-7710

Cover: Hanne Baadsgaard Utigard.
Print production: Reprosentralen, University of Oslo.

Preface

This thesis is submitted in partial fulfillment of the requirements for the degree of *Philosophiae Doctor* at the University of Oslo. The research presented was performed at the University of Oslo and IFE, under the supervision of professor Mikael Mortensen, Dr. Jan Nossen, and Dr. Murat Tutkun. The work was carried out at the University of Oslo and Institute for Energy Technology (IFE), and concerns computational fluid dynamics of two-phase flow within an annulus. The simulations are verified through experimental data collected at IFE; the author did not partake in the experimental setup nor data acquisition of the experimental data.

The thesis is a collection of three papers, presented in chronological order of writing. An introductory chapter precedes the journal papers, describing the motivation and background of the thesis and ties the papers together. I am first author on all papers, and was involved in the computational work as well as analysis of experiments presented in the papers, but did not perform the experiments or partake in setup of them.

This work was supported by the Norwegian Research Council through grant 255481.

Christopher Friedemann
Oslo, February 2021

Acknowledgements

To start it all off, I want to thank my supervisors Mikael Mortensen, Jan Nossen, and Murat Tutkun, for their diligence and hard work in each their ways. Mikael has supported me through not only technical difficulties, starting on the very first day, but through thorough knowledge and methodology related to computational fluid dynamics. He also allowed me the freedom and trust to take the project in a new direction, when I decided to swap out the original code for OpenFOAM.

Jan Nossen has provided invaluable input on subjects outside my background, for example, analysis of experiments and flow regime classification methods. I especially appreciate all the knowledge and experience he has with scientific writing, which I have benefitted greatly from. I want to thank Murat Tutkun for always having an open door for questions. Taking time to formulate well thought out answers to all manner of problems and many a conversation spent in the hallways of IFE when I was wondering about some specific aspect of a flow regime or model. If there is one thing I regret, it is not spending more time at the IFE office early on in the Ph.D. process. Jan, Murat, and perhaps especially Roberto Ibarra taught me a lot about multiphase flow, scientific writing and provided me with a new enthusiasm toward the end of the project.

Apart from my supervisors, I would like to express my appreciation to my friends and colleagues at UiO and IFE that helped me overcome problems as they occurred, in particular, Johan Kristian Sveen, Petter Vollestad, Diako Darian, Anis Ayati, Reyna Gutierrez and Jean Rossault.

Outside academia, I would like to thank my friends, Mikkel Stokke, Trond Johannesen, Bjørn Anders Fossum, and Marius Bratland, for keeping me sane and distracting me with social interactions, as well as Matej Murín and José F.R. Hernández for their debugging and coding expertise.

Siri, Dan, Cathrine and Carl-Erik Friedemann for their support and sometimes overeager enthusiasm for my work, and my girlfriend, Rebecca Wall, for her patience and understanding during these 3.5 years we had to spend apart.

Christopher Friedemann
Oslo, February 2021

List of publications.

There are 3 published articles included in this dissertation, in addition to the 3 included articles, included in the Ph.D. work, but omitted from the dissertation is 1 conference article. As a precursor to the list of publications included in this dissertation, it is important to clarify my contribution as main author. In each publication, I was responsible for the conceptualization of the published work, the design, execution, setup and analysis of the simulations, the analysis of the available experimental data, and also the drafting of the manuscript and any subsequent revisions. The second paper is adjoined with an author statement. In regards to the distribution of responsibilities for papers 1 and 3, they follow the same distributions as the second publication.

Papers included in the dissertation.

Paper I

Friedemann, C. and Mortensen, M. and Nossen, J. "Gas-liquid slug flow in a horizontal concentric annulus, a comparison of numerical simulations and experimental data". In: *International Journal of Heat and Fluid Flow.* Vol. 78, (2019), DOI: 10.1016/j.ijheatfluidflow.2019.108437.

Paper II

Friedemann, C. and Mortensen, M. and Nossen, J. "Two-phase flow simulations at 0-4^o inclination in an eccentric annulus". In: *International Journal of Heat and Fluid Flow.* Vol. 83 (2020), DOI: :/10.1016/j.ijheatfluidflow.2020.108586.

Paper III

Friedemann, C. and Mortensen, M. and Nossen, J. "Two-phase co-current flow simulations using periodic boundary conditions in horizontal, 4, 10 and 90^o inclined eccentric annuli, flow prediction using a modified interFoam solver and comparison with experimental results". In: *International Journal of Heat and Fluid Flow.* Vol. 88 (2021) DOI: :10.1016/j.ijheatfluidflow.2020.108754.

Relevant papers not included in the dissertation

Paper IV

Friedemann, C. and Mortensen, M. and Nossen, J. "Multiphase flow simulations in an annulus configuration". Appeared in *MekIT'17 - Ninth national conference on Computational Mechanics. International Center for Numerical Methods in Engineering (CIMNE)*, URL: https://ife.brage.unit.no/ife-xmlui/handle/11250/2469674

Contents

Preface **i**

Acknowledgements **iii**

List of publications. **v**

Contents **vii**

List of Figures **ix**

1 Introduction **1**
1.1 Motivations 1
1.2 Multiphase flow 3
1.3 Multiphase flow in an annulus 7
References 15

2 Experimental campaign at Institute for Energy Technology **21**
References 24

3 Numerical Method in OpenFOAM **27**
3.1 Description of the InterFoam solver 32
3.2 Numerical and experimental considerations 35
References 37

4 Objectives, findings and future perspective **39**

Papers **44**

I Gas-liquid slug flow in a horizontal concentric annulus, a comparison of numerical simulations and experimental data **45**

II Two-phase flow simulations at $0 - 4^o$ inclination in an eccentric annulus **61**

III Two-phase co-current flow simulations using periodic boundary conditions in horizontal, 4, 10 and 90^o inclined eccentric annuli, flow prediction using a modified inter-Foam solverand comparison with experimental results **83**

List of Figures

1.1 Common flow regimes in multiphase pipe flow 3
1.2 Gradual transition of flow regime along a vertical pipe 4
1.3 Flow regime maps of air-water and effect of geometry on oil-gas flow regime 5
1.4 Pressure drop empirical model performance in a vertical pipe . . 6
1.5 Concentric and eccentric annulus geometry 8
1.6 Hydrocarbons entering the riser annulus 9
1.7 Shape of Taylor bubble in a vertical concentric annulus 11
1.8 Effect of eccentricity on friction factor on single-phase flows in annulus 12

2.1 Horizontal flow-loop at Institute for Energy Technology with measurement devices 21
2.2 Inclined flow-loop at Institute for Energy Technology with measurement devices 22

3.1 OpenFOAM multiphase solvers 27
3.2 Hexahedral mesh for concentric annulus 31
3.3 Case structure of interFoam solver 32

Chapter 1

Introduction

1.1 Motivations

The purpose of this thesis is to explore, study, and analyze two-phase flow in an annulus by comparing computational fluid dynamics simulations using OpenFOAM with experimental data gathered at Institute for Energy Technology. The oil and gas industry has, for many years, relied upon experimental data and correlations built on empirical methods to predict flow behavior within wells, pipelines, and risers. Through vast data-sets, models are developed to predict flow regime, pressure behavior and flow rates. When carefully and methodically applied, these correlations are reliable and can give valuable information about flow behavior inside a flow conduit.

In the petroleum industry, empirical models are used to estimate maintenance schedules and predict operating loads of pipelines. In order to be confident that the model represents physical behavior, it is extremely important that the prediction methods are accurate and robust. However, many of the models, which were developed in the 70s and 80s, have a limited range of application due to their sensitivity to geometry, fluid properties, fluid fractions, and flow regimes. When improperly applied, an empirical model may incorrectly predict flow behavior, and falsely predict the flow regime, predicting for example stratified or annular flow rather than slug flow, which is identified by intermittent large pressure spikes and liquid bodies which cover the cross-section. Equally problematic and common are cases where slug flow is falsely predicted. If slug flow is expected, measures can be taken to reduce pipeline fatigue by implementing diverging pipe segments or slug catchers (flow separators that can accommodate large slugs) or dynamically regulate valves to minimize pressure loads and reduce the risk of malfunction. Slug control through manual or regulated valves is a vast topic and is almost considered its own field of study, and there are undoubtedly many other possible approaches.

When a new petroleum well is established, the fluid compositions, well-configuration, and local conditions may effect how accurate the available models‘ predictions are. Due to the high-risk nature of the petroleum industry and the detrimental after-effects of an oil-leak, it is vital to have accurate and robust models with a wide range of possible applications. When we combine these factors with the current advances in both computational resources and available computational fluid dynamic (CFD) tools, then the time has never been better to explore CFD as a tool for prediction of flow behavior, and pipeline analysis. The strength of CFD is that, in theory, the models are less sensitive to fluid compositions, and advanced geometries can be studied through careful domain modeling. One of the main limitations to the accuracy of CFD is proper

mesh resolution and the codependent solution time; however, this factor is at least partially overcome using modern computing clusters. Furthermore, the investment required for the petroleum industry to adopt CFD models instead of, or in combination with current models, should be relatively small when leveraged against the potentially vast improvements to safety, accuracy, and adaptability. Lastly, CFD can be used to further improve existing models predictions if the simulations are proven accurate enough to be considered alongside field data.

In the 2010 Macondo accident, flow occurred through an annulus (BP, 2010; DHSG, 2011; DNV, 2011) releasing what was initially predicted by currently available models as 1,000 barrels per day. Due to a lack of applicable models, several months passed before The National Oceanic and Atmosphere Administration (NOAA) received the more accurate estimate of barrels released per day, totalling 62,000. This thesis will represent a step toward limiting future events such as this, and improving current multiphase flow predictions in an annulus geometry.

The thesis is structured into four different chapters. The first chapter discusses the motivation for the work and provides an introduction to multiphase flow in a conventional pipe as well as within an annulus. The second chapter provides a short walk-through of the experimental setup detailing how the data used for verification of the simulations was acquired; please note that the author did not contribute to the experiments, but extracted and analyzed available data for specific cases. The third chapter is focused on the numerical solver utilized for the simulations. Although not exhaustive, the chapter will provide the reader with enough information to understand the basics of the methods used. The fourth chapter consists of a short introduction and provides relevance for the 3 journal papers before each paper is presented individually in the chronological order that they were written.

1.2 Multiphase flow

The definition of multiphase flow and thereby multiphase pipe-flow is any flow in which a combination of two or more phases are present. The compositions of these fluids are commonly presented as gas-liquid, liquid-liquid, and liquid-solid (G. Hewitt, 2010). Depending on the flow rates, holdup fractions, geometry, and fluid properties, different patterns known as flow regimes will develop (G. Hewitt and Roberts, 1969; Taitel and Dukler, 1976). Furthermore, based on the pressurization and temperature of the system, a streamwise variation of flow regimes may be observed. When the pressure decreases, gas particles are released from the liquid, leading to the formation of bubbles which may eventually be followed by the complete separation of the phases (Hasan and Kabir, 1988).

Flow regimes are predominantly determined through visual observations (H. Wu et al., 2001) which lead to varying definitions based on the observer's subjective opinion. However, researchers have developed a general consensus about the appearance and behavior of the most commonly observed flow regimes, some of which are visualized in Fig. 1.1. These common flow regimes are

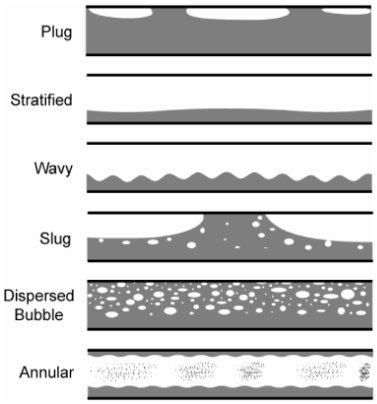

Figure 1.1: Typical gas (white)-liquid (dark)flow regimes observed in horizontal and inclined multiphase pipe flow (Ghajar, 2005).

observed under a wide range of conditions, and can develop abruptly through physical interactions with obstructions, or gradually through streamwise pressure variations. A gradual transition from smooth stratified flow to slug flow can occur through the development of Kelvin-Helmholtz instability and wave merging. In two-phase pipe-flow, the onset of Kelvin-Helmholtz instability occurs when the shear forces between two initially stratified fluids traveling at different velocities overcome the dampening effects of gravity and surface tension. As the instability grows, waves form followed by a process known as wave merging in which waves of gradually increasing length and amplitude are formed. Eventually these waves develop into a slug or plug by forming a large liquid body which covers the cross-section.

The plug flow regime is defined by a complete or near-complete lack of gas entrainment within the liquid phase (Fig. 1.1). The liquid phase accumulates into large liquid bodies void of gas penetration, these liquid bodies are commonly known as plugs. While the gas phase typically coalesces and forms large gas pockets, these gas pockets are more specifically known as Taylor bubbles. Taylor bubbles were first described in *"The mechanics of large bubbles rising through extended liquids and through liquids in tubes"* as bubbles that seperarate segments where the liquid phase occupies the entire cross-section, manifesting as an intermittent repeating flow regime by (Davies and Taylor, 1950).

Slug and plug flow share several characteristics, including Taylor bubbles, large and sudden pressure spikes that can inflict significant stress and deterioration of a pipeline (Rogero, 2009), and intermittent liquid bodies that cover the cross-section (Fig. 1.1). Due to the similarities between the slug and plug flow regimes, they can be hard to differentiate, and are often grouped together in literature. However, slug flow can be differentiated from plug flow by an increase in the gas entrapment within the liquid (Bertola, 2000), and the size and velocity of the Taylor bubbles (Guilizzoni et al., 2019; Schulmberger, 2020).

An annular flow regime is recognized by a low liquid holdup (α) that forms a slow-moving film along the pipe walls, with the core of the annular regime mostly occupied by high superficial velocity gas (u_{sg}), and liquid droplets. Superficial gas velocity is well known as

$$u_{sg} = (1 - \alpha) \cdot u_g, \tag{1.1}$$

describing the velocity at which the mass flux of gas is the same as if the pipe was only filled with gas.

A dispersed bubble flow regime, which is also known as homogeneous bubble flow, is characterized by a high liquid holdup fraction, and a relatively high superficial liquid velocity (Shaikh and Muthanna, 2007). The gas bubbles are small and evenly distributed with only limited variations in both bubble size and motion. Although, a direct transition between the dispersed bubble and the annular flow regime is possible at sufficiently high superficial velocities (Fig. 1.3), an intermittent flow regime (slug/plug) may separate the two flow patterns (Fig. 1.2).

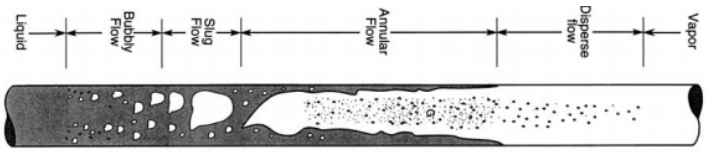

Figure 1.2: Gradual transition of flow regime in a vertical pipe. Adapted from Brennen (2005)

In addition to the previously discussed regimes, there are several other flow regimes and subsets of flow regimes that exist and will not be discussed in-depth in this thesis. Some examples include rolling waves, misty (Hoogendoorn, 1959) and wispy annular flow (Bennett et al., 1965), and churn flow. The latter is often described as an extremely chaotic regime, lacking consistent characteristics and existing as a transitional flow between the annular and slug flow regimes (F. Hewitt, 2012).

By collecting data for a variety of flows and superficial velocities, researchers have been able to develop flow maps for numerous specific geometries and fluid compositions. A flow regime map (Fig. 1.3) illustrates the transition points between flow regimes as well as describe the superficial gas and liquid velocities that limit each flow regime. Flow regime maps are valuable and serve

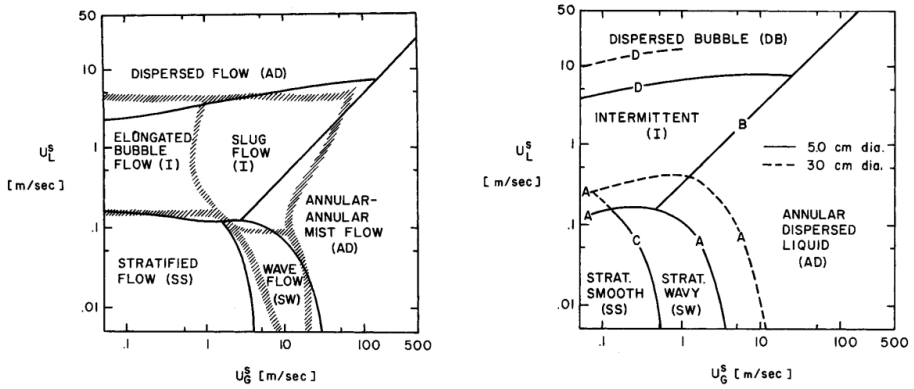

Figure 1.3: Flow regime maps of air-water (left) and oil-gas (right), with shaded fit to Mandhane model (Mandhane et al., 1974) (left) and effect of geometry (right). Adapted from: Taitel and Dukler (1976))

an important purpose; however, in order to accurately predict flow behavior, flow regime maps are limited to specific fluid compositions, geometries, and inclinations (B. Wu et al., 2017). When the pipeline falls outside the scope of the experiments or field-data originally used to build the flow regime maps, the model is likely to be inaccurate, as illustrated by Taitel, and shown in Fig. 1.3. Taitel indicates how there is a small but noticeable inconsistency between the data set and the data correlation applied, illustrated through the fit between the shaded and solid sections. Taitel further illustrates how pipe geometry also affects potential transition points and the overall flow map as seen in what occurs when overlapping data for 5.0 and 30 cm diameter pipes. This comparison demonstrates that the transition points shift to higher superficial gas and liquid velocities in the larger diameter pipe.

For a typical pipeline, visual flow regime identification is at best complicated, and at worst impossible. Therefore, significant time, money, and research is

allocated to the prediction and identification of flow regimes through non-visual means. There is a multitude of correlations and flow regime maps for different fluid compositions, geometries, and inclinations such as Speddings's map for air and water (Spedding and Nguyen, 1980), Taitel's correlation model and map for predicting flow regime transitions in horizontal and near horizontal gas-liquid flow (Taitel and Dukler, 1976), as well as several other well-known maps including Baker's original contribution from 1953 related to the design of oil and gas pipelines (Baker, 1953).

Flow regimes play an essential role in several crucial aspects of oil and gas transport, particularly pressure variations. Pipe pressure varies as an effect of streamwise location, and as a function of the flow regime. Therefore, flow regime maps are often used in combination with a mechanistic model or empirical correlation in order to predict the pressure behavior.

There are several well known and extensively utilized mechanistic and correlation-based pressure drop models throughout the industry. Beggs and Brill (1973) is perhaps the most well-known correlation and is reportedly applicable to different pipe diameters and a wide range of flows, including both inclined and vertical. Additional well known models include the mechanistic models developed by Aziz and Govier (1972) and Petalas and Aziz (2000) as well as the correlation developed by Hagedorn and Brown (1965). More recent developments have seen a shift in focus toward the utilization of artificial neural networks to predict the pressure loss within a pipeline. Of these, there are at least two such models known to the author of this thesi including those developed by Osman et al. (2005) and by Jahanandish et al. (2011), although there are undoubtedly many more.

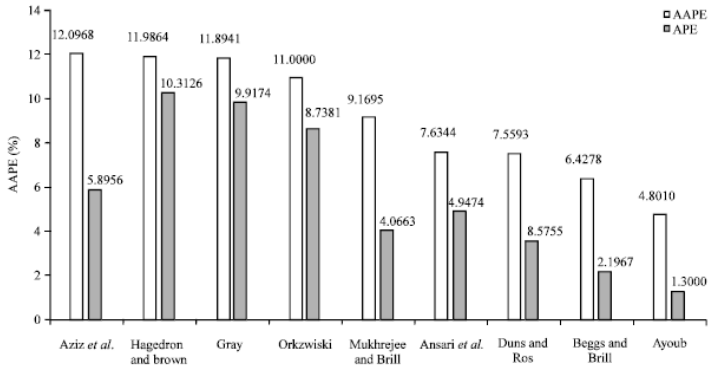

Figure 1.4: Performance of pressure drop models in %, average absolute relative error (left), average relative error (right). Adapted from Ahmed and Ayoub (2014)

Fig. 1.4 illustrates the findings from a pressure drop model performance analysis for mechanistic and correlation based models in a vertical well (Ahmed and Ayoub, 2014). The above models were also evaluated against their own

(Ayoub) model (Fig. 1.4). The author believes the Ayoub model to be a predecessor of the previously mentioned model in Osman et al. (2005). As shown in Fig. 1.4, the average performance of all models is relatively accurate, with errors within 15 % regardless of the metric utilized.

All models mentioned share a common dilemma; when the model is applied to a flow which falls outside the model's intended scope, there is a large degree of uncertainty in the results. For correlation-based models, the uncertainty may come from pipe diameters, inclinations, and fluid properties. Mechanistic models are often considered more robust than correlation models because they are based on a mathematical approach; however, mechanistic models share the same issue of model fit. The uncertainty of a mechanistic model often manifests through requiring prior knowledge of the flow regime. As mentioned, flow regimes are notoriously hard to quantify, and are often open to interpretation. Without utilizing models that are independent of a flow regime, these problems will continue to persist. The success of an Artificial neural networks (ANN), alternatively, is both dependent and limited by the training the system receives. Although ANN's are an exciting development, it is speculated whether the same issues that are encountered by correlations and mechanistic models, will also manifest in ANN's, leading to the question of whether or not there is enough available data to properly train the ANN to robustly and accurately function for any conceivable flow (Ahmed and Ayoub, 2014).

Considering the risk, cost, and environmental impact that a catastrophic failure in the petroleum industry would have, it is crucial to develop other means of predicting flow behavior, particularly pressure drop, flow regime, and slug frequency, among other equally important aspects. While available empirical models have been both helpful, and beneficial, in order to be able to improve predictions of multiphase flow behavior, new models must be developed that do not rely solely on the available data. These new models with modern solution methods should strive to rely on the underlying physical interactions, therefore improving adaptability to any flow, inclination, or geometry, such as an annulus.

1.3 Multiphase flow in an annulus

The purpose of this thesis is to study multiphase flow within an annulus through computational fluid dynamics using OpenFOAM. An annulus consists of an inner and outer cylinder. The cylinders' diameters and centroids define the eccentricity of the configuration, as shown in Fig. 1.5, and defined by Eq. (1.2).

$$E = \frac{d}{R_o - R_i}. \tag{1.2}$$

When the distance between centers (d) is maximized, the annulus is considered fully eccentric (E=1.0), and when the centers coincide, the annulus is considered concentric (E=0). The eccentricity of the annulus plays an important factor in flow development, affecting the fluid-fluid interfacial area, and influencing the friction factor.

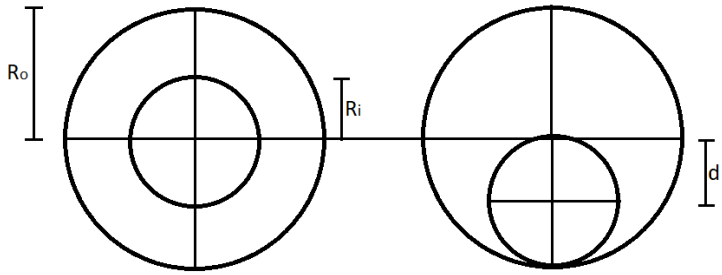

Figure 1.5: Concentric annulus (left) and fully eccentric annulus (right), R_i =inner radius, R_o =outer radius, d =distance between centroids

Annuli and closely related geometries are utilized in a vast array of industries including; petroleum (Hanks and Bonner, 1971; Ju et al., 2008; Rodriguez and Baldani, 2012), computer electronics (Iyer and Vafai, 1998), nuclear, and aerospace. Within these industries, applications of annuli are found in deviated and under-balanced wells (Rooki and Rakhshkhorshid, 2017; Sun et al., 2013), nuclear rod bundles (Choueiri, 2014), reactor cores (Inaba et al., 2005), heat transfer in annular heat pipes (Faghri, 1989), heat sinks (Yovanovich et al., 1988) and combustion engines (Mark and Selwyn, 2016). Due to the strong physical interactions present in multiphase flow, there is also an inherent risk. A malfunction within the combustion chamber of a jet engine (Hennecke et al., 2017), a failure of a cooling system in a nuclear power plant, or an accident at an oil and gas well, such as the well-known Macondo incident (BP, 2010), during which hydrocarbons leaked into the wellbore annulus (Fig. 1.6), are all examples of events that have already occurred or may occur in the future due to the strong physical interactions present in multiphase flow.

In an effort to determine whether the Macondo incident was preventable, and to reduce the likelihood of a similar disaster, the events prior to and the cause of the Macondo incident were thoroughly documented by British Petroleum (BP, 2010), Det Norske Veritas (DNV, 2011), National Oceanic and Atmospheric Administration (NOAA), National Commission on the BP Deepwater Horizon Oil Spill and Offshore Drilling (BP Deepwater Horizon Oil Spill and Drilling, 2011) and Deep Horizon Study Group (DHSG, 2011).

As summarized by both the independent and internal investigations, there were a series of events which led to flow leaking through an annulus, as shown in Fig. 1.6. According to BP's internal incident report, hydrocarbons entered the riser and flowed into an annulus upstream of the blow out preventer (BOP). There were at least two blow out preventers, of which at least one failed. In combination with other factors, the failure of the BOP led to flow moving through the annulus and an eventual leak (BP, 2010; BP Deepwater Horizon Oil Spill and Drilling, 2011; DHSG, 2011; DNV, 2011). As discussed, multiphase flow models are notoriously finicky with regards to geometry, fluid composition, and inclination. Due to several factors, including the annular geometry within the wellbore, it is

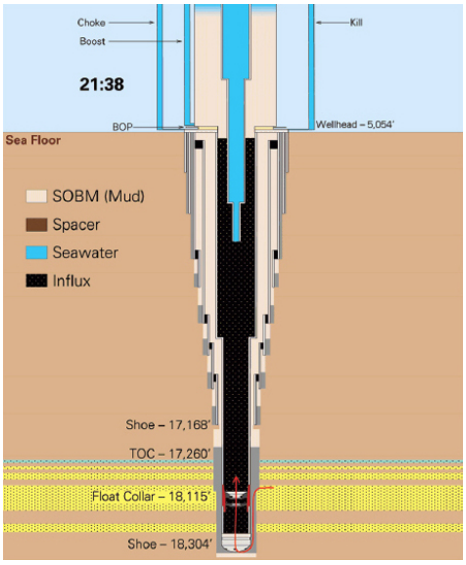

Figure 1.6: Hydrocarbons entering the annulus in the riser of the Macondo well. Adapted from BP (2010)

unlikely that the available models and methods utilized were sufficient enough to analyze the Macondo incident while it was occurring, leading to the discrepancies in leakage estimates that were proposed throughout the extensive timeline of the event. BP initially estimated a leakage of 1,000 barrels of oil per day at the start of the event. Several months later, the official estimate increased significantly to 62,000 barrels of oil per day (McNutt et al., 2012). Numeroust methods were utilized to generate ongoing approximations of oil leakage throughout the event, including particle image velocimetry, well pressure modeling, airborne particle measurements, and surface collection. The significant discrepancies that were presented between the initial and final estimates, underlines the importance of the subject matter within this thesis, exploring CFD as an option for multiphase flow modeling in annuli.

The flow regimes that occur during two-phase flow within an annulus share many similarities with their conventional hollow pipe counterpart, both with similar characteristics and regimes (Hasan and Kabir, 1992); however, due the addition of the inner cylinder within the annulus, the superficial velocities that define the boundaries of each flow regime within the annulus and transition points between regimes can shift drastically (Kiran et al., 2020; Ozar et al., 2008). Taitel referenced this difference seen within an annulus when he discussed the impact of pipe diameter in his early work on flow regime mapping and correlations (Taitel and Dukler, 1976). This shift of the superficial velocities which define the bounding region for each flow regime within an annulus occurs due to several factors. The Reynolds number, which is a function of the hydraulic

diameter, the pressure losses, which are a function of the friction factor, and the previously mentioned fluid-fluid interfacial area, are three examples which depict why flow in annuli may behave drastically different than that of flow in a hollow pipe at similar superficial velocities. While it is difficult to calculate each of the above's impact on overall flow behavior, together they cause a significant change to the physical interactions and can alter the resultant flow regimes when compared to seemingly similar hollow pipe configurations.

As previously mentioned, annuli and hollow pipes can share many of the same characteristics of flow regimes. In annuli, annular flow is characterized by a liquid film on the inner and outer cylinder walls, as well as a high velocity gas core, which is responsible for the majority of the mass flux. Although similar to a conventional hollow pipe, the inner cylinder within an annuli affects the fluid distribution, shaping the gas core as an annulus instead of as a cylinder.

It is well established that annular flows typically occur at low liquid holdup fractions. In a study of annular flow regimes, encompassing 29 different holdup fractions, it was found that the annular flow regime did not occur at lower than 65 % void fraction (Cioncolini and Thome, 2012). Typically, the liquid content of the gas core itself is no more than 20-25 % (Zeigarnik, 2010); however, due to the increase in wall surface area within an annulus, it is possible that the void fraction range for the annular flow that occurs is increased.

There are very few published studies on annular flow within an annulus and at the time of this thesis, the most recent publication studies vertical concentric annulus at high superficial gas velocities (9.2-47.2 m/s) (Kiran et al., 2020). The topics covered in this publication include comparisons of computational and experimental void fractions, and pressure gradients. Through the simulations run in Fluent, the mean error of the pressure gradients and void fractions were found to be within 20% of the experimental data. It is the author's understanding that Kiran's simulations were initialized to encourage annular flow through the boundary conditions, by using separate annular inlets for the gas and liquid phase. While these boundary conditions limit the direct applicability of these simulations for flow predictions, the close agreement between computational and experimental data highlight the value that CFD holds in its use as a flow modeling tool.

Among the many multiphase flow regimes studied in annular geometries, slug flow is one of the most commonly researched, due to its large pressure and velocity variations and negative impact on pipeline longevity. Slug flow in annuli shares many characteristics with its hollow pipe counterpart, including large pressure and velocity variations and liquid bodies that cover the cross-section. It is theorized that the typical axis-symmetric Taylor bubble observed in a hollow pipe may also be found in annuli with sufficiently smaller inner cylinder diameters and low superficial velocities (Hills and Chéty, 1998); however, in practice these are rarely found in annuli (Kelessidis and Dukler, 1990). Instead, in inclined or vertical annuli the Taylor bubble includes a liquid passageway. This passageway is not present in a hollow pipe, demonstrating that the shape of the Taylor bubble is visibly affected by the presence of an interior cylinder. In a hollow pipe, the Taylor bubble resembles a bullet with a symmetrical outline,

and a liquid coats the walls creating a thin film. This film is significantly slower than the Taylor bubble, and has the potential to flow in reverse. Alternatively, within an annulus, the Taylor bubble is made up of two wings that wrap around the interior cylinder (1.7), leaving a small gap which forms the liquid passageway (Caetano, 1985). This Taylor bubble configuration described in Caetano (1985) thesis was later referred to as an asymmetric Taylor bubble (G. Das et al., 1998).

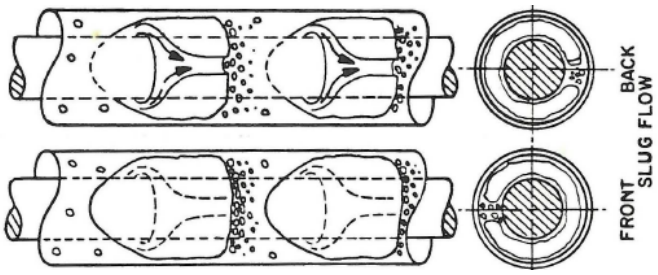

Figure 1.7: Taylor bubble shape in vertical concentric annulus configuration with stream lines indicating the liquid flow direction with respect to the Taylor bubble. Adapted from Caetano (1985)

As Caetano discovered, the Taylor bubble does not wrap completely around the interior cylinder when the annulus is concentric. Due to the asymmetry of the Taylor bubble in an annulus, liquid flows through the passageway between the two wings and along the walls (Fig. 1.7). This liquid that covers the walls and moves through the passageway between the wings, travels at a lower velocity than the Taylor bubble, and at high inclinations the liquid may be counter-current to the Taylor bubble, commonly referred to as back-flow. The altered shape of the Taylor bubble within an annulus, when compared to that within a hollow pipe, is an example of how flow behavior is affected by the annulus geometry, and highlights why conventional flow models for hollow pipes may not be applicable to the annulus geometry. These seemingly small changes to flow regimes are recurrent phenomena within an annulus and can occur based on the respective position (eccentricity) of the two cylinders, as Eyo highlights in his work on gas-liquid flow regimes in horizontal annuli (Eyo and Lao, 2019). The effect of the interior cylinder within an annulus may also contribute to the formation of rarely observed and lesser known flow regimes unique to the annulus geometry, including the wavy slug flow observed in Eyo's work. In an annulus, when compared to a hollow pipe, the presence of an interior cylinder inflicts many small differences on the flow regime. These small differences, alter the regime in such a way that empirical models based on hollow pipes may not predict the regime accurately and add significant uncertainty to commonly used pressure and hold up models when applied to an annular pipe.

There are also many less prominent differences which fundamentally affect flow development in annuli, including how the introduction of the interior pipe within an annulus affects the friction factor. Based on a model of hydraulic

diameter, the friction factor in a concentric annulus will always be greater than that in a hollow pipe, while a fully eccentric annulus will always have a lesser friction factor than in a hollow pipe with the same hydraulic diameter (Caetano, 1985; Denton, 1963).

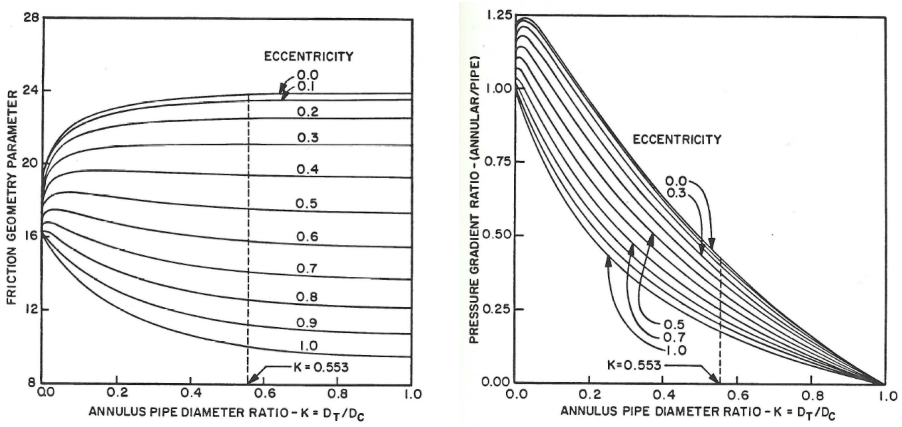

Figure 1.8: Effect of eccentricity on friction factor (left) and pressure gradient (right) of single-phase annulus flows. Adapted from: Caetano (1985))

Caetano discovered that when the diameter ratio (D_i/D_o) of the annulus approaches 0, the friction geometry parameter approaches 16 (Fig. 1.8), which is the theoretical value for the friction geometry parameter within a hollow pipe. At increasing pipe diameter ratios , with an eccentricity of 0.5 or below, an annulus will always have a higher friction geometry parameter than a hollow pipe. While these presented relationships are calculated for single-phase flows, the relationships should be comparable in an identical annulus for multiphase flow. Furthermore, due to the decreasing friction geometry parameter, the pressure gradients are reduced within a fully eccentric annulus when compared to a concentric configuration (Kelessidis, Dalamarinis, et al., 2011).

Most research pertaining to single phase and multiphase flow in an annulus was conducted experimentally in the 60's, 70's and 80's; however, beginning in the early 2000's, there was an increase in publications on this topic, a trend which has sustained interest to present day, possibly due to the after-effects following the 2010 Macondo incident. Among these publications, the transition points of inclined flows in an annular channel were studied, where it was discovered that the transition onset between plug to slug / bubbly flow occurs at lower superficial gas velocities as the inclination increases (Wongwises and Pipathattakul, 2006). In the same publication several other less significant but similar changes related to the transition between dispersed bubbly flow to bubbly/plug flow, bubbly/plug flow to bubbly/slug–plug flow, and bubbly/plug flow to plug flow were also found. For all other flow regimes, the transitions occur at a higher superficial gas velocity

while inclination is increased.

Ozar et al. (2008) studied the flow structures of gas-liquid flow in an annulus experimentally and compared the visually determined flow regimes that occurred during their experiments with previously published flow regime maps. Based on the gathered data a new correlation was developed for determining a fluid distribution parameter, which is needed by many models to predict the void fraction of two-phase flows. The flow regime data points found in the study by Ozar et al. (2008) were then compared to commonly used flow regime maps, including those by G. Das et al. (1999), Kaichiro and Ishii (1984), and Kelessidis and Dukler (1989), where it was found that while several of the flow regime maps had matching regions, Ozar et al. (2008) argued that the models which were compared were insufficient for specific flows. The Kaichiro model over-predicts the superficial velocities for transition from slug to churn which, Ozer theorized that the over-prediction occurs because the model is constructed for hollow pipes, and therefore does not account for the geometric influence of the annulus. Both the Kelessidis and Das models were originally intended for annuli; however, continued to over-predict the superficial gas velocity for the transition point between slug and churn. The discrepancies found between the previously published predictive flow regime models and those in the experiments conducted by Ozar et al. (2008) and Wongwises and Pipathattakul (2006), underlie the importance of developing a robust and adaptable method for prediction of flow behavior, specific to annular geometries. These studies by Ozar et al. (2008), show the limitations of flow regime correlations and highlight the flow variance that occurs due to inclination, further highlighting the limitations that occur when attempting to generalize empirical models.In a publication related to Ozar's study, air-water two-phase flow in a vertical annular channel was compared to previously existing flow regime maps, where it was discovered that the static flow regime maps were insufficient for this type of air-water two phase flow (Jeong et al., 2008) . A new method was then proposed using interfacial area transport for flow modeling, it was also suggested that the new method could be applied for closure modeling of CFD models (Jeong et al., 2008).

There are very few relevant studies throughout the literature examining flow in annuli through CFD. One of few relevant studies, is the computational work by A. Das and P. Das (2010), which discusses the modeling and transition points of bubbly flow in vertical annuli using population balance techniques. The research was based on a two-fluid model using an Eulerian-Eulerian approach with cylindrical coordinates. With the Eulerian approach employed, the mass and momentum conservation equations are solved separately for each phase, which naturally increases the solution time when compared to a single equation approach employed in mixture models such as volume of fluid. While the A. Das and P. Das (2010) model performs adequately when compared to their experimental data set, they deliberately mention that narrow annuli or strong deviations from the vertical configuration is likely to drastically limit the model's performance.

More recently, Sorgun et al. (2011) and Kiran et al. (2020), investigated the pressure losses of two-phase annulus flows using ANSYS CFX and Fluent

respectively. Both studies reported an accuracy of within 20 % for their featured parameters of either frictional pressure losses (Sorgun et al., 2011) or mean pressure gradient (Kiran et al., 2020). In addition, in the study conducted by Kiran et al. (2020), the void fraction of the studied flows were within 20 % of the experimental value. Kiran et al. (2020) reduced the domain in their study to reduce computation time, by applying two symmetric boundary conditions, across the y-plane and the x-plane to form a quarter-pipe geometry. This adjustment holds sound for a concentric orientation when studying annular and churn flows, due to the axis-symmetry of annular flows and the chaotic nature of churn flow.

Among other recent contributions to the field of annulus flow, are improvements of the the mathematical expressions for time-averaged velocity and mixed-mean velocity of single-phase flows in an annulus (Kaneda et al., 2003). These expressions are based on a theoretical approach, and nearly free of empiricism. Unfortunately, because these expressions are derived for single-phase flows they are not directly applicable to our work; however, these expressions do represent a shift away from standard empirical models, and may prove valuable for multiphase flows in the upcoming future. There have been many further advancements in single-phase flow, including the direct numerical simulations using a spectral method to study turbulent flow and heat transfer in an eccentric annulus (Nikitin et al., 2009). Mizushima et al. (2001) studied natural convection in annuli with high inner to outer cylinder diameter ratios and found dual steady state solutions for Reynolds numbers higher than the critical value. Escudier et al. (2002) studied the effect of eccentricity and rotation of the inner cylinder on laminar flows in an annulus discovering that the fanning friction factor times Reynolds number ($f \cdot Re$) was increasing for high and low eccentricities but decreasing for intermediate eccentricities ($0.2<E<0.9$) for non-Newtonian fluids, it was suggested that this occurs due to the combined effect of eccentricity and inner cylinder rotation. This discovery could have some beneficial applications in drilling operations for the petroleum industry when the location of the drill bore is unknown and varying.

The majority of the available literature studying flows within an annulus is experimental, with very few published works using computational methods. Of these studies using computational methods, most are focused solely on single-phase flows. Due to the complexity of multiphase phase flow and the computational resources required to extensively study the geometry of the annulus, there are very few publications, apart from the author's own works, studying two-phase annulus flow computationally. Because of this complexity, it is no surprise that most of the computational studies examine low velocity single phase flows or as in the case of Kiran's work, the geometry is significantly simplified. Therefore, the author's work using publicly available tools such as OpenFOAM to study multiphase flow, is a much needed addition to the knowledge base of two phase flow in the petroleum industry, which has been largely limited by accessibly computational resources. This is a problem that may be easily overcome through the petroleum industry's superior financial means.

References

Ahmed, M. and Ayoub, M. (Nov. 2014). "A Comprehensive Study on the Current Pressure Drop Calculation in Multiphase Vertical Wells; Current Trends and Future Prospective". In: *Journal of Applied Sciences* vol. 14.

Aziz, K. and Govier, G. (July 1972). "Pressure Drop In Wells Producing Oil And Gas". In: *Journal of Canadian Petroleum Technology* vol. 11.

Baker, O. (Oct. 1953). "Design of Pipelines for the Simultaneous Flow of Oil and Gas". In:

Beggs, D. and Brill, J. (May 1973). "A Study of Two-Phase Flow in Inclined Pipes". In: *Journal of Petroleum Technology* vol. 25, pp. 607–617.

Bennett, B. A. W. et al. (1965). "Paper 5: Flow Visualization Studies of Boiling at High Pressure". In: *Proceedings of the Institution of Mechanical Engineers, Conference Proceedings* vol. 180, no. 3, pp. 260–283.

Bertola, V. (July 2000). "New Trends in Water and Environmental Engineering for Safety and Life An experimental investigation on the intermittent air-water flow in horizontal pipes". In:

BP (2010). *Deepwater Horizon Accident Investigation Report*. URL: https://www.sec.gov/Archives/edgar/data/313807/000119312510216268/dex993.htm. (accessed: 01.16.2020).

BP Deepwater Horizon Oil Spill, U. S. N. C. on the and Drilling, O. (2011). *Macondo : the Gulf oil disaster : Chief Counsel's report*. URL: https://repository.library.noaa.gov/view/noaa/71. (accessed: 1/16/2020).

Brennen, C. E. (2005). *Fundamentals of Multiphase Flow*. Cambridge University Press.

Caetano, E. (1985). "Upward Vertical Two-Phase Flow Through an Annulus". PhD thesis. The University of Tulsa.

Choueiri, G. (2014). "Experimental investigations of flow development, gap instability and gap vortex street generation in eccentric annular channels". PhD thesis. University of Ottawa.

Cioncolini, A. and Thome, J. (July 2012). "Void fraction prediction in annular two-phase flow". In: *International Journal of Multiphase Flow* vol. 43, pp. 72–84.

Das, A. and Das, P. (Feb. 2010). "Modelling bubbly flow and its transitions in vertical annuli using population balance technique". In: *International Journal of Heat and Fluid Flow - INT J HEAT FLUID FLOW* vol. 31, pp. 101–114.

Das, G. et al. (1998). "Rise velocity of a Taylor bubble through concentric annulus". In: *Chemical Engineering Science* vol. 53, no. 5, pp. 977–993.

— (Dec. 1999). "Flow Pattern Transition During Gas Liquid Upflow Through Vertical Concentric Annuli—Part II: Mechanistic Models". In: *Journal of Fluids Engineering* vol. 121, no. 4, pp. 902–907.

Davies, R. M. and Taylor, G. (1950). "The Mechanics of Large Bubbles Rising through Extended Liquids and through Liquids in Tubes". In: vol. 200. 1062. The Royal Society, pp. 375–390.

Denton, J. (1963). "Turbulent flow in concentric and eccentric annuli". MA thesis. The University of British Columbia.

DHSG (2011). *Final Report on the Investigation of the Macondo Well Blowout*. URL: https://ccrm.berkeley.edu/pdfs_papers/bea_pdfs/DHSGFinalReport-March2011-tag.pdf. (accessed: 01.16.2020).

DNV (2011). *Forensic Examination of Deepwater Horizon Blowout Preventer*. URL: https://www.bsee.gov/sites/bsee.gov/files/research-guidance-manuals-or-best-practices/fact-sheet/dnvreportvoli1.pdf. (accessed: 01.16.2020).

Escudier, M., Oliveira, P., and Pinho, F. (2002). "Fully developed laminar flow of purely viscous non-Newtonian liquids through annuli, including the effects of eccentricity and inner-cylinder rotation". In: *International Journal of Heat and Fluid Flow* vol. 23, no. 1, pp. 52–73.

Eyo, E. and Lao, L. (2019). "Gas-liquid flow regimes in horizontal annulus". In: *Journal of Petroleum Science and Engineering* vol. 175, pp. 573–586.

Faghri, A. (Nov. 1989). "Performance Characteristics of a Concentric Annular Heat Pipe: Part II—Vapor Flow Analysis". In: *Journal of Heat Transfer* vol. 111, pp. 851–857.

Ghajar, A. (Mar. 2005). "Non-boiling heat transfer in gas-liquid flow in pipes: a tutorial". In: *Journal of the Brazilian Society of Mechanical Sciences and Engineering* vol. 27, pp. 46–73.

Guilizzoni, M. et al. (May 2019). "Characterization of plug and slug multiphase flows by means of image analysis". In: *Journal of Physics: Conference Series* vol. 1249.

Hagedorn, A. and Brown, K. (Apr. 1965). "Experimental Study of Pressure Gradients Occurring During Continuous Two-Phase Flow in Small-Diameter Vertical Conduits". In: *Journal of Petroleum Technology* vol. 17.

Hanks, R. W. and Bonner, W. F. (1971). "Transitional Flow Phenomena in Concentric Annuli". In: *Industrial & Engineering Chemistry Fundamentals* vol. 10, no. 1, pp. 105–113.

Hasan, A. and Kabir, C. (1992). "Two-phase flow in vertical and inclined annuli". In: *International Journal of Multiphase Flow* vol. 18, no. 2, pp. 279–293.

— (May 1988). "A study of multiphase flow behavior in vertical wells". In: *Journal of Petroleum Engineers*.

Hennecke, C., VonderHaar, H., and Dinkelacker, F. (2017). "Failure Detection in an Annular Combustion Chamber with Experimental and Numerical Methods". In: *Journal of Aeronautics & Aerospace Engineering* vol. 6.

Hewitt, F. (2012). "Churn and Wispy Annular Flow Regimes in Vertical Gas–Liquid Flows". In: *Energy & Fuels* vol. 26, no. 7, pp. 4067–4077.

Hewitt, G. (2010). *Multiphase Flow*. URL: http://www.thermopedia.com/content/4/. (accessed: 01.14.2020).

Hewitt, G. and Roberts, D. (Feb. 1969). *Studies of two-phase flow patterns by simultaneous x-ray and flast photography*. Tech. rep.

Hills, J. and Chéty, P. (1998). "The Rising Velocity of Taylor Bubbles in an Annulus". In: *Chemical Engineering Research and Design* vol. 76, no. 6. Process Design, pp. 723–727.

Hoogendoorn, C. (1959). "Gas-liquid flow in horizontal pipes". In: *Chemical Engineering Science* vol. 9, no. 4, pp. 205–217.

Inaba, Y. et al. (2005). “Natural convection heat transfer of high temperature gas in an annulus between two vertical concentric cylinders”. In: *Heat Transfer - Asian Research* vol. 34, no. 5, pp. 293–308.

Iyer, S. and Vafai, K. (1998). “Buoyancy induced flow and heat transfer in a cylindrical annulus with multiple perturbations”. In: *International Journal of Heat and Mass Transfer* vol. 41, no. 20, pp. 3025–3035.

Jahanandish, I., Salimifard, B., and Jalalifar, H. (2011). “Predicting bottomhole pressure in vertical multiphase flowing wells using artificial neural networks”. In: *Journal of Petroleum Science and Engineering* vol. 75, no. 3, pp. 336–342.

Jeong, J. et al. (2008). “Interfacial area transport of vertical upward air–water two-phase flow in an annulus channel”. In: *International Journal of Heat and Fluid Flow* vol. 29, no. 1, pp. 178–193.

Ju, B. et al. (Sept. 2008). “A Study to Prevent Bottom Water From Coning in Heavy-Oil Reservoirs: Design and Simulation Approaches”. In: *Journal of Energy Resources Technology-transactions of The Asme - J ENERG RESOUR TECHNOL* vol. 130.

Kaichiro, M. and Ishii, M. (1984). “Flow regime transition criteria for upward two-phase flow in vertical tubes”. In: *International Journal of Heat and Mass Transfer* vol. 27, no. 5, pp. 723–737.

Kaneda, M. et al. (2003). “The characteristics of turbulent flow and convection in concentric circular annuli. Part I: flow”. In: *International Journal of Heat and Mass Transfer* vol. 46, no. 26, pp. 5045–5057.

Kelessidis, V., Dalamarinis, P., and Maglione, R. (2011). “Experimental study and predictions of pressure losses of fluids modeled as Herschel–Bulkley in concentric and eccentric annuli in laminar, transitional and turbulent flows”. In: *Journal of Petroleum Science and Engineering* vol. 77, no. 3, pp. 305–312.

Kelessidis, V. and Dukler, A. (1989). “Modeling flow pattern transitions for upward gas-liquid flow in vertical concentric and eccentric annuli”. In: *International Journal of Multiphase Flow* vol. 15, no. 2, pp. 173–191.

— (1990). “Motion of large gas bubbles through liquids in vertical concentric and eccentric annuli”. In: *International Journal of Multiphase Flow* vol. 16, no. 3, pp. 375–390.

Kiran, R., Ahmed, R., and Salehi, S. (2020). “Experiments and CFD modelling for two phase flow in a vertical annulus”. In: *Chemical Engineering Research and Design* vol. 153, pp. 201–211.

Mandhane, J., Gregory, G., and Aziz, K. (1974). “A flow pattern map for gas—liquid flow in horizontal pipes”. In: *International Journal of Multiphase Flow* vol. 1, no. 4, pp. 537–553.

Mark, C. and Selwyn, A. (2016). “Design and analysis of annular combustion chamber of a low bypass turbofan engine in a jet trainer aircraft”. In: *Propulsion and Power Research* vol. 5, no. 2, pp. 97–107.

McNutt, M. K. et al. (2012). “Review of flow rate estimates of the Deepwater Horizon oil spill”. In: *Proceedings of the National Academy of Sciences* vol. 109, no. 50.

Mizushima, J., Hayashi, S., and Adachi, T. (2001). "Transitions of natural convection in a horizontal annulus". In: *International Journal of Heat and Mass Transfer* vol. 44, no. 6, pp. 1249–1257.

Nikitin, N., Wang, H., and Chernyshenko, S. (2009). "Turbulent flow and heat transfer in eccentric annulus". In: *Journal of Fluid Mechanics* vol. 638, pp. 95–116.

Osman, E., Ayoub, M., and Aggour, M. (Mar. 2005). "An Artificial Neural Network Model for Predicting Bottomhole Flowing Pressure in Vertical Multiphase Flow". In: *SPE Middle East Oil and Gas Show and Conference, MEOS, Proceedings*.

Ozar, B. et al. (2008). "Flow structure of gas–liquid two-phase flow in an annulus". In: *Chemical Engineering Science* vol. 63, no. 15, pp. 3998–4011.

Petalas, N. and Aziz, K. (June 2000). "A Mechanistic Model For Multiphase Flow In Pipes". In: *Journal of Canadian Petroleum Technology* vol. 39.

Rodriguez, O. and Baldani, L. (2012). "Prediction of pressure gradient and holdup in wavy stratified liquid–liquid inclined pipe flow". In: *Journal of Petroleum Science and Engineering* vol. 96-97, pp. 140–151.

Rogero, E. (2009). "Experimental Investigation of Developing Plug and Slug Flows". PhD thesis. Technical University of Munich.

Rooki, R. and Rakhshkhorshid, M. (2017). "Cuttings transport modeling in underbalanced oil drilling operation using radial basis neural network". In: *Egyptian Journal of Petroleum* vol. 26, no. 2, pp. 541–546.

Schulmberger (2020). *Plug flow*. URL: https://www.glossary.oilfield.slb.com/en/Terms/p/plug_flow.aspx. (accessed: 01.15.2020).

Shaikh, A. and Muthanna, A. (May 2007). "A Review on Flow Regime Transition in Bubble Columns". In: *International Journal of Chemical Reactor Engineering* vol. 5, p. 1.

Gas-Liquid Flow Through Horizontal Eccentric Annuli: CFD and Experiments Compared (July 2011). Vol. ASME-JSME-KSME 2011 Joint Fluids Engineering Conference: Volume 1, Symposia – Parts A, B, C, and D. Fluids Engineering Division Summer Meeting, pp. 3847–3852.

Spedding, P. and Nguyen, V. (1980). "Regime maps for air water two phase flow". In: *Chemical Engineering Science* vol. 35, no. 4, pp. 779–793.

Sun, X. et al. (May 2013). "Cuttings Transport with Gas in the Highly-Deviated Horizontal Wells". In: *The Open Fuels & Energy Science Journal* vol. 6, pp. 23–29.

Taitel, Y. and Dukler, A. (1976). "A model for predicting flow regime transitions in horizontal and near horizontal gas-liquid flow". In: *AIChE Journal* vol. 22, no. 1, pp. 47–55.

Wongwises, S. and Pipathattakul, M. (2006). "Flow pattern, pressure drop and void fraction of two-phase gas–liquid flow in an inclined narrow annular channel". In: *Experimental Thermal and Fluid Science* vol. 30, no. 4, pp. 345–354.

Wu, B. et al. (2017). "A critical review of flow maps for gas-liquid flows in vertical pipes and annuli". In: *Chemical Engineering Journal* vol. 326, pp. 350–377.

Wu, H., Zhou, F., and Wu, Y. (Mar. 2001). “Intelligent identification system of flow regime of oil–gas–water multiphase flow”. In: *International Journal of Multiphase Flow* vol. 27, pp. 459–475.

Yovanovich, M., Culham, J., and Lemczyk, T. (1988). “Simplified solutions to circular annular fins with contact resistance and end cooling”. In: *Journal of Thermophysics and Heat Transfer* vol. 2, no. 2, pp. 152–157.

Zeigarnik, Y. (2010). *Annular flow*. URL: http://www.thermopedia.com/content/11/. (accessed: 01.17.2020).

Authors’ addresses

Christopher Friedemann University of Oslo, Postboks 1337 Blindern, 0316 Oslo, Norway, fauthor@uio.no

Chapter 2

Experimental campaign at Institute for Energy Technology

As part of a broader research collaboration between the University of Oslo and Institute for Energy Technology, several experimental campaigns were conducted in parallel to the computational research conduced at UiO for the purpose of this thesis. While the author was not involved in either the execution nor setup of the experiments, a short description of this collaborative experimental work is relevant due to the verification of the simulations in this thesis through the experiments. Each experimental campaign utilized a different setup to study the effects of pipe diameter ratios, inclination, and eccentricity. The annular horizontal flow loop was 49 m long, while its inclined and vertical configurations were 14 m long; significantly shorter due to physical dimensions of the facilities where the experiments were conducted. Along the streamwise direction of the annulus, 4 cameras were installed, one of which was at a significantly higher frame-rate. Further, several data acquisition stations were installed to record values for experimental parameters including, pressure gradient measured by a differential pressure transducer (DP), holdup through broad beam gamma densitometry (G), and x-ray tomography.

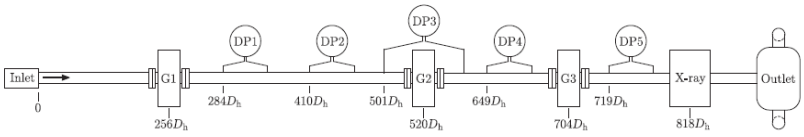

Figure 2.1: Horizontal flow-loop schematic with indicated measurement devices. Adapted from Ibarra and Nossen (2019)

The flow-loop illustrated in Fig.2.1 represents a schematic of the flow loop in a horizontal configuration. The inclined configurations (Fig. 2.2) are similar, but are significantly shortened due to dimensional restrictions. The high-speed camera locations, which are not indicated in this figure, are distributed along the annular pipe at 3 different locations in the horizontal configuration. Through the experimental data acquisition, which measures the pressure gradient at roughly 2 Hz and the fractional hold up at 50 Hz, the acquired data can be directly compared to the simulations. The visual data captured through the high-speed cameras can be used to identify flow regimes, and with further analysis, the bubble size of the entrained gas within the liquid phase can be determined.

The experiments conducted at IFE, w

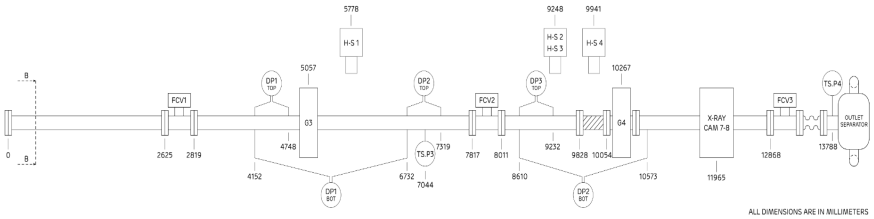

Figure 2.2: Inclined flow-loop schematic with indicated measurement devices.

The broadbeam gamma densitometry measures holdup through application of the equation which describes photon attenuation Eq. (2.1)

$$\gamma = \gamma_o exp(-\mu t). \tag{2.1}$$

In order to calculate the liquid holdup, the attenuation for pure liquid (γ_l) and pure gas γ_g is needed. These values are obtained through single-phase calibration measurements. Following calibration, the mixture attenuation γ_m is measured during the multiphase experiments using the same procedure as in single-phase. With all the attenuation values in place, the calculation of the liquid holdup is as follows:

$$\alpha_l = \frac{log(\frac{\gamma_m}{\gamma_g})}{log(\frac{\gamma l}{\gamma_g})}. \tag{2.2}$$

There are many other aspects to the flow loop which are not directly addressed through a simple schematic or explained by an equation. Because the experimental setup utilizes a flow loop, the liquid and gas phases are recycled. In other words, the gas and liquid are separated after the outlet and re-injected at the inlet. In order to ensure that the continuous cycle utilizes a clean gas and liquid phase, the gas undergoes a two-stage separation stage. Initially the mixture is passed through a gas-liquid separator. Prior to re-injection to the test section the gas phase is scrubbed in order to remove any remaining liquid (Ibarra, Nossen, and Tutkun, 2019c). The liquid phase alternatively is not passed through a secondary separator, instead it flows through a Coriolis meter which can be used to monitor the density. Ibarra, Nossen, and Tutkun (2019c) reported that even at the highest mixture velocities tested, no changes to the density of the liquids was observed.

The gas and liquid phases are delivered to the inlet section through different means. The gas phase is injected using a compressor, and the gas rate is measured with a turbine flow meter. The liquid phase is injected to the inlet section using centrifugal pumps, and the flow rate is measured using the same Coriolis meters that monitor the liquid density. The oil injection line is also equipped with heat exchangers to maintain a steady temperature throughout the experimental

test. The inlet section is meticulously designed in order to deliver a stratified inlet flow. This is achieved through a splitter plate and flow straightener. The combination of the two flow devices act to deliver a repeatable stratified and swirl reduced initial flow state.

There is also the aspect of the two cylindrical pipes which together create the annular flow conduit. The experimental test section is made up of a clear PVC which allows the capture of some flow information through non-intrusive visual means. The interior pipe is held in place by specially designed wings. These spokes are crafted in such a way as to minimally effect the flow. Of course, there is no spoke design that could leave no footprint; however, in order to create a rigid interior pipe, the pipe must be kept in place by spokes. Without these spokes, the interior pipe would travel together with large liquid bodies and potentially increase the load of the test system. If a researcher has observed a slug flow first hand in an experimental flow loop, it is apparent that there are tremendous forces involved and all steps should be taken to ensure the integrity of the structural system.

The scientists at IFE worked strenuously to perform an extremely vast array of experiments using a variety of inclinations, eccentricities, single, two, and even three-phase flow, as well as inner to outer pipe ratios. In comparison for every 1 simulation that was able to be run by the author from start to end, the IFE lab produced in the region of 100 experimental cases. In Ibarra, Nossen, and Tutkun (2019c), a singular publication on the topic of slug flow in horizontal annulus, a total of 478 slug flow conditions were produced.

The experimental campaigns conducted in parallel with the authors simulations resulted in several other publications by Roberto Ibarra, Jan Nossen, Murat Tutkun, and Olaf Skjæraasen. These authors' works explored a variety of subjects including flow patterns, pressure gradients, algorithm development, and fluid distribution, and utilized varying techniques, including x-ray tomography and laser doppler anemometry.

Ibarra and Nossen (2018) studied bubble velocities in both horizontal and low inclination upward slug flows, in concentric and eccentric annuli. One significant finding was that models for hollow pipes under-predict the Taylor bubble velocity for high mixture Froude numbers. Based on these results, Ibarra and Nossen (2018) developed a new model to predict bubble velocity in annuli. This model was intended to replace full pipe models for mixture Froude numbers higher than the critical $Fr_{M,C} = 3.3$. The Froude number is conventionally calculated as a function of the characteristic flow velocity (U_0), characteristic length (l_0), and gravity (g).

$$Fr = \frac{U_0}{\sqrt{gl_0}}. \tag{2.3}$$

For multiphase flow in an annulus, the characteristic flow velocity is the mixture velocity (U_m) and the characteristic length is the hydraulic diameter (D_h). Occasionally for multiphase flows there is an additional modification of the Froude number, based on the density ratio of the fluids. With this modification,

the Froude number for an oil-water mixture is

$$Fr_M = \frac{U_M}{\sqrt{gD_h(1 - \frac{\rho_{oil}}{\rho_w})}}. \tag{2.4}$$

In a two part publication, Ibarra, Nossen, and Tutkun (2019a), and Ibarra, Nossen, and Tutkun (2019b) two-phase oil and gas flow in both concentric and fully eccentric annuli was studied. In this extensive study, the flow patterns, pressure gradients, and slip ratios were analyzed and a mechanistic model was developed for horizontal gas-liquid flow in an annulus. This newly developed mechanistic model performed well when compared to experimental data. Through these experiments, it was discovered that pipe wettability has a large effect on the flow in a concentric annulus, with a smaller effect in an eccentric annulus, resulting in the observation of a more well defined structure in the eccentric annulus experiments. It was also confirmed that the pressure drop is larger in a concentric annulus than in a fully eccentric annulus for similar flows.

In 2019, Ibarra and Nossen (2019) and Ibarra, Nossen, and Tutkun (2019c), studied gas-liquid and liquid-liquid flow in both concentric and fully eccentric annuli pipes. Flow regime maps were developed based on the data collected from the high-speed cameras and X-ray projections, and a new correlation for the prediction of slug frequency in annular pipes was created. It was observed that the water holdup fractions for constant mixture velocities were higher in the eccentric water-oil slugs than they were in the concentric experiments. It was argued that the increased water hold up fraction occurred due to a small gap near the contact line of the two pipes. A similar observation was made for gas-water flow, where the gas entrainment within the liquid slugs was higher for the concentric cases. However, for the gas-water cases, it was argued that the increased gas entrainment was caused by the wetting characteristics of the PVC pipe, which at high velocities was not continuously wetted by the water, promoting entrainment and the break-up of bubbles. The authors of this study concluded that the hollow pipe models were insufficient for prediction of slug characteristics in annuli and that the eccentricity had only a small effect on the slug characteristics. The researchers at IFE published 1 additional article in the form of a conference paper, where they utilized x-ray tomography to analyze the structures of gas-liquid slug flow (Ibarra, Skjæraasen, et al., 2019).

The characteristic velocity U_m and fractional holdups were extracted from the accumulated experimental data at IFE, and were utilized as a momentum-source and for initial conditions in the simulations completed within this thesis.

References

Ibarra, R. and Nossen, J. (2018). “Bubble velocity in horizontal and low-inclination upward slug flow in concentric and fully eccentric annuli”. In: *Chemical Engineering Science* vol. 192, pp. 774–787.

— (2019). “Investigation of oil-water flow in concentric and fully eccentric annuli pipes”. In: *Chemical Engineering Science: X* vol. 4, p. 100042.

Ibarra, R., Nossen, J., and Tutkun, M. (2019a). “Two-phase gas-liquid flow in concentric and fully eccentric annuli. Part I: Flow patterns, holdup, slip ratio and pressure gradient”. In: *Chemical Engineering Science* vol. 203, pp. 489–500.

— (2019b). “Two-phase gas-liquid flow in concentric and fully eccentric annuli. Part II: Model development, flow regime transition algorithm and pressure gradient”. In: *Chemical Engineering Science* vol. 203, pp. 501–510.

Ibarra, R., Skjæraasen, O., and J.Nossen (2019). “Flow Structures of Gas-Liquid Slug Flow in Annuli Using X-Ray Tomography”. In:

Ibarra, R., Nossen, J., and Tutkun, M. (2019c). “Holdup and frequency characteristics of slug flow in concentric and fully eccentric annuli pipes”. In: *Journal of Petroleum Science and Engineering* vol. 182, p. 106256.

Chapter 3

Numerical Method in OpenFOAM

OpenFOAM is a publicly available open-source software with a large community of contributors and assistance available for troubleshooting. Since OpenFOAM's release in 2004, the solvers and naming conventions have received several updates through release iterations. The majority of the work performed in this thesis utilized OpenFOAM 4.1. If the reader is familiar with a different release, the naming conventions may differ somewhat.

There are several computational solution approaches available for two-phase flow through the default OpenFOAM package. The two main approaches are the Euler-Euler and the Euler-Lagrange as contextualized in Fig. 3.1. There are specific models and solvers that utilize each of the above approaches, including the VOF model and the Eulerian model for the Euler-Euler approach, and the sprayFoam solver for the Euler-Lagrange approach. Within this thesis a VOF model was utilized using the Euler-Euler approach.

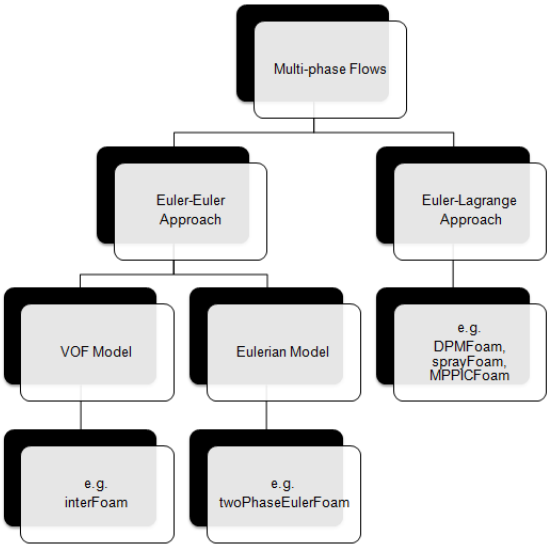

Figure 3.1: OpenFOAM multiphase solvers, categorized by solution method. Adapted from cfdyna.com (2020)

The naming convention of the illustrated approaches represent the phase behavior solution procedure. In the Euler-Lagrange approach there are two phases, the fluid phase and the dispersed phase. The fluid phase is treated as a continuum (Euler) and solved using the Navier-Stokes equations at each

meshed grid point, while the dispersed phase is solved using particle tracking (Lagrange) in the form of Newton's equations of motion through the continuous flow field. Depending on the number of particles, this approach can become extremely computationally expensive. Therefore, it is usually common to utilize the Euler-Lagrange approach when the dispersed phase occupies less than 10 % of the total volume fraction (ANSYS, 2009; cfdyna.com, 2020). Because neither the gas nor the liquid phase in this thesis are categorized as dispersed phases, solving them by particle tracking would be inefficient and less reliable. In addition, the Euler-Lagrange approach may not be suitable for streamwise periodic flows with prescribed mass flow or pressure drop (ANSYS, 2009), such as the flows studied in this thesis. Due to these reasons, the Euler-Lagrange approach is less suitable for the simulations within this thesis. This approach may be more suitable for future studies when particle tracking of sand grains or dispersed bubbles in a fluid are of interest.

The emphasis of the present work is two-phase gas-liquid flows with relatively high gas volume fractions, which enables the Euler-Euler approach to be selected as the most suitable method for the computational work conducted within this thesis. The three solvers that are most applicable to this thesis and that utilize the Euler-Euler approach are interFoam, which uses the VOF model, and twoPhaseEulerFoam or multiphaseEulerFoam, which both use an Eulerian model.

The defining difference between the VOF and Eulerian model lies in how the two phases within each model are treated. In solvers that utilize a Eulerian model, such as the twoPhaseEulerFoam and multiphaseEulerFoam, the phases are treated separately through n sets of equations for the conservation of mass and momentum. By solving separate equations for the conservation of mass and momentum, more information describing the behavior of each phase is retained, including momentum transfer between phases and the exact location of the fluid interface. Unfortunately, in using a separate solution for each phase, this also significantly increases the time required to complete the computations when compared to a single equation approach based on mixture modeling such as VOF. However, this increase in simulation time is not enough to deter from utilizing a specific solver. The Eulerian solvers, twoPhaseEulerFoam and multiPhaseEulerFoam, are designed for cases with interpenetrating continua, usually 1 continuous phase and 1 dispersed phase. For this reason, the Eulerian solvers in OpenFOAM require additional information, about bubble diameter, drag modeling, and which phase is considered the disperse phase. For flows such as dispersed bubble flow, the Eulerian solver implementations in OpenFoam have clear advantages; however, because the emphasis of this thesis lies in examining flow regimes with predominantly separate phases including slug, wavy, and churn flow, the Eulerian solvers currently available in OpenFOAM do not fit the expected flow behavior for the present studies.

A VOF type solver alternatively is based on a fluid mixture model, which is also known as a phase-averaged model. This type of model performs the computations for conservation of mass and momentum using a single set of equations for the calculated averaged fluid within each computational cell. The

interface location between phases is unknown and tracked through an advection equation. Due to the single flow field, momentum transfer between phases is not calculated (Rusche, 2002; Ubbink and Issa, 1999). While the VOF model performs very well for separated flows, there are issues when simulating interpenetrating continua and highly self-aerating flows. This problem manifests itself through bubble size, where bubbles that are smaller than the cell size are not properly resolved. For this reason, the grid should preferably be smaller than the size of the smallest expected bubbles, such that each bubble is resolved by multiple cells.

The bubble formation issue is observed in paper 3 submitted as part of this thesis. In paper 3 an increased development of bubbles is clearly shown as a function of mesh density. At all mesh densities the transition from stratified flow to slug flow occurs in the conventional way. In other words, the process begins when the shear forces between the liquid and gas overcome the surface tension causing Kelvin-Helmholtz instability. As the instability grows and the waves are amplified, some waves merge with other waves which causes an wave amplification effect. This process can eventually produce slugs. When these large waves crash, significant amounts of gas should be introduced into the liquid layer; however, at coarse meshes, these self-aerating flows are not accurately captured by VOF models.

Modeling self-aerating flows with the VOF model is a complicated process. The belief is that a happy middle-point of accuracy and solution time may be reached with interFoam even without further addressing the problem. One possible solution to this issue of self-aeration is adaptive meshing, which is a solution that could very well be tested in the future. There are further approaches that may be attempted as well and one drawback of the current work is that only OpenFOAM simulations performed in interFoam were included in the thesis. For the vertical simulations, if more time was allotted, an Euler-Euler approach may have been tested with a beneficial outcome. In addition, there are additional software programs available that combine Eularian models and VOF methods. These approaches may be beneficial in any future attempted work, so that the best of both approaches could be applied. For example, modeling the dispersed region with a Eularian model, and the separated flows with the VOF model.

Depending on the application, the ideal model for use is determined through the physical interactions that are simulated. For example, the Eulerian model should be utilized in simulations where heat transfer between phases is present, due to its inherent ability to solve the enthalpy equations separately. While examining heat transfer within an annulus during two phase flow is a topic that has been studied extensively (Adachi and Imai, 2007; Hasan and Kabir, 2012; Mizushima et al., 2001), the emphasis of this thesis is in examining flow regimes, pressure gradients, and frequencies, and does not focus on heat transfer. The flow regimes studied in this thesis are not considered dispersed flows and are separated for long periods. Therefore, separate equations per phase, as in the Eulerian model, are not needed. Furthermore, the utilization of the Eulerian model would significantly increase the required computational resources, without an increase in useful information. The VOF solver interFoam is a preferred

solver choice due to the relatively fast solution method, and the sharp interface, which is important for slug and wave simulations. This solver has also been extensively used for similar cases, most often in hollow pipes (Knotek et al., 2016; Shuard et al., 2016; Thaker and Banerjee, 2013). In particular, Shuard's research simulating several different flow regimes using interFoam and a water-air fluid composition, contributed several fundamental ideas regarding the setup and meshing of the domain for the simulations presented in this thesis.

The research performed by Thaker and Banerjee (2013) also represents a significant inspiration to utilize the interFoam solver for slug flow simulations. However short the time-periods presented in Thaker's paper are, the results are nonetheless impressive. In a conference appearance which is not included as part of this thesis, we did utilize similar boundary conditions as Thaker and Banerjee (2013) and Shuard et al. (2016), however after struggling to reproduce our experimental data over long simulation times the decision was made to move on to periodic boundary conditions.

From Shuard‘s research, it was found that there was an insignificant amount of flow across the centerline of a hollow pipe, which allowed Shuard to mirror the domain across the y-plane to reduce the computational demands. As previously mentioned, in annuli with either inclined or vertical configurations, the Taylor bubbles are asymmetric; however, the illustrations and observations made by Caetano (1985), Das et al. (1998), and Kelessidis and Dukler (1990) indicate that the Taylor bubble shape is symmetric around the y-plane.

Because the asymmetry of the Taylor bubble is dependent on the position of the interior pipe, while the bubble is symmetric across the y-plane, the interior pipe is only displaced in the y-direction in the work presented in this thesis. Thereby, the domain that is utilized can be applied with a symmetric boundary condition across the y-plane, even in cases where slug flow is expected. As mentioned previously, the symmetry procedure was further extended to two planes by Kiran et al. (2020) in his vertical simulations which employed a Fluent VOF model. In their work, two symmetry boundary conditions were applied on the y and x-planes to further reduce the computational demands without sacrificing essential physics. Kiran was able to apply this double symmetry to his research because the flow regimes that were studied (churn and annular) were unaffected by x and y-plane symmetry boundary conditions.

The basis of the VOF model employed in this thesis builds upon resolving the fluid flow through the use of an imaginary fluid and utilizing an interface tracking method to differentiate between the two separate phases. The fluid in VOF solvers that is averaged across phases, is referred to as a phase-average or mixture fluid. One of the drawbacks of VOF solvers is the smearing of the interface (Berberovic, 2010; Deshpande et al., 2012), and that mass-conservation can become difficult due to the solution procedure. The mass-fluxes are computed sequentially for each coordinate and then added together. This addition of the fluxes can lead to an inconsistent phase-fraction field (Ubbink and Issa, 1999), which has been observed by the author of this thesis in very coarse meshes, but appears to be less prominent in finer meshes. The implementation of the flux addition is complicated in arbitrary meshes (Berberovic, 2010; Ubbink and Issa,

1999). For this reason the use of hexahedral elements are advised when utilizing interFoam and efforts should be made to ensure elements are neatly organized as displayed in Fig. 3.2.

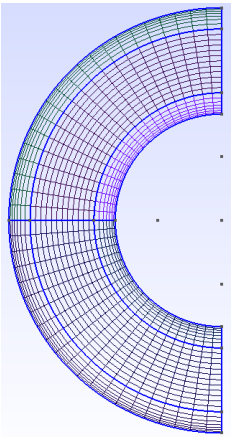

Figure 3.2: Hexahedral mesh for concentric annulus with wall refinement

As shown in Fig. 3.2, there is a region of wall refinement adjacent to both cylinder walls. Wall refinement is not necessarily a requirement when the wall boundary conditions are defined as wall functions; however, even with wall functions, care must be taken to ensure that the first element is within the logarithmic layer ($30 < y^+ < 200$) (Liu, 2016). For this reason, the size of the elements closest to the wall are strictly controlled to ensure a smooth transition to the interior region.

3.1 Description of the InterFoam solver

InterFoam, which is OpenFOAM's VOF based multiphase solver, is the solver utilized for the simulations presented in this thesis. The case structure of interFoam mimics those of most OpenFOAM solvers.

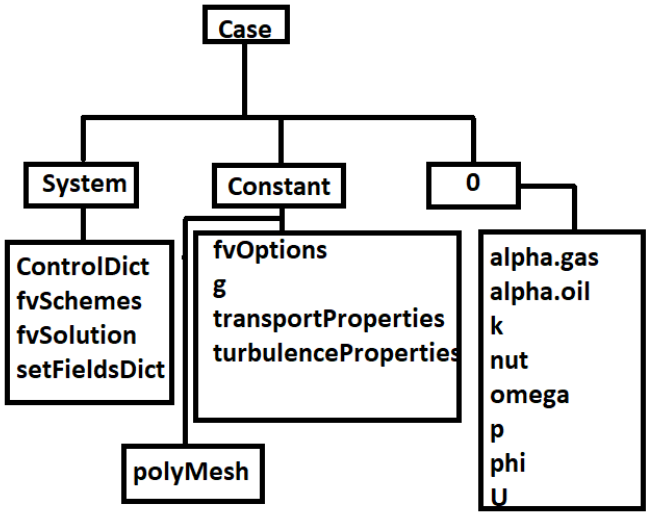

Figure 3.3: Case structure of interFoam solver

Fig. 3.3 generalizes the case structure used in interFoam. A short description of each is useful for the reader.

- The system directory includes the files controlDict, fvSchemes, fvSolution, and setFieldsDict. Controldict functions to establish general settings including how often data is saved and in what format, such as ASCII or binary. fvSchemes sets the discretisation schemes including divergence, gradient, and temporal schemes. fvSolution controls the solution algorithm and tolerances for important aspects including the velocity and pressure as well as how many correction loops are taken in the PIMPLE loop, which is a combination of Pressure-Implicit with Splitting of Operators (PISO) and Semi Implicit Method for Pressure Linked Equations (SIMPLE). setFieldsDict can be used to set an initial flow field In the cases presented in this thesis, commonly the phases are initialized as stratified flow at the phase velocities extracted from the experimental data, and allowed to develop from that initial state.
- The Constant directory includes all aspects of the simulation that are set at the start and unchanging, including the sub-directory polyMesh which includes all the mesh information. In the case of the meshes used

in this thesis, they were made in GMSH and converted to OpenFOAM format through built-in commands. fvOptions is a necessary file that needs to be included when periodic boundary conditions are used. In this file, the momentumSource which drives the flow is specified. Within the constant directory, the turbulence model (turbulenceProperties) and phase properties (transportProperties) are also specified. There are several enabled turbulence models for interFoam, including LES, $k-\omega$ and $k-\epsilon$. The gravity file (g) can be easily manipulated to specify the direction and magnitude of gravity.

- Lastly, there is the time directory (0). A new directory will be created for each save time specified in controlDict. Within this directory all the field properties are saved.

It should be mentioned that for all inclined simulations in this thesis we introduce a small modification to the interFoam Solver. Rather than utilizing the modified pressure equations implemented in interFoam (3.7) and (3.8) which includes a gravity term, the solver is adjusted to reflect a pressure equation without the incorporated gravity term. The original pressure equation, with the gravity term, contradicts the periodic boundary condition used in this thesis when the domain is inclined and is therefore inapplicable. Although at very low inclinations the flow appears physical with the original pressure equations, at close inspection there is a pressure discontinuity between the inlet and outlet, which is exacerbated at higher inclination. For a more thorough explanation of interFoam and its solution procedure, the most up to date and comprehensive descriptions are found in Berberovic (2010) and Deshpande et al. (2012). What follows is an introduction to the solver, but for the fine details the author's advice is to read the aforementioned thesis and article.

VOF based solvers utilize an imaginary mixture fluid to describe the flow field, rather than solving one equation for each phase of the flow field as in the Eulerian model. In order to determine the mixture fluid property, a general mixture rule, based on the fluid fraction α is applied. A mixture velocity vector, sometimes referred to as phase-averaged velocity $\bar{\mathbf{u}}$, is calculated as

$$\bar{\mathbf{u}} = (1-\alpha)\mathbf{u}_g + \alpha\mathbf{u}_l, \tag{3.1}$$

where α is the phase fraction of liquid in the computational cell. The mixture rule applied for mixture-velocity in (3.1), is also applied to other quantities including density and viscosity by replacing velocity with the relevant fluid property. Vectors are denoted by bold lettering and mixture quantities by a bar. The phase fraction (or indicator function) α is described as

$$\alpha = \begin{cases} 1 & \text{if cell is occupied by liquid} \\ 0 < \alpha < 1 & \text{if cell contains both gas and liquid} \\ 0 & \text{if cell is occupied by gas.} \end{cases} \tag{3.2}$$

The value assigned to each cell is thus based on the fraction of the fluid contained within this cell. The function returns a value of 1 if the cell contains only liquids and 0 if the cell is filled with gas. The indicator function α is solved for in a modified advection equation

$$\frac{\partial \alpha}{\partial t} + \nabla \cdot (\alpha \bar{\mathbf{u}}) + \nabla \cdot (\mathbf{u}_c \alpha (1 - \alpha)) = 0, \tag{3.3}$$

where the interface compression velocity, u_c, is used to artificially "compress" the surface, which acts to sharpen the interface between the two phases. u_c is represented as a vector of the relative velocity of the two phases. Although there are several suggested models, the most well known form was proposed by Weller (2008) and is calculated as

$$\mathbf{u}_c = min[C_\alpha |\bar{\mathbf{u}}|, max(|\bar{\mathbf{u}}|)] \frac{\nabla \alpha}{|\nabla \alpha|}. \tag{3.4}$$

The interface compression velocity is bounded by the maximum velocity within the domain.

After the implementation of mixture quantities and assuming incompressible flow, the governing continuity and momentum equations can be simplified as

$$\frac{\partial \bar{\mathbf{u}}}{\partial t} + \nabla \cdot (\bar{\mathbf{u}} \bar{\mathbf{u}}) = -\frac{1}{\bar{\rho}} \nabla p + \nabla \cdot (\bar{\nu} (\nabla \bar{\mathbf{u}} + (\nabla \bar{\mathbf{u}})^T)) + \mathbf{g} + \frac{F_s}{\bar{\rho}}, \tag{3.5}$$

$$\nabla \cdot \bar{\mathbf{u}} = 0, \tag{3.6}$$

where $\bar{\rho}$, $\bar{\nu}$, and F_s represent mixture density, viscosity, and surface tension force respectively. The calculation of the mixture components follows the same mixture rule as exemplified in Eq. (3.1).

As mentioned briefly, when interFoam is used in combination with periodic boundary conditions and in an inclined domain, a discontinuity between the inlet and outlet of the periodic domain is introduced due to the modified pressure equation utilized in interFoam. This modified pressure (p_d) equation takes the form of

$$p_d = p - \bar{\rho} \mathbf{g} \cdot \mathbf{x}, \tag{3.7}$$

$$\nabla p_d = \nabla p - \bar{\rho} \mathbf{g} - \mathbf{g} \cdot \mathbf{x} \nabla \bar{\rho}, \tag{3.8}$$

where $\mathbf{x}$ is the position vector. As is shown in Eqs. (3.7) & (3.8) there is a gravity term within the pressure equations. This gravity term creates a discontinuity for the periodic boundary condition between the inlet and outlet when the domain is inclined. In order to rectify this discontinuity, the boundary condition specification must be re-written from the modified pressure (p_d) to p, and the momentum equation must be rewritten by adding the hydrostatic component back into the equation as a separate term.

3.2 Numerical and experimental considerations

Before discussing the considerations to account for when comparing numerical and experimental data as well as if the data is comparable to field data, there are some considerations that need to be discussed when attempting to simulate two-phase flow behavior. The first and largest hurdle any scientist or interested party will encounter is the problem of computational cost. All simulations, even those performed at extremely coarse meshes will take a significant amount of time, use a large amount of storage space, and in some cases the require the use of several computers simultaneously. To illustrate these considerations, the present work accounts for roughly 15 TB of data, which does not include simulations that were done using different methods or those used for initial testing. The longest simulations in this thesis lasted several months, even after optimizing for scaling on multiple cores. According to Axtmann and Rist (2016) interFoam scales well down to 20 k cells per core; however, based on our experience the scaling significantly reduced at 80 k cells / core. That is not to say that Axtmann's findings were incorrect, rather simply that scaling can be extremely different across systems. This variance in scaling across systems is an experience that occurred throughout the present research as well when running simulations on various computing clusters. Factors such as communications protocol and computer age drastically affected the simulation speed. These issues of computational cost, in combination with mesh dependent time scaling is one of the primary reasons periodic boundary conditions were applied to the domain. Periodic boundary conditions allow us to simulate reduced domain lengths while still allowing the flow to develop over a significant length. In turn the decreased domain lengths allow for an increase in mesh resolution while maintaining a reasonable simulation time.

When considering which solution method to utilize when simulating complex two-phase flows, specifically self-aerating flows such as slugs, it is important to note that some compromises must be made when time and cost are of concern. With infinite resources and time, extremely accurate domains with mesh resolution all the way down to the smallest scales can be simulated using direct numerical simulations. However, these simulations are not practical for most purposes, and a respectable middle ground can be achieved at a lower mesh density using RANS simulations, as showed in both the research by Shuard et al. (2016) and Thaker and Banerjee, 2013. Compromising mesh resolution for decreased simulation time results in a potential loss of accuracy, especially in terms of small structures such as bubbles that in an experiment would naturally occur through wave breaking or slug behavior. However, this compromise in mesh density in the interest of time will still accurately depict the large scale behavior of the flows. In a VOF model with a loss of mesh resolution, it is possible that small bubbles are reduced artificially. This could be an effect of the solver attempting to obey the continuity equations but not having the required mesh resolution to resolve the minor bubbles, thereby pushing the gas toward the top or accumulating the gas into large bubbles. In the present simulations, it can clearly be seen that as mesh density increases, the amount of small bubbles

increase as well.

When attempting to validate numerical data based on experimental data sets, there are several consideration to make. Primarily, it is of utmost importance to consider whether the simulations are in fact representative of the experimental setup. In the case of the simulations included as part of this thesis, and the experiments analyzed alongside the simulations, the laboratory environment was expertly configured by my colleagues at IFE. In addition, the author had the opportunity to work closely with Jan Nossen, Murat Tutkun, and Roberto Ibarra, in order to ensure the computational methods used were as close to the experimental lab as could be realistically achieved. This included selecting data far downstream of the inlet, while being far enough from the outlet to negate any outlet effects.

When considering whether the numerical simulations accurately represent the experimental setup and data, there are a few considerations that should be examined. Firstly, are the simulated geometries representative of the experimental geometries? In the case of the simulations published in papers 1-3, the annulus dimensions were designed to be exact replicas of those used in the experiments, with some small discrepancies for the fully eccentric cases where experimentally there was a contact line between the interior and exterior cylinder. In addition, in order to maintain the rigidity of the interior cylinder the experimental setup implements streamlined spokes/fins to keep the inner cylinder in place. Early experiments showed that the initial design allowed for the interior cylinder to drift significantly when under the effect of large flow structures. These spokes that prohibit interior cylinder drift are not modeled in the computational domain, and could contribute to some uncertainty.

Secondly, are the boundary conditions used in the simulations representative of the experimental setup? Periodic boundary conditions are applied to the computational domain. Periodic boundary conditions are rarely a perfect fit for experimental lab conditions. Due to this, a large aspect of the first publication was devoted to domain size considerations. A short domain with periodic boundary conditions enforces limitations on the amount of liquid within the system, and can therefore influence the size and frequency of slugs, as well as if they appear at all.

In addition, when considering whether the simulations are representative of the experimental cases, the representation of the simulations and experiments compared to real wells in the field should be considered. Both simulations and experimental lab settings should be considered idealized situations that attempt to represent potential expected field behavior. Field behavior, especially something as unexpected as a leakage is not ideal, and when compared to a laboratory setting there is an abundance of potential uncontrolled variables. For example, the fluid composition may be polluted by solids or the eccentricity of the annulus may vary in the streamwise direction. The pressurization and temperature of the system and therefore the fluid properties are also influenced by external factors, which are much less likely to be modeled accurately in an experimental setting. For example, the oil lines of the experiments in this thesis were fitted with heat exchangers in order to maintain the same operating

temperature, and the system was pressurized to maintain the stability of the conditions. There are many other issues that may be encountered in a field well that are not necessarily considered in the presented simulations and experiments including the pipe material, vibration, movement, and torsion of the interior pipe as well as the influence and presence of granular objects such as sand or small rocks within the liquid phase. These factors, although not comprehensive are factors that may effect the accuracy of both experimental and computational simulations when compared to well data. Even small aspects such as a minor deviation of the eccentricity may influence transition points between flow regimes. Movement of the interior pipe and granular objects within the flow can similarly have a significant impact on both the development of the flow regime and the behavior of the pressure gradient. Although, the experiments and simulations may not be completely representative of field data, the presented data aid in further developing new tools to aid in the prediction of flow behavior of live wells. The potential of CFD to predict field behavior should not be affected by how well the experiments directly replicate field behavior. When attempting to validate some CFD results, one should always start from simplified idealized test cases, which in this case are controlled laboratory experiments, and work toward more representative cases.

References

Adachi, T. and Imai, S. (2007). "Three-dimensional linear stability of natural convection in horizontal concentric annuli". In: *International Journal of Heat and Mass Transfer* vol. 50, no. 7, pp. 1388–1396.

ANSYS, I. (2009). *Limitation on the Particle Volume Fraction.* URL: https://www.afs.enea.it/project/neptunius/docs/fluent/html/ug/node669.htm#sec-disp-oview-limits. (accessed: 05.28.2020).

Axtmann, G. and Rist, U. (Sept. 2016). *Scalability of OpenFOAM with Large Eddy Simulations and DNS on High-Performance Systems.*

Berberovic, E. (Nov. 2010). "Investigation of Free-surface Flow Associated with Drop Impact: Numerical Simulations and Theoretical Modeling". PhD thesis. Darmstadt: Technische Universität.

Caetano, E. (1985). "Upward Vertical Two-Phase Flow Through an Annulus". PhD thesis. The University of Tulsa.

cfdyna.com (2020). *OPENFOAM: Multiphase.* URL: http://www.cfdyna.com/Home/of_multiPhase.html. (accessed: 01.24.2020).

Das, G. et al. (1998). "Rise velocity of a Taylor bubble through concentric annulus". In: *Chemical Engineering Science* vol. 53, no. 5, pp. 977–993.

Deshpande, S., Anumolu, L., and Trujillo, M. (Nov. 2012). "Evaluating the performance of the two-phase flow solver interFoam". In: *Computational Science & Discovery* vol. 5.

Hasan, A. and Kabir, C. (2012). "Wellbore heat-transfer modeling and applications". In: *Journal of Petroleum Science and Engineering* vol. 86-87, pp. 127–136.

Kelessidis, V. and Dukler, A. (1990). "Motion of large gas bubbles through liquids in vertical concentric and eccentric annuli". In: *International Journal of Multiphase Flow* vol. 16, no. 3, pp. 375–390.

Kiran, R., Ahmed, R., and Salehi, S. (2020). "Experiments and CFD modelling for two phase flow in a vertical annulus". In: *Chemical Engineering Research and Design* vol. 153, pp. 201–211.

Knotek, S., Fiebach, A., and Schmelter, S. (Sept. 2016). "Numerical simulation of multiphase flows in large horizontal pipes". In: *Proceedings of 17th International Flow Measurement Conference*. Sydney, Australia.

Liu, F. (2016). "A Thorough Description Of How Wall Functions Are Implemented In OpenFOAM." In: *Proceedings of CFD with OpenSource Software*. Ed. by Nilsson, H.

Mizushima, J., Hayashi, S., and Adachi, T. (2001). "Transitions of natural convection in a horizontal annulus". In: *International Journal of Heat and Mass Transfer* vol. 44, no. 6, pp. 1249–1257.

Rusche, H. (Dec. 2002). "COMPUTATIONAL FLUID DYNAMICS OF DISPERSED TWO-PHASE FLOWS AT HIGH PHASE FRACTIONS". PhD thesis. Exhibition Road, London SW7 2BX: Imperial College London.

Shuard, A., Mahmud, H., and King, A. (2016). "Comparison of Two-Phase Pipe Flow in OpenFOAM with a Mechanistic Model". In: *IOP Conference Series: Materials Science and Engineering* vol. 121.

Thaker, J. and Banerjee, J. (Dec. 2013). "CFD SIMULATION OF TWO-PHASE FLOW PHENOMENA IN HORIZONTAL PIPELINES USING OPENFOAM". In: *Proceedings of the 40th National Conference on Fluid Mechanics and Fluid Power*.

Ubbink, O. and Issa, R. (1999). "A Method for Capturing Sharp Fluid Interfaces on Arbitrary Meshes". In: *Journal of Computational Physics* vol. 153, no. 1, pp. 26–50.

Weller, G. (Jan. 2008). *A new approach to VOF-based interface capturing methods for incompressible and compressible flow*. Tech. rep.

Chapter 4

Objectives, findings and future perspective

Before discussing the objectives of the thesis, it is important to note that throughout the literature review it was clear that there is a distinct lack of computational work related to multiphase flows in annuli, and a significant portion of the experimental work and models developed that relate to flows in annuli are older in age. Age in itself is not a problem, but it portrays that the field of flows in annuli has been less studied over time when compared to studies available with data from conventional pipes. There are several reasons that there is a scarcity of computational work related to flows in annuli, primarily being the computational cost associated with conducting two-phase CFD research has until very recently been prohibitive. In addition, two-phase solvers often need extensive modelling, requiring further knowledge of the physical behavior of the flows. Contact angle, bubble size, and how to distinguish dispersed and continuous phases may be inputs required to run a simulation. Further, depending on the solver even more complicated inputs may also be required. However, in more recent times large improvements have been made to open-source and commercial software the can simplify the simulation of two-phase flows.

Because there is very little computational work in the field of researching flows in annuli, and a significant portion of the experimental work regarding the annulus configuration is older in age, the models and methods used to predict flows in annuli often build upon hollow pipe models, which can lead to significant discrepancies. This thesis attempts to begin bridging that knowledge gap through computational means. In the present thesis, all simulations are run in the open-source software OpenFOAM. Other options are also available including Fluent and Multiflow, however an open-source software presents an advantage that anyone with a computer and the prerequisite background knowledge has the opportunity to continue the present work. A common criticism of science as a whole is that there is a high threshold for entry. While it is important that there is this high threshold in terms of knowledge and the quality of the work, the accessibility and the ability to repeat studies are also important aspects of science which should not be barriers for the dissemination and future development of the work. This is particularly crucial in a developing field, such as complex computational fluid dynamics.

The main objectives of this thesis are as follows; i) Acquire knowledge of two-phase flows within annuli for a variety of flow regimes and inclinations; ii) Validate simulations through comparisons of computational data and experimental data using flow regimes, pressure gradients, and wave and slug frequencies as parameters; iii) Utilize numerical simulations as a tool for two-phase flow

behavior prediction.

The relationship between the objectives and the papers submitted as part of this thesis are outlined below. Through assessing the aforementioned objectives in each publication, the hope is to make a step toward a computational method for the prediction of oil and gas behavior in field pipelines. It is too early to utilize solely computations when attempting to predict the behaviour of multiphase flows in wells and transport lines, however, it is necessary to develop alternate and modern methods to accompany the valuable correlations and models that already exist.

Paper I: Gas-liquid slug flow in a horizontal concentric annulus, a comparison of numerical simulations and experimental data

This paper represents the initial validation of the use of InterFoam combined with periodic boundary conditions as a tool to simulate slug flow in an annulus when an oil-gas fluid mixture is present. The simulations are compared with experiments conducted in an identical annulus with the same fluid phase fractions and mixture velocities. In this publication, the slug frequencies and pressure gradients of a specific slug flow are analyzed as a function of the mesh density, domain length, and time. While the results indicate that the simulations in the finest mesh result in the best replication of the experimental results, even at low mesh densities the slug frequencies are maintained when the domain length is an integer multiple of the slug to slug length (distance between two slug fronts or tails). When the domain length is not an integer value of the slug to slug length, both the pressure gradient and slug frequency are adversely affected. This effect is reduced by simulating domains that are long enough to contain several simultaneous slugs.

This paper is related to objectives i and ii. The validation (objective ii) is obtained through cross-analyzing the computational data with regards to holdup and pressure gradient transients with equivalent experimental data for the same mixture velocities and phase fractions. By also finding that there is a relationship between the slug to slug length, domain length and slug frequency, a clear consideration is developed for sizing domains of slug flow when using periodic boundary conditions. This relationship also has an effect on the pressure gradient observed. Together, the findings regarding pressure gradient, slug frequency and domain length represent a developing understanding of slug flow in computational fluid dynamics (objective i))

Paper II: Two-phase flow simulations at 0-4^o inclination in an eccentric annulus

In this publication, simulations are run in a partly eccentric annulus based on results from fully eccentric and concentric experiments, in order to study the effect of a change in eccentricity. This paper represents the thesis' first steps toward flow prediction using interFoam. A small change to the pressure equation in InterFoam is introduced in order to utilize periodic boundary conditions in

inclined domains. Due to the inclusion of gravity in the pressure equation term for the standard interFoam implementation, a discontinuity between inlet and outlet is formed for inclined simulations with periodic boundary conditions. In order to rectify this discontinuity, the gravity term is decoupled from the pressure equation, and the momentum equation is altered to reflect the redefined pressure equation.

Due to the different eccentricities in the experiments and simulations, the pressure gradient comparisons are relatively poor; however, it is found that reducing the eccentricity increases the pressure gradient, and increasing the eccentricity lowers the pressure gradient. This is the case in most, except for in a few cases with very low mixture velocities. This paper pertains to objectives i) and iii). Objective i) is achieved through the study of similar cases but with different eccentricities, by altering the eccentricity an understanding is developed of the flow mechanisms that contribute to develop flow regimes and pressure gradients. Because the cases studied were similar to experimental cases, but with an altered eccentricity, the paper aims to move towards flow prediction (objective iii)) by verifying known relationships, such as pressure gradients decreasing with increasing eccentricities. It was also of course encouraging that the for the most part the expected flow regimes developed.

Paper III: Two-phase co-current flow simulations using periodic boundary conditions in horizontal, 4, 10 and 90^o inclined eccentric annuli, flow prediction using a modified interFoam solver and comparison with experimental results

In this publication, horizontal and inclined simulations in a fully eccentric orientation are compared with previously gathered experimental data (objectives i and ii). The flow regimes observed are slug, wavy, and churn flow. The horizontal simulations within this publication are also compared with the horizontal simulations from Paper II, which are identical except at a lower eccentricity. By comparing the two sets of simulations at different eccentricities, it is found that the change from E=0.5 to E=1.0 results in a 30 % pressure gradient (Pa/m) decrease for the cases studied (objective iii). Apart from the two low velocity horizontal cases, the mean pressure gradient is within 33 % of the experimental data for all cases studied. In addition, by increasing the inclination of the 4^o cases to 10^o, an increase in pressure gradient is found, which is within 6 % of the theoretical value (objective iii). The flow regimes are also compared with the expected regimes from a unified model, for nearly all cases the unified model and the observed developed flow regime agrees. There are however several fringe cases, where the prediction model is very near transition to a different regime.

Future work

There remains an expansive array of topics to cover on two-phase flow in annuli. A persistent issue, which occurred throughout the works related to this thesis, is that structures resembling slugs were formed in the simulations. These structures, referred to as proto-slugs, display the characteristic behavior of conventional slugs; however, they seldom occupied the entire cross-section

as a conventional slug would. These proto-slugs develop through the same mechanisms as conventional slugs would. Typically the proto-slugs that are observed in the simulations gradually transition from stratified to wavy flow to proto-slug flow. Initially the transition happens through Kelvin-Helmholtz instability followed by continuous wave merging resulting in increasingly larger waves. This process is well-known from slug flow; however, the process falls just short of developing long lasting slugs. Interestingly, these proto-slug structures may be observed during an experiment, often as a precursor of a slug that has the potential to develop. Some of these structures were observed during the experiments discussed within this thesis, but not as prevalent as they are in the simulations.

The author believes the proto-slugs are formed due to a lack of mesh resolution and issues related to highly self-aerating flows. The bubbles dispersed within the liquid layer of the experiments are not achievable with the utilized mesh densities. Instead there is minimal self aeration achieved at coarse meshes, and rather than dispersed bubbles, the bubbles that do appear tend to be large isolated bubbles. In paper 3 a simplified geometry is used where conventional slugs appear; however, the mesh density is much greater and it would be near impossible with current resources to simulate the full annulus geometry. A possible solution could be to utilize adaptive meshing, allowing for local refinement in the areas surrounding gas-liquid interfaces.

There are other potential causes for the appearance of proto-slugs apart from mesh density and VOF models trouble with self-aerating flows which could be explored. These potential causes include surface tension, boundary conditions, and specific bubble modeling. Reducing surface tension could artificially increase mixing and a boundary condition with a variable pressure gradient, or momentum source could be applied. Further, specific bubble modeling to enhance bubble formation and breakup are all possible solutions to improve the bubble formation. In future work, it would be beneficial to identify and resolve the cause of the proto-slugs discussed.

Future work could also study in-depth the effect of inclination and eccentricity by focusing on single cases and gradually increasing the inclination or eccentricity. These studies could be extremely helpful for real-life wells and pipelines where eccentricities and inclinations may be variable, which could influence local flow conditions enough to transition the flow regime from wavy to slug.

Lastly, by performing further simulations, the computational results can be included when generating flow regime maps, models, and correlations for the prediction of two-phase flow behavior in annuli.

Papers

Paper I

Gas-liquid slug flow in a horizontal concentric annulus, a comparison of numerical simulations and experimental data

C. Friedemann, M. Mortensen, J. Nossen

Published in International Journal of Heat and Fluid flow, August 2019, volume 78, DOI:10.1016/j.ijheatfluidflow.2019.108437

International Journal of Heat and Fluid Flow 78 (2019) 108437

Contents lists available at ScienceDirect

International Journal of Heat and Fluid Flow

journal homepage: www.elsevier.com/locate/ijhff

Gas–liquid slug flow in a horizontal concentric annulus, a comparison of numerical simulations and experimental data

C. Friedemann*[,a], M. Mortensen[a], J. Nossen[b]

[a] Department of Mathematics University of Oslo, Moltke Moes vei 35, OSLO 0851, Norway
[b] Institute for Energy Technology, Kjeller, 2007, Norway

ARTICLE INFO

Keywords:
Annulus
Slug flow
Volume of fluid
Reynolds-averaged Navier–Stokes equations

ABSTRACT

Multiphase flow simulations were run in OpenFOAM utilizing InterFoam, a volume of fluid type solver. A concentric annulus geometry was constructed and periodic boundary conditions were applied to alleviate the requirement for a longer domain. The simulations were run in 3, 5 and 7 m long domains with the annulus dimensioned such that the outer and inner cylinder diameter were 0.1 and 0.05 m respectively. The 4 individual mesh designs were constructed such that the coarsest mesh consists of 102k cells/m while the finest mesh was generated with 400k cells/m. Each mesh was significantly refined within 0.005 m of both the inner and outer cylinder wall. The simulation data was compared with experimental pressure and holdup data collected at Institute for Energy Technology in Norway. The 3 and 7 m domains reproduced slug frequencies to within 9% of the experiment results of 1.43 Hz for all mesh densities. Comparatively, the 5 m domain has larger errors with respect to slugging frequency (22–27%). The 5 m case performs poorly, probably due to an artificial restraint introduced by the limitation of available liquid which is set as $\alpha_{oil} = 0.53$ for all cases. The α_{oil} restriction combined with the domain length determines the amount of liquid in the system. This interaction of factors means that the domain length is an important parameter when preparing the simulation. The pressure data display a stronger dependence on the mesh quality in comparison to the slug frequency analysis. The 3 m domain with a 400k cells/m mesh resulted in a maximum and minimum pressure gradient of 1783.5 and 803.9 Pa/m, compared to the experiment values of 1785 and 822 Pa/m, which are within 3% of the expected results.

1. Introduction

During the spring of 2010 a catastrophic event at the Macondo prospect in the Gulf of Mexico devastated the United States coastline and ocean ecosystem. The Macondo accident was compounded when the annular blowout preventer failed (LP, 2014; BP, 2010; Transocean, 2011). Following the system failure leakage through the annulus caused several hundred million liters of oil to seep into the ocean before the rupture was eventually sealed.

The ability to predict the outlet phase fractions as well as flow rates is imperative when estimating the scope of disasters caused by an uncontrolled release of environmentally harmful hydrocarbons. As noted by Gidaspow et al. (2013), there are doubts related to whether the models employed by BP in the aftermath of the oil spill were accurate. The uncertainty related to the scope of the disaster underlines the importance of understanding the annulus flow problem. The issue is further emphasized when accounting for the current status and delicate balance of our environment and ecosystem.

The modeling, simulation and validation of two-phase pipe-flow and flow regimes are fairly well understood. We can conduct reasonably accurate simulations of pressure drop, as well as reproduce flow regimes and holdup profiles from experiments (Issa and Kempf, 2003; Knotek, 2014; Valle et al., 2008; Housz et al., 2017; Parsi et al., 2017). Compared to conventional pipe flow, the special case of the annulus configuration with a submerged internal cylinder interfering with the surrounding flow is significantly less studied. There are very few if any CFD simulations which are validated by experiments. As such this paper will present simulations of a specific case based on data gathered during experiments at the Institute for Energy Technology (IFE) in Norway, the results from which have been made available as part of this project.

There are several cases of intended annulus flow within the oil and gas industry. The geometry exists between the drill pipe and casing during drilling, in a gas lifted well, and in some special cases between the tubing and casing. Although the Macondo incident and indeed most

* Corresponding author.
E-mail address: chrisjfr@student.matnat.uio.no (C. Friedemann).
URL: https://www.mn.uio.no/math/personer/vit/chrisjfr/ (C. Friedemann).

https://doi.org/10.1016/j.ijheatfluidflow.2019.108437
Received 14 December 2018; Received in revised form 25 June 2019; Accepted 1 July 2019
Available online 06 July 2019
0142-727X/

applications of the annulus configuration occurs in a vertical orientation, there are relevant annulus applications related to a horizontal orientation, such as multi-stage horizontal fracking systems (Bellarby et al., 2013). The combination of intended and unintended occurrences of annulus flow and the aftereffects of a system failure warrants the need for extensive research into understanding and predicting the behavior of multiphase flow within an annulus.

Reviewing the annulus flow body of work, we realize that there lacks literature compared to other configurations. Beyond the experimental tests and early work on annulus flow done by Kelessidis and Dukler related to vertical, concentric and eccentric annuli (Kelessidis and Dukler, 1989) from 1989, as well as Caetano's (Caetano, 1985) 1992 thesis there is scarce research covering the topic. We can identify a small body of work that deals with horizontal annuli (Sorgun et al., 2013; Ekberg et al., 1999; Chung and Sung, 2003) as well as vertical (Hasan and Kabir, 1992; Julia and Hibiki, 2011; Julia et al., 2011; Jeong et al., 2008), inclined (Hasan and Kabir, 1992; Wongwises and Pipathattakul, 2006), coiled (Xin et al., 1997), rotating (Hadžiabdić et al., 2013; Chung and Sung, 2005) and obstructed annuli (Bicalho et al., 2016). The majority of which are experimental, of considerable age and in some cases single phase. Additionally, the literature rarely addresses slug flow. Finally, most of the existing work is based on the concentric annulus configuration. The eccentricity of the annulus has an effect on the wetted surface area and frictional forces, which in turn alters pressure drop and turbulence generation. Considering this, it stands to reason that the eccentricity of the annulus should be a parameter given additional attention in later works along with other parameters such as viscosity.

Concurrent with the constant advances related to computing power, computational methods and CFD code efficiency, it has become realistic to conduct numerical simulations of several types of complex multiphase pipe flow. Among these are geometries such as T-junction risers (Tunstall and Skillen, 2016), wavy pipe (Xing et al., 2013), ventilated vertical pipe (Xiang et al., 2011), horizontal loop (Hossain et al., 2011) and even single phase flow in an annulus with a rotating inner (Chung and Sung, 2005; Escudier et al., 2000) or outer (Hadžiabdić et al., 2013) cylinder. In conjunction with the ability to simulate intricate geometries, similar advances were made with complex flows. Complex flows in the form of droplets (Verdin et al., 2014), slurry (Zambrano et al., 2017), bubbly flow (Rzehak and Kriebitzsch, 2015; Rzehak and Krepper, 2013; Colombo and Fairweather, 2015), three-phase in a U-bend (Pietrzak and Witczak, 2013) and slug flow (Hua et al., 2014; Shuard et al., 2016) are all flows that are possible to resolve within a reasonable amount of time.

All of these more or less new developments point toward the viability of conducting realistic CFD simulations of slug flow within an annulus configuration. Even though the annulus configuration in itself is a simple geometry, complexity is introduced through the internal pipes interaction with the flow. The inner pipe has the effect of increasing the overall interfacial area between wall and fluid while decreasing the interfacial area between the two fluids. Consequently, when the inner pipe is fully concentric, that is to say that the distance between the inner and outer pipe is constant, the friction factor is increased. Alternatively, for a fully eccentric pipe the opposite is true, the friction factor will always be lower than that of a regular pipe (Caetano, 1985). Therefore, depending on the eccentricity of the annulus we can expect to see markedly different behavior such as altered pressure drop, flow regimes and turbulence generation. Considering the pronounced impact of eccentricity, the annulus eccentricity is seen as an ideal topic for future work.

In this paper we have studied a specific concentric case, and compared the numerical results with available experimental data from IFE. The fluid density, viscosity and flow rates are dictated by the experimental set up and mimicked in the simulation cases. The collected experiment data represents a typical slug flow, which is defined by a body of liquid which periodically bridges the entire cross section. Although the topic of this paper is slug flow, in the future we expect to be able to develop flow regime maps akin to those created for conventional pipe flow. By analyzing diverse cases from several campaigns, including wavy flow and dispersed bubbly flow, it will be possible to compare the simulations with mechanistic models such as those by Taitel and Dukler (1976), flow regime maps and correlations.

The simulations were run with a fully concentric annulus and periodic boundary conditions. Periodic boundary conditions were chosen in an attempt to alleviate the need for a much longer domain. The natural step in order to simulate a slug flow would be to construct a domain long enough to support several simultaneous slugs. Periodic boundary conditions circumvent this requirement by having a pseudo infinite pipe. The drawback is that there is limited room for redistribution of the liquid within the system, which in turn restricts the number of possible simultaneous slugs.

The pipe lengths studied were 3, 5 and 7 m. The pipe lengths were chosen to analyze the effect of the domain length on the solution. The Reynolds-averaged Navier–Stokes (RANS) implementation of the InterFoam solver within the OpenFOAM framework was used to run the simulations. The InterFoam solver which employs the volume of fluid (VOF) method has been shown to be applicable to a variety of complex flows such as jets (Deshpande et al., 2012), slug and annular flow (Shuard et al., 2016), droplets (Dianat et al., 2017) and t-junction risers (Tunstall and Skillen, 2016). The holdup profile and pressure gradient in particular will be compared with the experimental data collected at IFE.

2. Model

2.1. Geometry and mesh

The computational domain consists of a concentric annulus with an outer cylinder diameter (O.D) of 0.1 m, while the inner cylinder has a diameter (I.D) of 0.05 m. As mentioned, the 3 different domain lengths were used to investigate the effects of the amount of available liquid and number of slugs within the domain on the pressure gradient and liquid holdup profile.

Varying mesh densities were utilized to study the effect of the resolution on the solution. The coarsest mesh was designed with 108k cells/m while the finest mesh consisted of 400k cells/m. A comparison of the cross section of the extra coarse, very coarse, medium and very fine mesh are presented in Fig. 1.

The meshes shown in Fig. 1 and summarized in Table 1 were constructed in Gmsh and consist of two main regions, the near wall and the interior. Each cell expanding out from either cylinder grow thicker as they approach the constant cell thickness maintained within the rinterior area. The near wall cells are significantly refined in order to more accurately describe the flow in these regions. The shear flow which occurs close to the wall due to the no slip condition contributes to the instability of the interface and is therefore crucial to the overall flow development. The model utilizes a symmetry condition across the y-axis, which effectively halves the cell count. When combined with the

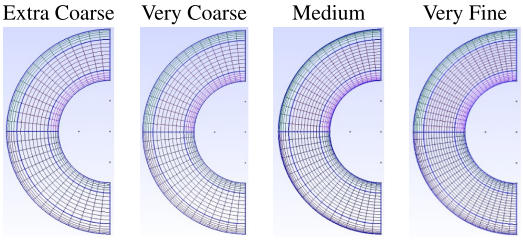

Fig. 1. Side by side comparison of increasing mesh density. Ref. Table 1.

Table 1
Mesh information.

Mesh	Circumference cells	Interior cells	Cells/m
E.Coarse	30	18	$102 \cdot 10^3$
V.Coarse	34	20	$150 \cdot 10^3$
Medium	36	24	$200 \cdot 10^3$
V.Fine	42	26	$400 \cdot 10^3$

utilized RANS model, the symmetry condition results in negligible loss of accuracy (Shuard et al., 2016).

The mesh information displayed in Table 1 summarizes the number of cells per meter, as well as along the circumference and within the interior region of each mesh. The mesh is built by placing hexahedral elements along transfinite lines. Transfinite lines are lines used to distribute the elements according to a chosen progression. There are transfinite lines placed along the circumference, along which the cells are evenly distributed. Additionally, there are transfinite lines connecting the inner and outer cylinder. Within the wall region a progression of 1.2 is applied, thus each cell is 20% larger than the preceding cell. Within the central interior region a constant cell sizing is employed. By carefully distributing the number of nodes along each transfinite line, the mesh sizing and element type can be controlled. This procedure ensures the exact placement of elements, thereby guaranteeing a precise match between the inlet and outlet.

The match between the inlet and outlet patches is important for any OpenFoam simulation using periodic boundary conditions. A poor match between two connecting patches such as the inlet and outlet can result in an alteration of the flow field during patch transfer.

3. Numerical method

The solver employed in this set of simulations was as previously mentioned the interFoam solver within OpenFoam. Although interFoam accepts a variety of turbulence models, these simulations used the k-ω RANS model in combination with periodic boundary conditions. The turbulence model solves for the kinetic energy (k) and specific dissipation rate (ω) by use of partial differential equations.

The InterFoam solver treats the mixture of the two fluids as a single imaginary fluid. In order to do so it applies mixture rules to determine the mixture velocity ($\bar{u}$), density ($\bar{\rho}$) and viscosity ($\bar{\nu}$). The mixture rule utilized in the InterFoam framework is described in Eq. (1). The average mixture velocity is determined as a function of the gas (u_g) and liquid (u_l) velocity, as well as the respective phase fractions (α_g, α_l).

$$\bar{u} = \alpha_g u_g + \alpha_l u_l, \tag{1}$$

the average mixture density and viscosity is solved by applying the same procedure.

If we consider the two fluids incompressible and apply the averaging procedure described in Eq. (1) to the fundamental conservation of continuity and momentum equations, the continuity equation can be simplified as

$$\nabla \cdot \bar{u} = 0, \tag{2}$$

and the corresponding momentum equation becomes

$$\frac{\partial \bar{u}}{\partial t} + \nabla \cdot (\bar{u}\bar{u}) = -\frac{1}{\bar{\rho}} \nabla p + \nabla \cdot (\bar{\nu}(\nabla \bar{u} + (\nabla \bar{u})^T)) + g + \frac{F_s}{\bar{\rho}}. \tag{3}$$

The terms p,g, and F_s denote pressure, gravity, and surface tension force respectively. A more comprehensive derivation and description of the solver can be studied in Lopes (2013).

By treating the two fluids as a single imaginary fluid, using Eqs. (2) & (3) the solver resolves the equations once for each iteration instead of repeating them for each phase. In order to keep track of the position and interface between the phases an indicator function, Eq. (4) is used in combination with an advection function Eq. (5) to predict the transport of the phase fluids. In general form, as described in Khalili et al. (2016) the indicator function (γ) is summarized as

$$\gamma = \begin{cases} 1 & \text{if cell is occupied by phase 1} \\ 0 < \gamma < 1 & \text{if phase 1 and phase 2 interfaces} \\ 0 & \text{if cell is occupied by phase 2,} \end{cases} \tag{4}$$

and the advection function takes the form of

$$\frac{\partial \gamma}{\partial t} + \nabla \cdot (\gamma \bar{u}) + \nabla \cdot (u_c \gamma (1 - \gamma)) = 0. \tag{5}$$

The last term on the L.H.S is an added term used to help with the conservation of phases by reducing numerical diffusion, which can cause smearing of the interface. Smearing is known to be a potential problem with VOF type solvers and can contribute to potential inaccuracy of the solution (Ubbink, 1997; So et al., 2011).

The term u_c, is an artificial interface compression velocity represented as a vector of the relative velocity of the two phases. The general form of the equation used to solve for interface compression velocity was suggested by Weller (2008) and is calculated as

$$u_c = min[C_\gamma |\bar{u}|, max(|\bar{u}|)] \frac{\nabla \gamma}{|\nabla \gamma|}. \tag{6}$$

As described in Berberovic (2010), the interface compression velocity is based on the maximum velocity within the interfacial area. The interface compression (C_γ) is a set constant, and in the case of this work it has been set at 0.8. The constant can theoretically take any value, values above 1 are considered enhanced compression, while a value of 0 is no compression, setting the value to 0 would as a result negate the term completely.

As a benefit of applying periodic boundary conditions, the values of the turbulent kinetic energy (k), specific dissipation (ω) and the initial flow field are only of importance at startup. As the simulation progresses, the values are continuously numerically solved. and updated to reflect the current flow. Therefore, only the initial phase fractions, viscosity and density are of significance to the reader, these are summarized in Table 2.

The surface tension (σ) which was measured during the experiment campaign and applied to the simulations was 0.0285 N/m. There was no initial pressure gradient or wave formations prescribed within the initial field. Instead an average mixture flow velocity of 3.6 m/s extracted from the experiment data was used as the periodic flow condition. The simulations are initialized as a stratified smooth flow, as such the pressure gradient and holdup profile undergo a transient at startup while the flow develops. The transient is caused by the sudden formation of a large slug that is not described by the initial conditions.

4. Simulations and results

The simulation cases presented in this paper were based on the holdup and velocity data obtained at IFE during their experiment campaign. The experimental setup at IFE includes 5 differential pressure transducers (DPT) distributed along the top of the annulus test section with an accuracy of ± 6 Pa, and an effective acquisition rate of 1.20 Hz. The 5th set is placed 36 and 39 m downstream of the phase inlets. The data collected at this test location is used as the basis for this work. In addition to the DPT there are 3 broad-beam gamma

Table 2
Fluid properties.

	Oil	Gas	Mixture	Units
α	0.53	0.47	1.0	
ν	$2.0 \cdot 10^{-6}$	$7.56 \cdot 10^{-7}$	$1.415 \cdot 10^{-6}$	$\frac{m^2}{s}$
ρ	801.0	23.82	–	$\frac{kg}{m^3}$

densitometers (GD) and 4 high speed cameras (HSC). The GD and HSC are used in order to acquire holdup data (GD) and aid with flow visualizations (HSC). The flow rates of the two phases are controlled at the inlet section. The data collected during the experiments serves as an excellent point of comparison for the annulus configuration simulations.

The simulation series were run using 4 different mesh densities and 3 pipe lengths. Periodic boundary conditions in combination with the chosen pipe lengths and mesh densities were utilized to study the effect of domain length and mesh density on the flow.

From the slug unit lengths observed in the experiments, a 7 m pipe should be able to produce two simultaneous slugs. Meanwhile, the 5 m pipe has more than sufficient liquid to support one slug while lacking the required liquid to produce two concurrent slugs. Lastly, the 3 m pipe has just enough liquid to support a single slug, which should result in a strong concentration of the slug frequency. Following this suggestion, both the 7 m pipe and 3 m pipe are expected to be an accurate representation of the experimental setup. Conversely, the 5 m domain should produce slugs at a lower frequency, due to restraints imposed on the system by the initial conditions in the form of available liquid. The tendency of domain size to have a direct impact on the flow when applied with periodic boundary conditions was also identified in Frank's work on air-water slug flow (Frank, 2005). Utilizing these domains and mesh densities, the effect of the number of slugs within the domain as well as the pressure gradient required to drive the flow were studied and compared with the experiments.

Due to the rapid growth of computational requirements tied to domain size, it is unrealistic to utilize all meshes for the 7 m domain. Therefore, the 7 m domain is restricted to the two coarsest meshes, while the shorter domains are run with all 4 mesh densities. To illustrate the time scaling associated with the grid sizing, the 5 m 400k cells/m mesh took 5 months to simulate a 30 s window on 20 cores, equivalent to roughly 75,000 CPU hours, while the coarsest mesh simulation lasted a mere 7 days for the same domain length.

4.1. Simulation and experiment phase distribution results

The holdup data collected at IFE was processed by their team using data from the gamma densitometers. As a result of the gas entrapment within the slugs, the liquid holdup will rarely indicate 100%. Caetano (1985) found that in an annulus configuration when a slug arises there are regions where the gas phase passes through the liquid, which is consistent with the collected data. As shown in Fig. 3, the fractional liquid holdup never reaches 1.0, instead it reaches a maximum of around 0.87.

A separate matter is that of small Taylor bubbles separating slugs, and also that of gas pockets entrapped within the liquid layer. A short Taylor bubble as seen in Fig. 2 can separate two slugs. It is important that these occurrences are correctly captured in the analysis. In the simulations the occurrence of large entrapped bubbles (Fig. 8) is a more immediate concern with regards to false positives. In the raw data, these phenomena look similar because the gamma densitometers measure the cross-sectional average holdups. However, it is imperative to distinguish the two because their effect on the flow is different. Two high holdup regions separated by a Taylor bubble should be interpreted as two separate slugs, while occurrences with smaller entrapped bubbles are counted as a single slug. Therefore, a combination of visual confirmation and statistics are used when determining slug frequency.

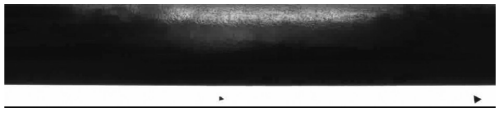

Fig. 2. Two slugs separated by a Taylor bubble.

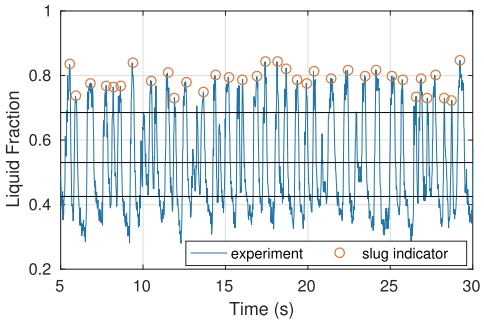

Fig. 3. IFE experiment holdup data, with slug indicators.

Fig. 2 shows a short Taylor bubble with a slug on either side. The image was captured at the 3rd camera location 37m downstream of the inlet. The HSC is placed between the DPT used to measure the pressure gradient. Short Taylor bubbles as shown in Fig. 2 will cause problems for a time based slug filter without careful attention to the parameters. The process used in this paper and by Nuland (1999) is more robust and effective at capturing such phenomena.

The original holdup data (Fig. 3) was processed using a statistical approach (Fig. 4) and visual confirmation. The same procedure was applied to the simulation data. The histograms and labeled slugs were compared with the visual data to ensure that they are consistent with regards to slug frequency. Note that the analysis was run on the full 100 s data set collected in experiment, while only 25 s are presented here for illustration purposes.

By applying filters to the data represented in Fig. 3 we can determine the number of slugs in the sample and the slug frequency. The filtering process follows the procedure described in Nuland's paper on slug analysis (Nuland, 1999). Two thresholds are determined along with the mean holdup. The thresholds are indicated by horizontal lines in Fig. 3. The mean holdup is determined as the average holdup of the time series at the sample point. In this experiment it was determined to be 0.53. The liquid fraction as well as average mixture velocity (3.6 m/s) was used as a basis for the subsequent simulations.

The two conditional holdups are determined using the mean holdup as the starting point. We isolate the data above and below the mean. Among the data points above the mean a conditional holdup is identified as the threshold which identifies a likely slug. For the simulation data, the slug thresholds are generally determined to be in the region of 70% liquid holdup.

Similarly, the data below the mean are used to determine the threshold for the bubble which separates slugs, this threshold is in the region around 40% liquid holdup. The indicator function for slugs will

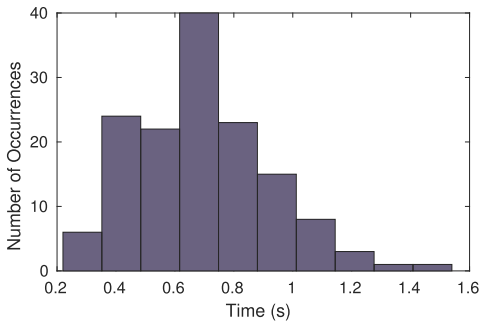

Fig. 4. Histogram of slug distribution from experiment.

only trigger for a new slug if the conditions for slug-bubble-slug transition has been met. Therefore, a new slug is only recognized if the holdup has gone from above the upper threshold, to below the lower threshold and back up again. The filtering process indicates the peak of each identified slug as shown in Fig. 3. The method ensures that there is no inherent time-based filter built into the slug detection, and it relies solely on meeting the necessary conditions as described. The method should detect the occurrence of small Taylor bubbles (Fig. 2) separating two slugs and correctly count them, at the same time it is unlikely that large waves will trigger the indicator function.

By applying the Nuland procedure to the raw data (Fig. 3), we can analyze the data using statistical principles to calculate the mean time interval and standard of the isolated slugs. As shown in Fig. 3, the period between slugs lies within a range of 0.2 to 1.5 s. The majority of them appear in the interval between 0.5 and 1.0 s. The calculated sample mean is 0.697 s (1.43 Hz) and the standard deviation is 0.2302 s. The statistical data matches well with the 20 s visual data captured by the high speed cameras. By applying the same methods used to analyze the experimental data to process the fractional liquid data of the 7 m domain represented in Fig. 5, we can determine the number of slug occurrences. The data analysis results in the identification of 33 slug formations within the 25 second time window of the developed flow field for both meshes. The slug frequency of 1.32 Hz indicates a match with the experimental data to within 10%. We will subsequently notice that the frequency is slightly lower than that observed in the 3 m domain (Fig. 12), and slightly higher than that which occurred in the 5 m domain (Fig. 10) for the same mesh densities.

The maximum holdup of 93.75% for the 102k cells/m mesh and near 99% for the 150k cells/m mesh is higher than that identified during the experiments. Most likely this is a side effect of mesh density and thereby an inability to resolve the small bubbles which permeate through the liquid layer in the experiments. Instead, there is a tendency for large bubbles to form either within the liquid subsequent to wave breaking (Fig. 8), or along the top wall separating the liquid from the wall (Fig. 9).

When we compare the histograms of the 7 m domain (Fig. 6) with the experimental results (Fig. 4), we notice that the bulk of the slug periods (Fig. 6) are concentrated in a span between 0.6 and 0.8 s for the 102k cells/m mesh.

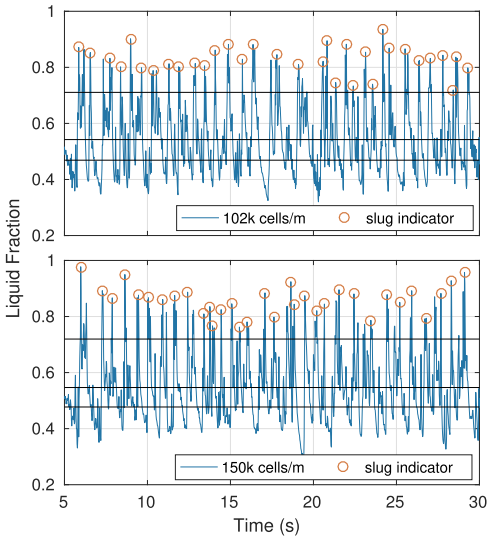

Fig. 5. Holdup profile as a function of time, 7 m pipe 108k cells/m.

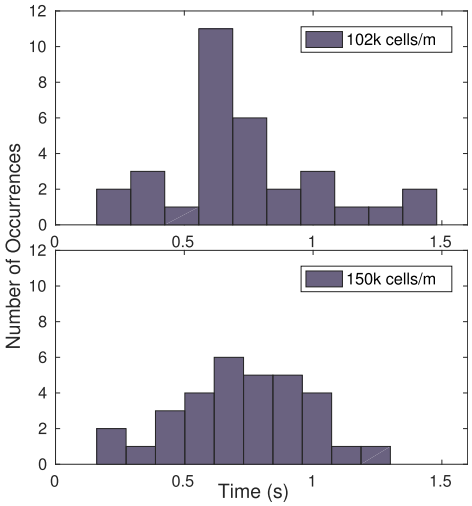

Fig. 6. Histogram of proto slug distribution within 7 m pipe.

The 150k cells/m mesh data spread is reminiscent of a standard distribution. The simulated slug periods ae similar to the experiment data. Most of the data lie between 0.4 and 1.0 s. The experimental mean of 0.697 s is reflected well in both simulations. Although it is possible to calculate a standard deviation, the number of sample points is too low for these simulations to give a meaningful representation of the distribution.

Furthermore, as shown for several of the subsequent cases and the 102k cells/m case, the distribution is not always Gaussian, therefore the standard deviation will not be summarized for the simulations. The mean peak interval is 0.757 s for both cases and match well with the experimental data, to within 10% as summarized in Table 3.

Even though the simulated slug frequency matches well with the experiments ($t = 0.697s$), we notice there are occasional gaps in the simulation data (Fig. 5). These gaps are the result of two proto slugs merging, after the merging there is a long period of time between holdup peaks. A proto slug is a precursor to a slug, often short, that may or may not develop into a stable slug. This merging behavior is most noticeable in the interval between 17 and 20 s of the 102k cells/m mesh (Fig. 5). With additional computational resources it will be possible to ascertain if the phenomenon is related to mesh density. As can be seen from this limited sample the behaviour is diminished in the 150k cells/m mesh.

The merging behaviour is apparent when inspecting a streamwise view of the domain. In Fig. 7, we see the process at which the flow regime quickly develops into two proto slugs from a smooth stratified flow at initialization. The transition from a single slug to two slugs is also clearly demonstrated. The domain appears short in the figure due to doubling the vertical scale for illustration purposes.

At t = 5, 20 and 25 s there is a single visible proto slug, while at t = 10, 15 and 30 s there are two distinct proto slugs at various stages of accumulation. At 10 s, the proto slug structures are depicted in the

Table 3
Summary of proto slug frequency for 7 m pipe.

Cells/m	t (s)	f (Hz)
102 k	0.76	1.32
150 k	0.76	1.32
exp.	0.70	1.43

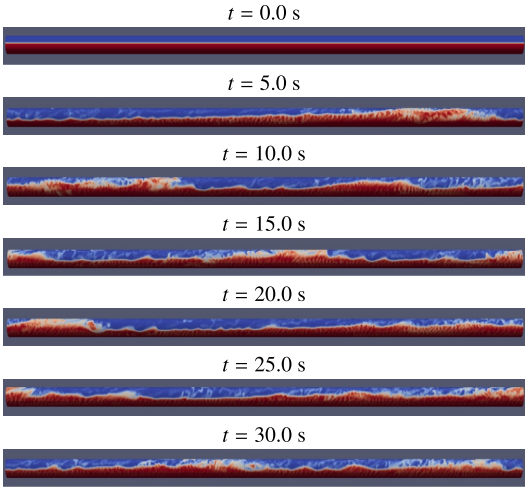

Fig. 7. Snapshots of streamwise phase field.

Fig. 8. Streamwise view of propagating slug.

liquid accumulation stage and nearly occupying the entire cross section at 15 s. Upon observation of the entire time series, the buildup and dissipation of slugs is a reoccurring process. The proto slugs are travelling faster than the waves and thus gathering liquid, which in turn contributes to the growth of the proto slug.

The process during which the liquid body both grows and entraps gas pockets is shown in Fig. 8. The proto slug is absorbing the smaller waves in front. As it absorbs these waves it is accumulating liquid at a faster rate than that which it is depositing liquid at the tail. There is a clear breaking of the front wave which entraps gas and creates gas pockets within the liquid.

If the streamwise cut (Fig. 8) is observed throughout the simulation, there is a noticeable excitation stage in which the proto slug grows and a relaxation period in which it dissipates. During excitation of the flow, the area in front of the accumulation region creates small ripples that grow into waves. The waves merge and create larger waves, and eventually this behavior forms a proto slug. During the dissipation phase, the area in front of the slug calms and the waves die out. This process is repeated and results in a periodic formation and dissipation of proto slugs.

If, instead, we monitor a cross-sectional cut (Fig. 9), it is clear that the bubbles are not dispersed into a swarm of small bubbles within the liquid layer, instead the gas tends to bunch together in large pockets. This contributes to the observed tendency where the liquid layer rarely reaches the top wall. The simulation lacks the resolution to resolve minor bubbles entrapped in the liquid layer. It is likely that this is the root cause of the gas layer we see separating the liquid from the upper wall in Figs. 9 and 7.

The cross section shown in Fig. 9 gives further context to the gas entrapment highlighted in Fig. 8. With further mesh refinement it is likely we would see a more prominent occurrence of small dispersed bubbles.

Although we classify the flow in the experiments as slug flow, this simulation, as well as subsequent meshes and pipe lengths rarely result in the liquid layer completely covering the cross section. This is due to the pockets of gas formed near the top wall. The experimental data gathered by gamma densitometry and visual recordings indicate that the liquid breaches the top wall intermittently, while also creating large gas pockets near the top wall after the slug front. We believe that the discrepancy between experiment and simulation occurs because the mesh is too coarse to resolve small gas bubbles within the liquid layer. The solver obeys the continuity equations and thereby pushes the gas phase toward the top creating large pockets of gas. The replacement of dispersed small bubbles with large gas bubbles will in turn reduce the effective viscosity (Pal, 1996; Pal and Rhodes, 1989; Anisa and Nour, 2010). The combination of the liquid not breaching the top wall and the decreased effective viscosity caused by a lack of small bubbles will lead to an undershoot of the maximum and mean pressure gradient solutions compared to the expected results. Conversely, the minimum values should be representative of the experiments.

Compared to the experiment (Fig. 3), the holdup profile peaks marked in Fig. 5 exist in the region between 80 and 90% holdup, with infrequent peaks above 90%, which is consistent with the 7 and 3 m

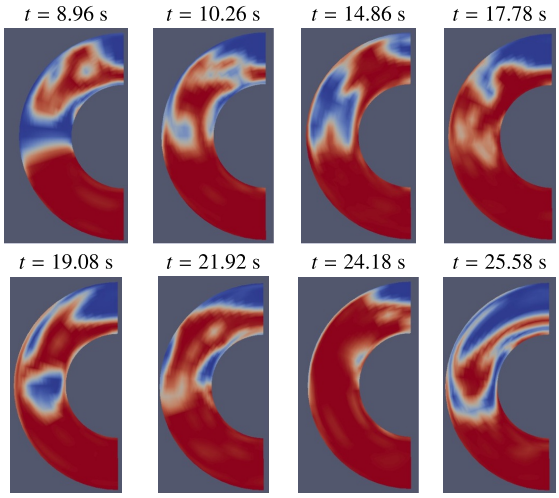

Fig. 9. Snapshots of phase field at selected peaks (Ref. Fig. 5).

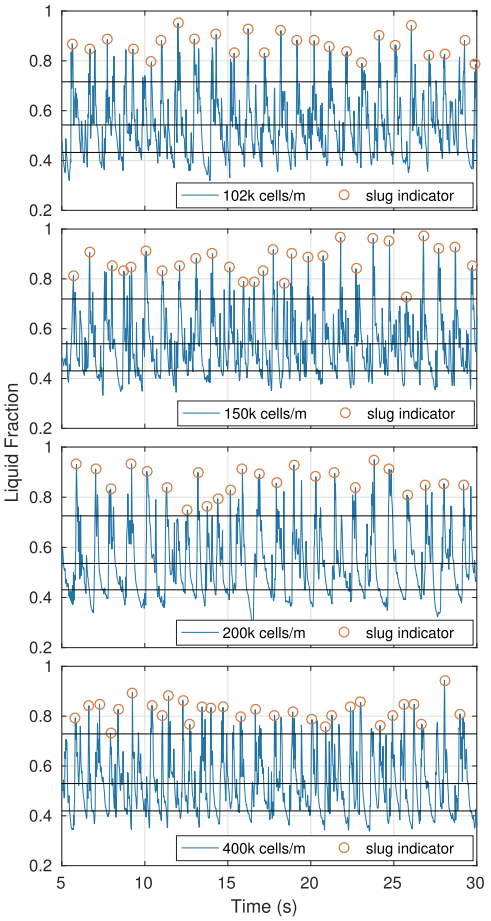

Fig. 10. Holdup profile as a function of time within 5 m pipe.

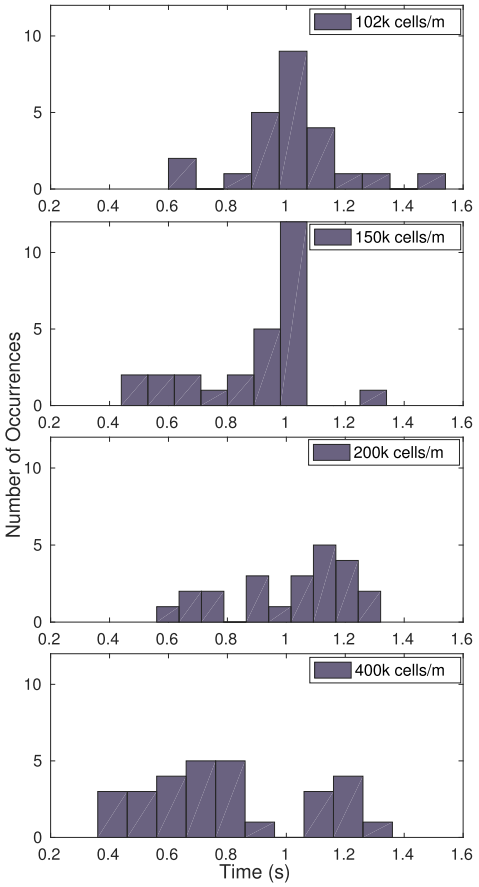

Fig. 11. Histogram of proto slug distribution within 5 m pipe.

simulations (Figs. 10 & 12).

When we compare the holdup profiles as shown in Fig. 10 and the corresponding histograms represented in Fig. 11 with those of the 7 m pipe in Fig. 5 and the experiment (Fig. 3), there is a distinct shift in the proto slug frequency as summarized in Table 4. We notice that, as the mesh is refined, the finer meshes are able to distinguish two slug frequencies. Fig. 10 shows that the two coarse meshes have slug occurrences concentrated around a 1 s interval while the two finer meshes are split between 0.5 and 1.3 s. Concurrent with the mesh refinement there is a distinct shift toward more high frequency slugs and a few low frequency slugs.

As we previously theorized, the 5 m domain is not suitable to accurately represent the slugging frequency of the experiment (1.43 Hz). The flow is likely near the production of persistent secondary proto slugs. As the secondary proto slug merges with the primary and creates one prolonged proto slug, two distinct frequencies are distinguished from the data, as shown in the histograms of the finer meshes (Fig. 11).

The additional liquid available within the domain introduces a strong presence of interfering structures such as waves which were not noted in either the 3 or 7 m simulation. The large waves produced in the 5 m domain are likely caused by the restriction imposed on the simulation by the domain length and initial conditions (I.C). Inspecting the visual data collected at IFE, there does not appear to be any visible large wave structures of this nature in the experiment.

Compared to both the 7 m (Fig. 6) and 3 m domain (Fig. 13) histograms, the statistical representation of the 5 m domain (Fig. 11) indicates a more irregular distribution of the slug period. For the 5 m case, it is apparent that the mesh has a visible effect on the time wise distribution, as shown the center of the most frequent bin(s) shifts from 1 s for the coarser meshes to 0.7 s for the finest mesh. In addition, there is an introduction of additional low frequency occurrences in the range around 1.2 s, a trend which coincides with the mesh refinement.

The overall statistics summarized in Table 4, indicate a reduction of the slugging frequency by 9 to 27% when compared to the 7 m domain, and 16 to 33% reduction compared to the experiment. This result exemplifies that although periodic boundary conditions are often described as simulating an infinite pipe, there are still domain specific artifacts introduced in strong periodic flow such as the slug regime which makes the domain length a critical consideration.

The data collected for the 3 m pipe as represented by Figs. 12 and 13 are statistically summarized in Table 5. They indicate that the frequency of slug occurrences remains relatively stable within a frequency range of 1.36-1.48 Hz, within 5% of the expected behaviour. Visually inspecting the individual mesh solutions (Fig. 12), there are no clear differences in the data sets.

Similarly, as with the 5 and 7 m domains, the vast majority of the

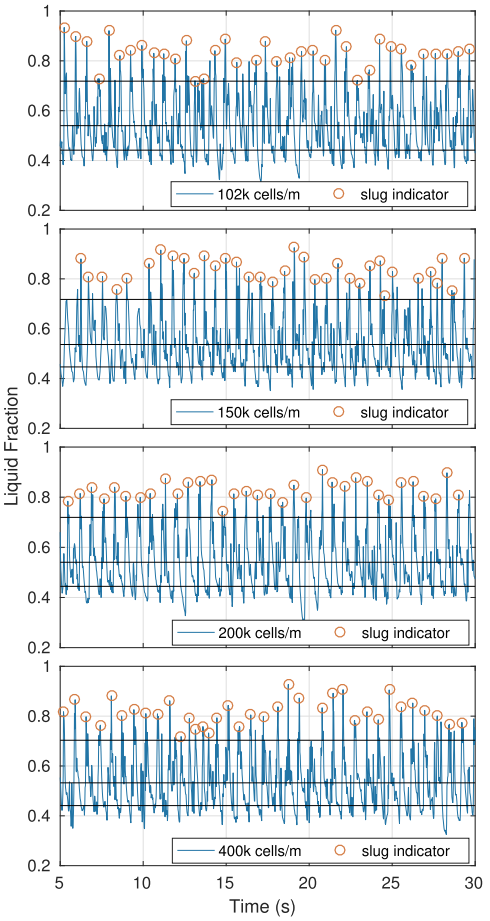

Fig. 12. Holdup profile as a function of time within 3 m pipe.

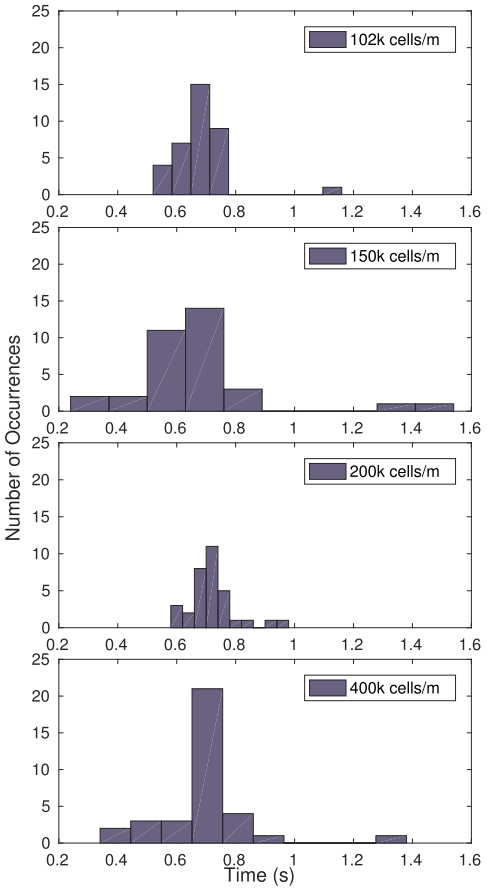

Fig. 13. Histogram of proto slug distribution within 3 m pipe.

Table 4
Summary of proto slug frequency for 5 m pipe.

Cells/m	t (s)	f (Hz)
102k	1.00	1.00
150k	0.89	1.12
200k	1.04	0.96
400k	0.83	1.20
exp.	0.70	1.43

Table 5
Summary of proto slug frequency for 3 m pipe.

Cells/m	t (s)	f (Hz)
102 k	0.68	1.48
150 k	0.71	1.40
200 k	0.74	1.36
400 k	0.69	1.44
exp.	0.70	1.43

slug occurrences exist in the region between 80 and 90% hold up, with some infrequent occurrences above 90%.

The data in Fig. 13 is concentrated for all meshes at the mean interval between 0.68 and 0.74 s (Table 5). When compared to the previous simulations this implies that the short domain imposes a very strong periodic behavior on the flow. As we originally hypothesized, the 5 and 7 m domains both contribute to alleviate this behaviour. For simulation purposes, without very good prior knowledge of the flow conditions it would be complicated to justify such a short domain. The domain has a significant impact on the slug frequency. We see this as the frequency clearly shifts between cases of different length. The 3 and 7 m domain are close to the expected behaviour, these domains were designed to closely replicate the length between slugs observed in the experiments.

4.2. Measured and simulated pressure gradient results

At IFE the pressure gradient was measured using differential pressure transducers. The data used in this paper was collected 36 and 39 m downstream of the inlet section at a frequency of 1.2 Hz. The pressure gradient data extracted from the simulations was the pressure gradient required to maintain the 3.6 m/s average mixture velocity established during the experiments. The recorded pressure gradient is a correction determined by the solver, as the solver attempts to determine the correction, it takes all the velocity components within the domain into consideration and determines a pressure gradient required to adjust the

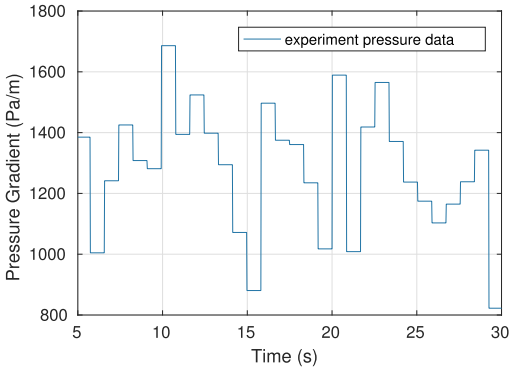

Fig. 14. Experiment pressure gradient as a function of time.

average velocity field of the domain to the set value. Therefore, the pressure gradient is not the differential of 2 points as in the experiments but rather numerically determined as the pressure gradient correction required to maintain the average mixture velocity. For this reason, with regards to the simulations, there is no inherit averaging tied to the length of the domain as could be the case for an experimental case. However, what may have an impact on the pressure gradient, is the number of slugs located within the domain, our hypothesis is as mentioned that the domain length should be close to an integer value of the slug to slug length to minimize the error.

Fig. 14 visualizes a 25 s segment of the experiment pressure gradient as a function of time while Fig. 15 displays the pressure gradient distribution in histogram form. The analysis is performed on the full 100 s data, however for purposes of consistency between experiment and simulation illustrations we only plot a 25 s segment. The periodic buildup of pressure caused by a passing slug and subsequent drop is clearly shown throughout the time lapse in Fig. 14. Keep in mind that due to the low sampling rate (1.2 Hz) it is complicated to compare trends such as frequency of pressure spikes with the simulation data (50 Hz), however maximum, minimum and mean pressure readings will be compared. In addition we will compare threshold data at which 5% of the data is above or below the threshold at both the high and low end of the data. We note that the maximum pressure gradient found in the experiment was 1785 Pa/m while the minimum was 822 Pa/m and the average 1286 Pa/m.

The histogram is used to put further context to the pressure gradient behaviour. The pressure data was originally 5000 data points, however the data collection procedure increases the number of samples artificially to match the holdup data points which results in repeat data.

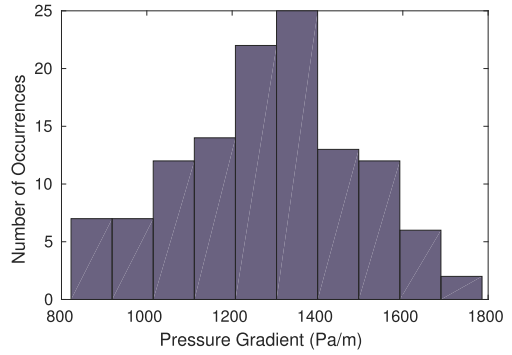

Fig. 15. Experiment pressure gradient histogram.

Therefore the sample is filtered to include each new sample, this reduces the amount of data points to 120. The pressure gradient distribution is centered at 1286 Pa/m and takes a shape resembling a Gaussian distribution.

Instead of using the extreme values for comparison we utilize a threshold at 5% and 95% of the data points to adjust for extreme outliers. These thresholds are the points at each end of the spectrum where 5% of the data is either lower or higher respectively than the threshold value. The 5% threshold is at 880.5 Pa/m while the upper threshold is at 1626.0 Pa/m. Using an upper and lower bound threshold to compare the pressure gradients of the simulations and experiments give a more robust comparison and it is less likely that the point represent an extreme outlier.

In the following sections we will present the pressure solutions for the 7, 5 and 3 m pipe along with the assorted meshes used for each domain length.

4.3. Long pipe (7 m)

Due to the time required to run a simulation for the 7 m domain with finer meshes, the 7 m domain simulation has been restricted to the two coarsest meshes, while remaining domain lengths utilize all 4 meshes.

As with the experiments we notice the oscillating behaviour associated with the buildup and drop off of the pressure gradient as the simulation attempts to maintain the constant average velocity of 3.6 m/s specified as the flow condition.

Similarly to the holdup solutions, we exclude the startup region prior to 5 s for the pressure gradient solution and compare the remaining data with the data gathered in experiment. The maximum and mean pressure gradient values are consistent with those observed in the collected experimental data (Fig. 14) while the minimum pressure gradient deviates significantly from the expected results.

The data summarized in Table 6 indicates that the 150k cells/m mesh performs better with regards to the pressure readings. Overall, the data collected for the two meshes are within 28% of the experiment data. The maximum and mean pressure data are accurately reproduced in the simulations. The relative errors are within 3–8% of the maximum readings and 1% of the mean. while the minimum pressure gradient is significantly higher than expected (19–29%).

In subsequent domains with refined meshes we will notice that typically the pressure gradient values decrease as the mesh is refined.

The extreme values of the experiments and simulations are not necessarily good points of comparison for the statistical behaviour of the flow. Therefore, in addition to the extreme values we utilize thresholds to more robustly evaluate the pressure behaviour.

In order to determine how similarly the solutions are behaving, we analyze the data using a statistical approach (Fig. 17). From this process we can say something about the distribution of the pressure data. The analysis offers a visual representation of both the mean and the extreme values at a glance. The data is summarized in Table 7 and shows that this approach, although still deviatory compared to the experiments, conforms to the trends noticed in the extreme value comparison.

The results summarized in Table 7 exemplifies a difference between the simulations and the experiments which is not readily available by looking at the max and minimum values as shown in Table 6. Although the general behaviour is consistent with the extreme values when using

Table 6
Summary of pressure gradient data for the 7 m pipe.

Cells/m	Mean (Pa/m)	Max (Pa/m)	Min (Pa/m)
102k	1295.4	1641.7	1058.2
150k	1299.7	1735.3	980.9
exp.	1286.0	1785.0	822.0

Table 7
Summary of pressure gradient histogram data for the 7 m pipe.

Cells/m	Mean (Pa/m)	95% (Pa/m)	5% (Pa/m)
102k	1295.4	1493.8	1127.3
150k	1299.7	1503.7	1114.8
exp.	1286.0	1626.4	880.5

a 5% threshold, it is clear that the bulk of the low and high pressure gradient results are closer to the mean, which results in a slightly larger gap than that seen from merely comparing the extreme values. Utilizing an approach which builds on a percentage of data points instead of extreme values gives a clearer picture of how the simulation pressure solutions are behaving compared to the experiments. The largest errors which are associated with the lower bounds are within 30% of the expected results, while the mean and upper bounds relative errors are significantly smaller, at approximately 1% and 8% respectively.

4.4. Medium pipe (5 m)

The 5 m pipe simulation results in a lower slugging frequency than the 3 and 7 m pipes but is still expected to exhibit similar trends with regards to the mean pressure gradient. In addition we would expect to see a prolonged pressure trough in the region between 25 and 27 s where the noted holdup drop was for the 150k cells/m mesh (Fig. 10).

Referencing Table 8 we notice a negative shift of the maximum, min and mean pressure gradient values from the 102 to 200k cells/m mesh solutions. The finest mesh has a minor pressure gradient increase when compared to the 200k cells/m mesh, for all recorded parameters. The trends hold true for both the extreme values (Table 8 and the threshold values (Table 9).

The extreme values are as mentioned not necessarily accurate representations as they could in some cases be an extreme outlier, for that reason we plot the data as histograms and find the 5 percentile threshold at either end of the spectrum.

The statistical representation of the pressure gradient solution shown in Fig. 19 clearly indicate that the mean values of the solution shift toward a lower value as the mesh density increases. We also notice that the front tail of the distribution closely follows a normal distribution pattern. The back tail of the histogram is cut short for the finer meshes. These types of distributions resemble a positive skew normal distribution. The behaviour is also present in the 3 m domain. By sorting the data in ascending order and choosing the 5 percentile data points at either tail of the data we can determine a more representative threshold for the high and low pressure boundaries, these thresholds are summarized in Table 9.

With regards to mesh dependency, there is no great difference between the relative errors of the mean,max and minimum pressure gradient data for the two finer meshes. However, there is significant discrepancy between the min and max relative errors with respect to the experiments as shown in Fig. 20 and Table 9. This particular case has a reduced slugging frequency due to restriction of available liquid tied to the length of the domain, which in turn will have an impact on the pressure solution. The solutions tend to stabilize as the mesh is refined and the gap between mean and extreme values stays relatively

Table 8
Summary of pressure gradient information for the 5 m pipe.

Cells/m	Mean (Pa/m)	Max (Pa/m)	Min (Pa/m)
102k	1316.7	1776.5	1023.4
150k	1276.0	1733.5	965.5
200k	1051.0	1448.0	840.2
400k	1069	1515.8	865.0
exp.	1286.0	1785.0	822.0

Table 9
Summary of pressure gradient information for the 5 m pipe.

Cells/m	Mean (Pa/m)	95% (Pa/m)	5% (Pa/m)
102k	1316.7	1495.6	1147.7
150k	1276.1	1518.6	1042.1
200k	1065.5	1267.7	910.8
400k	1074.0	1277.1	910.8
exp.	1286.0	1626.4	880.5

constant. We can conclude that for this domain length and slugging frequency the solution consistently undershoots the mean and maximum pressure gradients (Table 8). This could be a direct result of the reduced slugging frequency (Table 4) as it is the slugs that introduce the large pressure spikes.

There is a large pressure gradient drop of approximately 250 Pa/m from the 102k cells/m mesh to the 200k cells/m mesh, after which the solution stabilizes. A probable cause for this phenomenon is that the coarser meshes are not resolving some of the finer structures within the pipe. Surprisingly, the coarsest mesh is closest to the experiment results for the mean and minimum values. However, remember that this particular domain size does not accurately replicate the experimental slug frequency as seen in Table 4. As such, neither mesh is expected to give a particularly good replication of the experiment.

Overall, apart from the 102k cells/m mesh, the results were within 21.5% relative error with respect to the experiments.

4.5. Short pipe (3 m)

In the following figures and tables, we will compare the 3 m domain pressure behavior (Fig. 21) with that seen within the 5 and 7 m domains (Figs. 18 & 16) as well as experiment results.

Comparing the different meshes of the 3 m domain in Fig. 21, there are a few noticeable differences. Foremost, it is evident that the mean pressure gradient decreases as the mesh count increases (Table 10), which is consistent with the 5 m case (Table 8). The mean pressure gradient of the 102k and 150k cells/m mesh are and 1205.7 and 1263.6 Pa/m respectively. Comparatively the two finer meshes are 1065.5 and 1074 (Table 10).

Beyond the first 10 s the location of the minimums and maximum

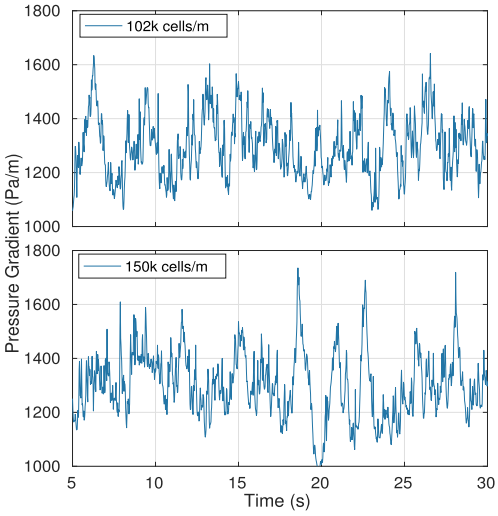

Fig. 16. Pressure gradient as a function of time, 7 m pipe 108k cells/m.

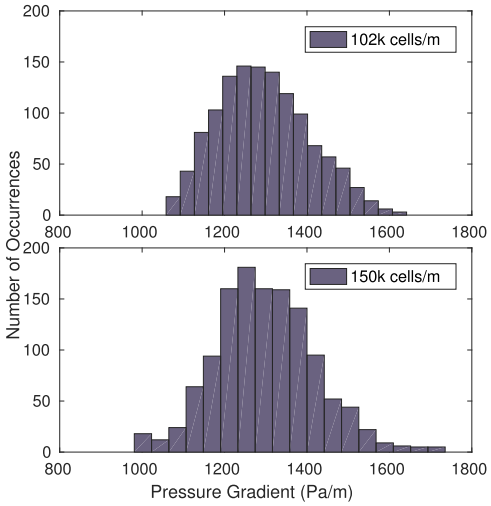

Fig. 17. Pressure gradient histogram, 7 m pipe.

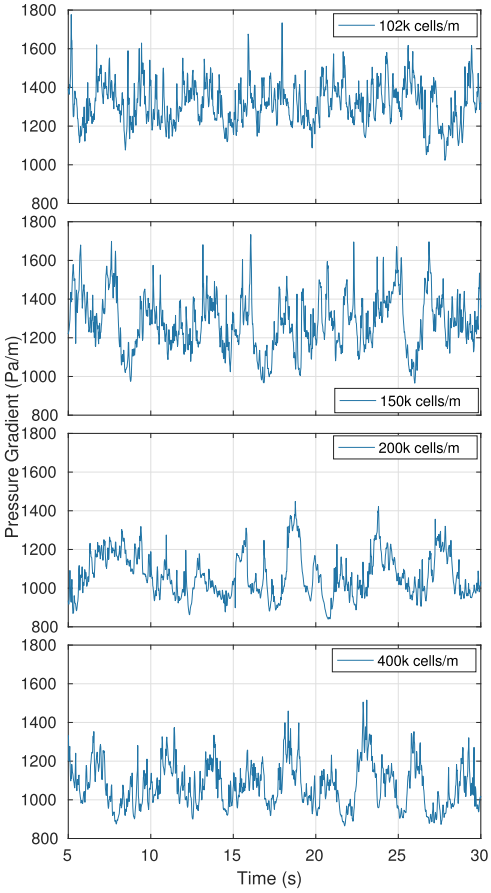

Fig. 18. Pressure gradient as function of time 5 m pipe.

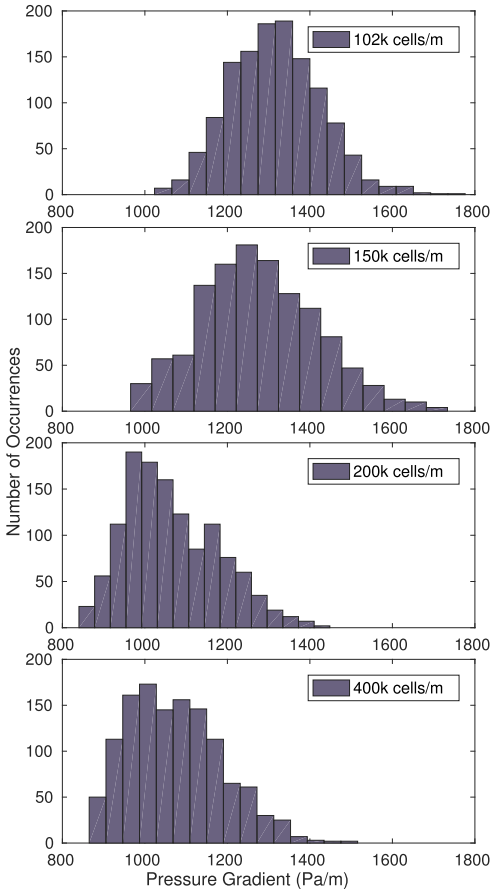

Fig. 19. Pressure gradient histogram, 5 m pipe.

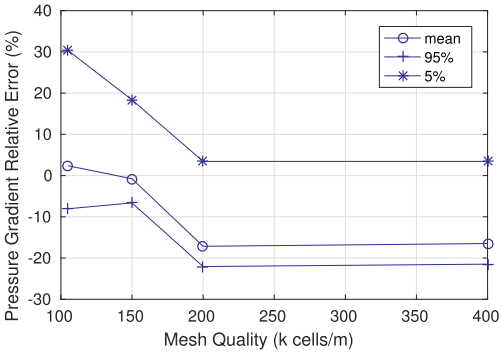

Fig. 20. Pressure gradient relative error as a function of cell count.

peaks are nearly synchronized in time as seen at the peak on either side of the 20 s mark. Also note that the maximum value (2241 Pa/m) recorded for the 150 k cells/m mesh is 400 Pa/m higher than any data point prior to it. If we were to exclude this data point, the maximum value would be in line with the trend of the remaining meshes as shown in Table 10.

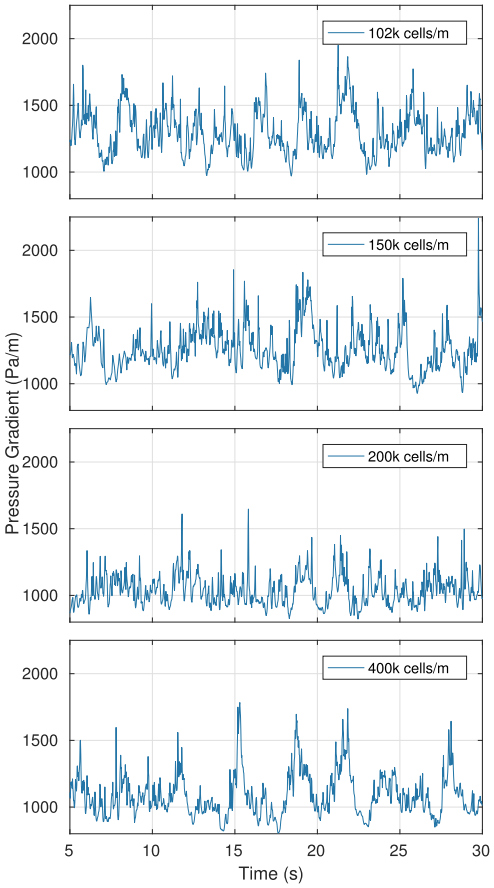

Fig. 21. Pressure gradient as a function of time within 3 m pipe.

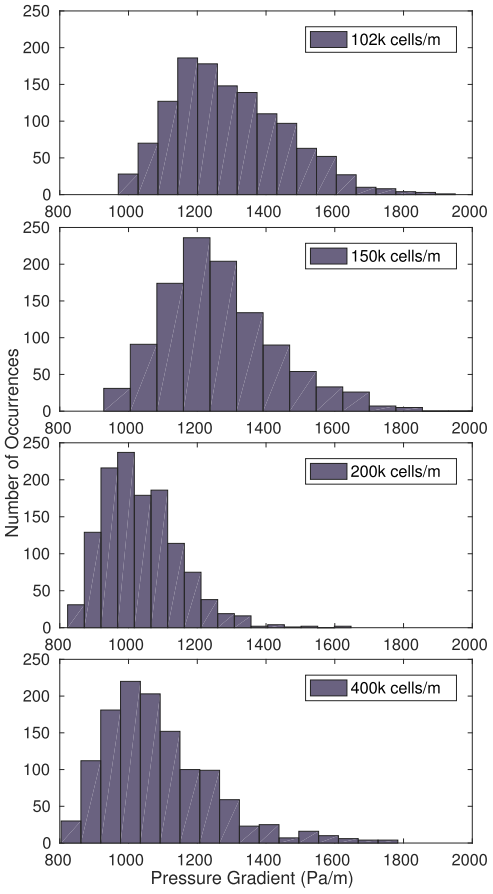

Fig. 22. Pressure gradient histogram, 3 m pipe.

Table 10
Summary of pressure gradient information for the 3 m pipe.

Cells/m	Mean (Pa/m)	Max (Pa/m)	Min (Pa/m)
102k	1295.7	1950.5	970.2
150k	1263.6	2241.1	927.9
200k	1037.5	1647.3	822.9
400k	1087.2	1783.5	803.9
exp.	1286.0	1785.0	822.0

From Table 10 we observe that the pressure gradient of the 3 m domain has undergone a shift when compared to the 5 m domain (Table 8). All the maximum pressure readings have increased and the minimum decreased. The maximum pressure gradient determined during the simulation of the finest mesh was 1783.5 Pa/m at 15.3 s. This is an excellent match to the experimentally determined maximum of 1785 Pa/m. Similarly, the minimal gradient observed in the simulations was 2.2% lower than the experimental value and was 803.9 Pa/m. The mean pressure gradient was lower than expected and averaged out to 1087 Pa/m which is 15.5% lower than the experimental value of 1286 Pa/m. This behavior is consistently noted throughout all domains.

The pressure gradient data shown in Fig. 22 indicates that all the 3 m solutions are resembling a positive skew normal distribution. The front tail seemingly closely follows a Gaussian distribution, however the back tail is cut short. Additionally, the histograms provide a visual representation of how the mean pressure gradient shifts towards a lower value as the mesh is refined. As with prior cases, we will sort the data and indicate an upper and lower 5% pressure threshold to adjust for extreme outliers.

As summarized in Table 11, the general trends noted from preceding cases holds true for the threshold data. As the mesh is refined the pressure gradients decrease. We suggest that the reason why the pressure solutions tend to undershoot is that there is a lack of dispersed small bubbles through the liquid layer. The gas bubbles formed are large and as a byproduct of conservation laws and buoyancy they tend to be pushed to the top, which hinders the formation of conventional slugs. The effect of this behavior on the pressure gradient would be twofold, not only would it reduce the effective viscosity, but also it

Table 11
Summary of pressure gradient information for the 3 m pipe.

Cells/m	Mean (Pa/m)	95% (Pa/m)	5% (Pa/m)
102k	1295.7	1589.8	1054.2
150k	1263.6	1574.3	1034.2
200k	1037.5	1231.4	890.5
400k	1087.2	1392.5	878.9
exp.	1286.0	1626.4	880.5

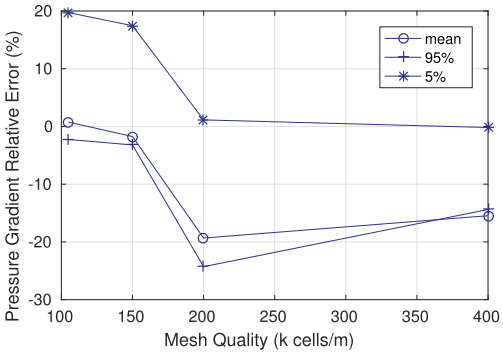

Fig. 23. Pressure gradient relative error as a function of cell count.

would reduce the pressure gradients as the liquid layer does not cover the cross section. Such behavior would most easily be noticed in the high pressure and mean pressure gradient readings while the minimum values should remain consistent with the experiments.

In the following figure we show that the relative error is a better match to the experimental values (Fig. 23) than what was observed in the 5 m mesh (Fig. 20).

The relative errors for the 3 m pipe show the same general trends as the 5 m pipe in terms of refinement behavior. The 150k cells/m mesh undershoot the maximum values by a marginal amount while dropping for the two finer meshes. There is a small improvement from the medium to the finest mesh for all 3 parameters, and overall the errors related to the 3 m case are smaller than those of the 5 m case

For the 3 m domain the best reproduction of experiment results are achieved by the 400k cells/m mesh. When comparing the results with the 5 m domain, we see that they both undershoot the mean value by approximately 15%, while the max and min values are better represented in the 3 m domain. This is an expected result because the 3 m domain closely replicates the distance between slugs. The finest mesh is within 15.5% error for all the recorded values.

Unfortunately, the 7 m case does not have a 200 nor a 400k cells/m simulation, as it would be interesting to compare the pressure solutions for the finest meshes of each case.

5. Conclusion

A series of simulations were run using OpenFOAM and the built in VOF type solver interFoam. The simulations were run using 3, 5 and 7 m long domains employing a concentric annulus configuration. The outer and inner diameters were 0.1 and 0.05 m respectively. The meshes varied from 102k cells/m to 400k cells/m. Due to the impact of mesh density on simulation time, the 7 m domain was only run with the 2 coarsest meshes. The data was analyzed with respect to pressure gradient and holdup profile and compared to experimental data.

During the course of these simulations we noticed a significant impact of the domain length on the slug frequency as well as on the pressure distribution. For both of the 3 m and 7 m domains, the simulation results compare favourably with the experimental data. As the mesh density increases there is a clear trend that the minimum and maximum pressure gradient values converge toward the experimental values of 1785 and 822 Pa/m respectively, the threshold data also show some signs of convergence however there is a larger gap for the maximum and mean data. The 3 m domain with a fine mesh maintained the 5% threshold minimum relative error to within 3% while the mean and max relative error were below 15.5%. For all cases the largest error associated with any of the extreme values or mean was within 30% including the outlier case of the 5 m pipe.

The simulation of the 3 m domain with a 400k cells/m mesh gave minimum, mean and maximum values of 803, 1074 and 1783.5 Pa/m respectively. Compared to the experimentally measured 822, 1286 and 1785 Pa/m, the extreme values are within 3% of the expected results. In general the simulations are better at predicting minimum values for the finer meshes than they are at predicting maximum mean values. A persistent trend is that as the mesh density is increased, the pressure gradients decrease. A likely reason the maximum and mean pressure gradients undershoot the expected results is that the proto slugs seen in the simulations rarely breach the top wall, in addition the lack of small bubbles within the liquid layer reduces the effective viscosity of the mixture. This effect would be much less prevalent in the minimum pressure gradient results as these readings would not be associated with proto slugs.

The slugging frequencies determined from the 3 m and 7 m domains are representative of the experiments in the sense that the slugging frequency lies within an error margin of 8% of the experiments. The 7 m domain results in a slugging frequency of 1.32 Hz, while the 3 m domain slug frequency lies within a range between 1.36 and 1.48 Hz depending on the mesh. For comparison, the experiments produced slugs at an average frequency of 1.43 Hz. This supports the initial hypothesis that slug flow in a concentric annulus can be studied using a computational representation of the experiments.

The 5 m domain, which is not long enough to include two slugs, did not reproduce the slug frequency nor the minimum or maximum pressure gradients measured in experiment. The result is that we observe large errors in at least 1 extreme value for each mesh for the 5 m domain as well as significant deviation in slug frequency between meshes and experiment result.

Based on the comparison between experimental and simulation data, in order to accurately replicate experimental data using periodic boundary conditions for a flow of a periodic nature such as slug flow, the of the domain must be considered. The computational domain should be approximately equal to an integer number of slug units (distance between two slug fronts or tails). In the case where the domain length is between 1 and 2 slug units such as the 5 m long domain, the slug frequency and pressure distribution will be imposed with an artificial restraint and not be an accurate representation of the physical domain.

We determined that for the sake of reproducing slug frequencies and pressure gradients within an annulus configuration, simulations are accurately able to represent the behavior within a physical pipe. Close attention is required when designing a simulation using periodic boundary conditions, as there are artificial restraints imposed on the simulation also by the initial conditions. In an ideal simulation, a much longer domain would be utilized, such that several slugs can form within the domain simultaneously. This would provide the best representation of a physical domain. However, with the computational demands such a simulation requires, we have attempted to simplify the simulations by using shorter domains and periodic boundary conditions. With this approach some information is needed on the physical flow conditions prior to attempting an accurate simulation.

As shown in the 5 m domain, large discrepancies are introduced when the computational domain is not representative of the experiment. In short, this means that simulations which utilize periodic boundary conditions are unlikely to be fully predictive unless they are also utilizing long domains accompanied with some prior knowledge of the flow conditions. Utilizing a very long domain comes with its own drawback of prohibitive simulation times. To counteract the computational demands related to a longer domain, we have attempted to accurately replicated experiment data using short domains accompanied with detailed knowledge of physical flow conditions.

Potential topics for future studies which are not covered in the current work are the effects of phase fractions, eccentricity, and fluid properties on the resulting flow pattern and characteristics. Each of these present challenging topics with the potential to drastically alter the resulting flow regime.

Acknowledgements

This work is part of a larger project called Multiphase Flow in Concentric and Eccentric Annulus Spaces (project number 255481) and has been performed thanks to funding from the Research Council of Norway through the PETROMAKS2 programme.

References

Anisa, A.I., Nour, A., 2010. Affect of viscosity and droplet diameter on water-in-oil (w/o) emulsions: an experimental study. Int. J. Chem. Mol.Eng. 4, 213–216.
Bellarby, J., Kofoed, S., Marketz, F., 2013. Annular pressure build-up analysis and methodology with examples from multifrac horizontal wells and hpht. SPEI/IADX Drilling Conference. Society of Petroleum Engineers, Amsterdam, Netherlands. https://doi.org/10.2118/163557-MS.
Berberovic, E., 2010. Investigation of Free-surface Flow Associated with Drop Impact: Numerical Simulations and Theoretical Modeling. TU Darmstadt Ph.D. thesis.
Bicalho, I., dos Santos, D., Ataíde, C., Duarte, C., 2016. Fluid-dynamic behavior of flow in partially obstructed concentric and eccentric annuli with orbital motion. Int. J. Heat Fluid Flow 137, 202–213. https://doi.org/10.1016/j.petrol.2015.11.029.
BP, 2010. Deepwater Horizon Accident Investigation Report. Technical Report.
Caetano, E., 1985. Upward Vertical Two-Phase Flow Through an Annulus. The University of Tulsa.
Chung, S., Sung, H., 2003. Direct numerical simulation of turbulent concentric annular pipe flow part 2: heat transfer. Int. J. Heat Fluid Flow 24, 399–411. https://doi.org/10.1016/S0142-727X(03)00017-1.
Chung, S., Sung, H., 2005. Large-eddy simulation of turbulent flow in a concentric annulus with rotation of an inner cylinder. Int. J. Heat Fluid Flow 26, 191–203. https://doi.org/10.1016/j.ijheatfluidflow.2004.08.006.
Colombo, M., Fairweather, M., 2015. Multiphase turbulence in bubbly flows: Rans simuilations. Int. J. Multiphase Flow 77, 222–243. https://doi.org/10.1016/j.ijmultiphaseflow.2015.09.003.
Deshpande, S., Anumolu, L., Trujillo, M., 2012. Evaluating the performance of the two-phase flow solver interfoam. Comput. Sci. Discovery 5, 47–55. https://doi.org/10.1088/1749-4699/5/1/014016.
Dianat, M., Skarysz, M., Garmory, A., 2017. A coupled level set and volume of fluid method for automotive exterior water management applications. Int. J. Multiphase Flow 91. https://doi.org/10.1016/j.ijmultiphaseflow.2017.01.008.
Ekberg, N., Ghiaasiaan, S., Abdel-Khalik, S., Yoda, M., Jeter, S., 1999. Gas-liquid two-phase flow in narrow horizontal annuli. Nucl. Eng. Des. 192, 59–80. https://doi.org/10.1016/S0029-5493(99)00078-3.
Escudier, M., Gouldson, I., Oliveira, P., Pinho, F., 2000. Eects of inner cylinder rotation on laminar ow of a newtonian ïuid through an eccentric annulus. Int. J. Heat Fluid Flow 21, 92–103. https://doi.org/10.1016/S0142-727X(99)00059-4.
Frank, T., 2005. Numerical simulation of slug flow regime for an air-water two-phase flow in horizontal pipes. The 11th International Topical Meeting on Nuclear Reactor Thermal-Hydraulics. Avignon, France
Gidaspow, D., Li, F., Huang, J., 2013. A cfd simulator for multiphase flow in reservoirs and pipes. Powder Technol. 242, 2–12. https://doi.org/10.1016/j.powtec.2013.01.047.
Hadžiabdić, M., Hanjalić, K., Mullyadzhanov, R., 2013. Les of turbulent flow in a concentric annulus with rotating outer wall. Int. J. Heat Fluid Flow 43, 74–84. https://doi.org/10.1016/j.ijheatfluidflow.2013.05.008.
Hasan, A., Kabir, C., 1992. Two-phase flow in vertical and inclined annuli. Int. J. Multiphase Flow 18, 279–293. https://doi.org/10.1016/0301-9322(92)90089-Y.
Hossain, A., Naser, J., Imteaz, M., 2011. Cfd investigation of particle deposition in a horizontal looped turbulent pipe flow. Environ. Model. Assess. 16, 359–367. https://doi.org/10.1007/s10666-011-9252-8.
Housz, E.I., Ooms, G., Henkes, R., Porquie, M., Kidess, A., Radhakrishnan, R., 2017. A comparison between numerical predictions and experimental results for horizontal core-annular flow with a turbulent annulus. Int. J. Multiphase Flow 95, 271–282. https://doi.org/10.1016/j.ijmultiphaseflow.2017.01.020.
Hua, J., Nordbø, J., Foss, M., 2014. Cfd modelling of gas entrainment at a propagating slug front. Proceedings of the 10th international Conference on CFD in Oil and Gas, Metallurgical and Process Industries. Sintef Proceedings, Trondheim, Norway.
Issa, R., Kempf, M., 2003. Simulation of slug flow in horizontal and nearly horizontal pipes with the two fluid-model. Int. J. Multiphase Flow 29, 69–95. https://doi.org/10.1016/S0301-9322(02)00127-1.
Jeong, J., Ozar, B., Dixit, A., Juliá, J., Hibiki, T., Ishii, M., 2008. Interfacial area transport of vertical upward air-water two-phase flow in an annulus channel. Int. J. Heat Fluid Flow 29, 178–193. https://doi.org/10.1016/j.ijheauitow.2007.07.00.
Julia, J., Hibiki, T., 2011. Flow regime transition criteria for two-phase flow in a vertical annulus. Int. J. Heat Fluid Flow 32, 993–1004. https://doi.org/10.1016/j.ijheatfluidflow.2011.06.001.
Julia, J., Ozar, B., Jeong, J., Hibiki, T., Ishii, M., 2011. Flow regime development analysis in adiabatic upward two-phase flow in a vertical annulus. Int. J. Heat Fluid Flow 32, 164–175. https://doi.org/10.1016/j.ijheatfluidflow.2010.09.003.
Kelessidis, V., Dukler, A., 1989. Modeling flow pattern transitions for upward gas-liquid flow in vertical concentric and eccentric annuli. Int. J. Multiphase Flow 15, 173–191. https://doi.org/10.1016/0301-9322(89)90069-4.
Khalili, M., Yahyazadeh, H., Gorji-Bandpy, M., Ganji, D., 2016. Application of volume of fluid method for simulation of a droplet impacting a fiber. Propul. Power Res. 5, 122–123. https://doi.org/10.1016/j.jppr.2016.04.003.
Knotek, S., 2014. Numerical simulation of multiphase flows in large horizontal pipes. Proceedings of the 17th International Flow Measurement Conference FLOMEKO 2016. International Measurement Confederation, Taipei, Taiwan.
Lopes, P., 2013. Free-surface Flow Interface and Air-Entrainment Modelling Using OpenFOAM. University of Coimbra:Department of Civil Engineering.
LP, E. S., 2014. Deepwater Horizon Blowout Preventer Failure Analysis Report.
Nuland, S., 1999. Bubble fraction in slugs in two-phase flow with high viscosity liquid. Proceedings of the 2nd International Symposium on Two-phase Flow Modeling and Experimentation. https://doi.org/10.1088/1757-899X/121/1/012018. Pisa, Italy
Pal, R., 1996. Effect of droplet size on the rheology of emulsions. Am. Inst. Chem. Eng. 42, 3181–3190. https://doi.org/10.1002/aic.690421119.
Pal, R., Rhodes, E., 1989. Viscosity/concentration relationships for emulsions. J. Rheol. 33, 1021–1045. https://doi.org/10.1122/1.550044.
Parsi, M., Azzopardi, B., Al-Sarkhi, A., Kesana, N., Vieira, R., Torres, C., McLaury, B., Shirazi, S., Schleicher, E., Hampel, U., 2017. Do huge waves exist in horizontal gas-liquid pipe flow? Int. J. Multiphase Flow 96, 1–23. https://doi.org/10.1016/j.ijmultiphaseflow.2017.06.007.
Pietrzak, M., Witczak, S., 2013. Flow patterns and void fractions of phases during gas-liquid two-phase and gas-liquid-liquid three-phase flow in u-bends. Int. J. Heat Fluid Flow 44, 700–710. https://doi.org/10.1016/j.ijheatfluidflow.2013.09.007.
Rzehak, R., Krepper, E., 2013. Cfd modeling of bubble-induced turbulence. Int. J. Multiphase Flow 55, 138–155. https://doi.org/10.1016/j.ijmultiphaseflow.2013.04.007.
Rzehak, R., Kriebitzsch, S., 2015. Multiphase cfd-simulation of bubbly pipe flow: a code comparison. Int. J. Multiphase Flow 68, 135–152. https://doi.org/10.1016/j.ijmultiphaseflow.2014.09.005.
Shuard, A., Mahmud, H., King, A., 2016. Comparison of two-phase pipe flow in openfoam with a mechanistic model. Proceedings of the IOP Conference Series: Materials Science and Engineering Volume 121. IOP Publishing Ltd, Trondheim, Norway. https://doi.org/10.1088/1757-899X/121/1/012018.
So, K., Hu, X., Adams, N., 2011. Anti-diffusion method for interface steepening in two-phase incompressible flow. J. Comput. Phys. 230, 5155–5177. https://doi.org/10.1016/j.jcp.2011.03.011.
Sorgun, M., Osgouei, R., Ozbayoglu, M., Ozbayoglu, A., 2013. An experimental and numerical study of two-phase flow in horizontal eccentric annuli. Energy Sources Part A 35, 891–899. https://doi.org/10.1080/15567036.2011.559524.
Taitel, Y., Dukler, A., 1976. A model for predicting flow regime transitions in horizontal and near horizontal gas-liquid flow. Am. Inst. Chem. Eng. 22, 47–55. https://doi.org/10.1002/aic.690220105.
Transocean, 2011. Macondo Well Incident.
Tunstall, R., Skillen, A., 2016. Large eddy simulation of a t-junction with upstream elbow: the role of dean vortices in thermal fatigue. Appl. Therm. Eng. 107, 672–680. https://doi.org/10.1016/j.applthermaleng.2016.07.011.
Ubbink, O., 1997. Numerical Prediction of Two Fluid Systems with Sharp Interfaces. Imperial College.
Valle, C., Hohne, T., Prasser, H., Shnel, T., 2008. Experimental investigation and cfd simulation of horizontal stratified two-phase flow phenomena. Nucl. Eng. Des. 238, 637–646. https://doi.org/10.1016/j.nucengdes.2007.02.051.
Verdin, P., Thompson, C., Brown, L., 2014. Cfd modelling of stratified/atomization gas-liquid flow in large diameter pipes. Int. J. Multiphase Flow 67, 135–143. https://doi.org/10.1016/j.ijmultiphaseflow.2014.07.008.
Weller, G., 2008. A New Approach to VOF-based Interface Capturing Methods for Incompressible and Compressible Flow. Technical Report.
Wongwises, S., Pipathattakul, M., 2006. Flow pattern, pressure drop and void fraction of two-phase gas-liquid flow in an inclined narrow annular channel. Exp. Therm. Fluid Sci. 30, 345–354. https://doi.org/10.1016/j.expthermflusci.2005.08.002.
Xiang, M., Cheung, S., Yeoh, G., Zhang, W., Tu, J., 2011. On the numerical study of bubbly flow created by ventilated cavity in vertical pipe. Int. J. Multiphase Flow 37, 756–768. https://doi.org/10.1016/j.ijmultiphaseflow.2011.01.014.
Xin, R., Awwad, A., Dong, Z., Ebadian, M., 1997. An experimental study of single-phase and two-phase flow pressure drop in annular helicoidal pipes. Int. J. Heat Fluid Flow 18, 482–488. https://doi.org/10.1016/S0142-727X(97)80006-9.
Xing, L., Yeung, H., Shen, J., Cao, Y., 2013. Numerical study on mitigating severe slugging in pipeline/riser system with wavy pipe. Int. J. Multiphase Flow 53, 1–10. https://doi.org/10.1016/j.ijmultiphaseflow.2013.01.003.
Zambrano, H., Sigalotti, L., Klapp, J., Polo, F., Bencomo, A., 2017. Heavy oil slurry transporation through horizontal pipelines: experiments and cfd simulations. Int. J. Multiphase Flow 91, 130–141. https://doi.org/10.1016/j.ijmultiphaseflow.2016.04.013.

Paper II

Two-phase flow simulations at $0 - 4^o$ inclination in an eccentric annulus

C. Friedemann, M. Mortensen, J. Nossen

Published in International Journal of Heat and Fluid flow, June 2020, volume 83,
DOI:10.1016/j.ijheatfluidflow.2020.108586

II

International Journal of Heat and Fluid Flow 83 (2020) 108586

Contents lists available at ScienceDirect

International Journal of Heat and Fluid Flow

journal homepage: www.elsevier.com/locate/ijhff

Two-phase flow simulations at $0 - 4^o$ inclination in an eccentric annulus

C. Friedemann[*,a], M. Mortensen[a], J. Nossen[b]

[a] Department of Mathematics, University of Oslo, Moltke Moes vei 35, Oslo 0851, Norway
[b] Institute for Energy Technology, Kjeller 2007, Norway

ARTICLE INFO

Keywords:
Annulus
Slug flow
Wavy flow
Volume of fluid
Reynolds-averaged Navier-Stokes equations

ABSTRACT

Co-current two-phase simulations of gas-liquid flow with mixture velocities from 1.2 to 4.2 m/s were run in a partially eccentric annulus and compared with entirely eccentric and concentric experimental data collected at the Institute for Energy Technology in Norway. The gas-phase was sulphur hexafluoride (SF_6) for all cases, while the liquid-phase was Exxsol D60 for the horizontal cases and a mixture of Exxsol D60 and Marcol 82 for the inclined case. The outer diameter of the annulus was 0.1 m for all cases, while the inner diameter was 0.05 m in the horizontal configuration and 0.04 m for the inclined configuration. The purpose of this paper is to explore the effect of the holdup fraction, mixture velocity, and interior pipe's position on the pressure gradient and flow regime, in effect a study of the pressure gradient and holdup fraction transients. The comparisons between simulations and experiments indicate that moving the pipe from an entirely eccentric to the partially eccentric configuration has a drastic impact on the pressure gradient. In all 4 cases where the inner pipe was changed from a completely eccentric geometry in the experiments to a less eccentric configuration in the simulations, we notice an increase of 48–303% of the mean pressure gradient. Comparatively, the 4 cases where the pipe was moved from a concentric experimental configuration to a more eccentric configuration in the simulations result in less drastic pressure gradient changes. Two cases were within 22% of the experimental results for mean, maximum, and minimum pressure gradient, while the last two cases exceeded the minimum and mean pressure gradients by 25–250%, respectively. The flow regime is rarely significantly affected by a change in eccentricity; 2 out of the 8 horizontal cases indicate either a transition from wavy flow to slug flow or significantly larger waves. The most prominent and frequent discrepancies identified were altered slug and wave frequencies. The last case, a 4^o inclined, partially eccentric simulation was compared to an entirely eccentric experiment and results in a 0.2 Hz increase in wave frequency, up from the experimental 0.56 Hz and a 49% increase in the mean pressure gradient.

1. Introduction

The modern-day study of two-phase and multiphase flow was spurred on by the discovery of oil and gas and the worldwide dependence on fossil fuels to power not only our cars and planes but countless other applications of everyday life.

The topic of this paper, which is two-phase flow within an annulus, has direct applications to oil and gas extraction. However, the intentional usage of the annulus geometry is prevalent in several industries beyond petroleum. One example is nuclear reactors. Sato et al. (2013) studied loss of coolant during an accident, which is highly applicable to the oil and gas industry, because of the similarities to a leak or rupture along a petroleum pipeline. The conducted studies go past environmental aspects, and there are several papers on the utilization of annular fuel rods concerning internal and external cooling, for example, Deokule et al. (2015) and Blinkov et al. (2010). There are also more fundamental flow studies, such as the velocity distribution within the annular mixing chamber (Sun et al., 2017).

Two-phase pipe flow is a rigorously studied subject within the field of petroleum engineering. It is well known that two-phase flows and flow regimes are highly dependent on fluid composition, flow rates, and pipe inclination. Inclined pipe flow is less studied than horizontal and vertical configurations. However, the literature covers topics such as slug frequency (Perez et al., 2007; Hout et al., 2003; Schulkes, 2011), holdup profile (Beggs and Brill, 1973; Bonnecaze et al., 1971), pressure drop (Strazza et al., 2011; Salem, 2008; Ilic, 1986; Ghajar and Bhagwat, 2014), mechanical losses (Liu et al., 2015) and flow regime (Archibong-Eso et al., 2016; Oddie et al., 2003).

Although we frequently find these topics in the body of work related to two-phase flow, the subjects are rare when studying the annulus

* Corresponding author.
E-mail address: chrisjfr@student.matnat.uio.no (C. Friedemann).

https://doi.org/10.1016/j.ijheatfluidflow.2020.108586
Received 22 November 2019; Received in revised form 14 February 2020; Accepted 5 March 2020

Abbreviations

IFE	Institute for Energy Technology
VOF	Volume of Fluid
G	Gamma densitometer
DP	Differential pressure transducer

Subscripts

s	Superficial
g	Gas
l	Liquid
c	Compression
m	Mixture
0	Incident beam

Constants and variables

α	Liquid fraction
d	Distance between cylinder centroids (m)
E	Eccentricity
R_o	Radius of outer cylinder (m)
R_i	Radius of inner cylinder (m)
$\bar{u}$	Mixture velocity (m/s)
$\bar{\rho}$	Mixture density (kg/m^3)
p	Pressure (Pa)
$\bar{\nu}$	Viscosity (m^2/s)
g	Gravity (m/s^2)
F	Surface tension force
σ	Surface tension (N/m)
γ	Gamma beam intensity
μ	Linear attenuation coefficient (cm^{-1})
D_h	Hydraulic diameter (m)
k	Turbulent kinetic energy
ω	Specific dissipation rate (m^2/s^2)

configuration specifically. Although the annulus configuration is a well-known problem, the existing literature on the topic is not as extensive nor as rigorous as it is for a conventional pipe geometry. Therefore, this paper will revolve around the aspect of eccentricity of the annulus and its potential effect on the flow regime, holdup pattern, and pressure gradient.

One of the earliest works applicable to the problem at hand presented in this paper was the modeling of frictional pressure drop and was performed in the late 1940s by Lockhart and Martinelli, a model which was later expanded by Chen and Spedding (1981). The original model was based on correlations and was the result of a study into separated two-phase flows. Correlation models are prone to errors when the case falls outside the original scope of the measurements used to develop the model, yet may produce reliable results when used appropriately.

Some of the earliest annulus studies originated in the 1960s as Denton (1963) completed his Master's thesis on the topic of turbulent flow in concentric and eccentric annuli. During the same period, Michiyoshi and Nakajima (1968) studied fully turbulent flow in a concentric annulus, while Vaughn (1963) and Wein et al. (1970) both studied non-Newtonian fluids in annuli. Although most of the early publications related to the annulus configuration concentrated on single-phase flow, it signaled the beginning of an emerging field of study.

By the mid-1970s, there was significant progress in terms of prediction and modeling of flow regimes. Taitel and Dukler (1976) worked on flow regime transitions for two-phase gas-liquid flow, and presented a generalized flow regime map, while Hanks and Bonner (1971) studied the specifics of laminar flow stability in a concentric annulus. However, as was the case in the previous decade, the 1970s saw consistent work on single-phase flows, and the majority of the efforts focused on the use or development of correlations.

The 1980s continued in the same trend as the preceding decade; among the publications were further works mapping out annulus flow regimes (Kelessidis and Dukler, 1989; Caetano, 1985). Also, new correlations and models for flow behavior in different configurations, including annulus, were developed (Høyland et al., 1989; Dukler and Taitel, 1986; Taitel et al., 1980). In addition, Kelessidis and Dukler (1990) studied the motion of large gas bubbles passing through the liquid in vertical annuli.

During the late 1990s, Iyer and Vafai (1998) conducted simulations of buoyancy induced flow in an annulus, outlining the effect of between 1 and 4 perturbations of the wall within the domain. Iyer's work on computational fluid dynamics related to the annulus configuration was one of the first publications which utilized CFD to study the annulus configuration. Simultaneously, Buyruk et al. (1999) studied the theoretical heat transfer in laminar flow within a concentric annulus. Several researchers conducted experimental studies of multiphase flow behavior. Harvel et al. (1999) studied the different flow regimes in a vertical annulus by using optical techniques such as X-ray and tomography. Escudier et al. (1995) studied non-Newtonian fluids in a concentric annulus while concurrent studies on void fraction (Hasan and Kabir, 1992), as well as the rise velocity of Taylor bubbles (Das et al., 1998; Hills and Chéty, 1998) were published.

By the 2000s, technology had finally advanced to the point where CFD simulations became noticeable in the literature with regards to annulus flow. Simulations were published focused on turbulent flow and heat transfer (Nikitin et al., 2009) as well as natural convection (Adachi and Imai, 2007; Mizushima et al., 2001; Yoo, 2003; Yu et al., 2005). Along with a new influx of simulation-based studies concerning the annulus configuration, there was a significant uptick in published experimental research. Asymmetric phase distributions (Das et al., 2000), flow structures in a vertical annulus (Hibiki et al., 2003; Ozar et al., 2008), flow pattern and pressure drop in an inclined annular channel (Wongwises and Pipathattakul, 2006) and convection in a vertical eccentric annulus (Hosseini et al., 2009) were among the published works.

Even though flow in an annulus has been studied since the early 1960s, the recent increase in interest for the annulus configuration is natural because of its prevalence in industry combined with technological advances. Because the annulus configuration is frequently present in industries with potential for significant adverse environmental impacts, such as petroleum and nuclear, it is logical that the topic is of lasting interest to engineers and researchers. It is imperative to better understand not just the statistics, but also the physics related to multiphase flow in annuli to help mitigate and prevent environmentally damaging accidents.

To better understand and predict the behavior of two-phase flow within an annulus, we compare simulations performed in OpenFOAM using the Volume of Fluid type solver interFoam with experimental data from Institute for Energy Technology (IFE) in Norway. The experiments are conducted in a fully concentric or eccentric configuration. We use experimental data such as averaged phase velocities and holdup fraction as initial conditions; however, we alter the domain utilized in the simulations to study the potential effect of the interior pipe's location. The change in the interior pipe's relative location to the outer pipe, means we do not expect for the simulations to be replications of the experiments, but rather wish to study how it affects the flow.

Additionally, we pair each simulation with another simulation of the same phase-averaged velocity but different holdup fraction. The simulation pairings allow us to study the effect of the holdup fraction itself on the resultant flow regime and pressure behavior.

The outcome of the simulations is a set of holdup and pressure gradient transients for each partially eccentric simulation, which are compared with experimental data of concentric or entirely eccentric configurations. The transients allow us to study the frequency and size of slugs and waves as well as the minimum, mean and maximum pressure gradients, which are relevant for both flow assurance purposes as well as pipeline maintenance and design.

2. Geometry and mesh

The annulus geometry is defined by the enclosed inner cylinder and its location compared to the outer cylinder. Their relative locations define the parameter known as eccentricity, which is one of the factors along with holdup fraction, which we will investigate to what degree affects the flow.

The eccentricity (E) is determined based on the location and dimensions of the two cylinders as illustrated by Fig. 1 and described by

$$E = \frac{d}{R_o - R_i}. \tag{1}$$

When the annulus is fully concentric, the eccentricity is always $E = 0$, while for an entirely eccentric annulus, the ratio is always $E = 1.0$.

We construct the simulation domains in Gmsh. Gmsh is a robust meshing tool which interfaces well with OpenFOAM. Through Gmsh, we define the separate regions of the mesh. The two circles that represent the inner and outer cylinder are subject to the no-slip condition, and they are connected by transfinite lines that originate at predefined points along the circumference. Each transfinite line connecting the two cylinders contains three sections. We refer to these sections as the central region and inner and outer wall region. The wall regions form a significantly refined 5 mm thick concentric belt around each cylinder (Fig. 2).

The cylinder wall and wall refinement regions are also transfinite lines. A transfinite line may be used as part of the structural domain, as is the case of the cylinder walls, or solely for its functionality. The functionality of the transfinite line command is to define the number of mesh points along the line. When properly paired such that each region forms a quadrilateral of transfinite lines, it gives the user control over the type of element within the region. The drawback of utilizing the transfinite line function is that it prefers having the same number of nodes either side of the line, we consider this to be a soft restriction as it can be bypassed by allowing skewed elements.

The eccentric configuration results in a narrow gap separating the cylinders, the combination of an eccentric configuration and OpenFOAM's preference for hexahedral elements means we have to choose between having minuscule elements within the gap or circumvent the transfinite line node restriction. We have chosen to reduce the number of elements within the narrow gap by allowing some cell distortion, as shown in Fig. 2.

Allowing these distorted elements circumvents having the same number of cells in each mesh region within the interior; however, it introduces additional cell skewness and distortion.

Each mesh is quality assured using the built-in commands in OpenFOAM, and they are well within acceptable limits for simulation in terms of non-orthogonality and cell skewness. The maximum and average non-orthogonality for any mesh is 55 and 15 degrees, while the cell skewness maximum is ~ 0.5. OpenFOAM advice that meshes should be below 70 degrees non-orthogonality and below 4 for cell skewness. Through the case directory, the solver is instructed to perform two specific correction steps to the pressure solution to minimize any effect the non-orthogonality and cell skewness may have on the simulations.

The domain utilized for the horizontal simulations is 7 m long. In the case of the inclined simulation, the domain is 5 m long, and the direction of gravity rotated so that the inclination is 4 degrees.

Finally, we utilize the mesh in combination with periodic boundary conditions, which allows the flow to transfer seamlessly from the outlet to the inlet. No-slip was applied at the cylinder walls, while we define the centerline as a symmetry plane. We used the k -ω turbulence model, which is a well-documented closure method for the Reynolds-averaged Navier-Stokes equations.

3. Fundamental equations and interFoam

The OpenFOAM solver interFoam is based on a two-phase Volume of Fluid (VOF) model, which utilizes an imaginary mixture fluid instead of solving one equation for each phase. In this work, we introduce a simple modification to the standard interFoam solver to adjust for periodic boundary conditions in an inclined pipe by uncoupling the gravity term from the pressure equation.

A mixture velocity, sometimes referred to as phase-averaged velocity $\bar{u}$, is calculated by applying the following mixture rule

$$\bar{u} = (1 - \alpha)u_g + \alpha u_l, \tag{2}$$

where α is the phase fraction of liquid in the computational cell. The phase fraction (or indicator function) α is described as

$$\alpha = \begin{cases} 1 & \text{if cell is occupied by liquid} \\ 0 < \alpha < 1 & \text{if cell contains both gas and liquid} \\ 0 & \text{if cell is occupied by gas.} \end{cases} \tag{3}$$

The value assigned to each cell is thus based on the fraction of the fluid contained within this cell. The function returns a value of 1 if the cell contains only liquids and 0 if the cell is filled with gas. The indicator function α is solved for in a modified advection equation

$$\frac{\partial \alpha}{\partial t} + \nabla\cdot(\alpha\bar{u}) + \nabla\cdot(u_c\alpha(1 - \alpha)) = 0, \tag{4}$$

where the interface compression velocity, u_c, is used to artificially "compress" the surface, thus maintaining a sharp interface between the two phases.

With phase-averaging in place, the governing momentum and continuity equations can be written as

$$\frac{\partial \bar{u}}{\partial t} + \nabla\cdot(\bar{u}\bar{u}) = -\frac{1}{\bar{\rho}}\nabla p + \nabla\cdot(\bar{\nu}(\nabla\bar{u} + (\nabla\bar{u})^T)) + g + \frac{F}{\bar{\rho}}, \tag{5}$$

$$\nabla\cdot\bar{u} = 0, \tag{6}$$

where $\bar{\rho}$, $\bar{\nu}$, and F represent mixture density, viscosity, and surface tension force, respectively. The calculation of the mixture components follows the same mixture rule as exemplified in Eq. (2).

The benefit of the VOF approach is that the momentum and continuity equations are solved once for the mixture fluid instead of once for each phase. The drawback is that some information about the behavior of each phase is lost. With regards to both the VOF solver and the

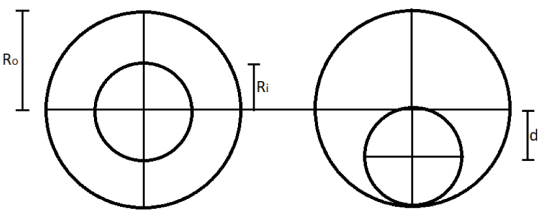

Fig. 1. Eccentricity of annulus, R_o = outer cylinder radius, R_i = inner cylinder radius, d = distance between cylinder centers, concentric (left) and fully eccentric (right).

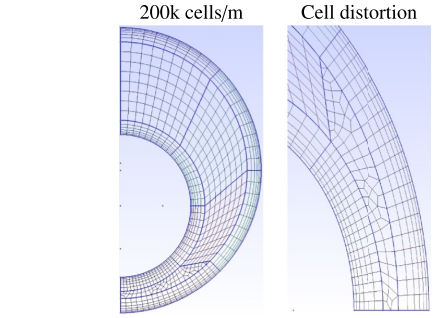

Fig. 2. Cross-section (left) and dummyTXdummy– zoomed in view of skewed cells within rotated narrow gap (right).

interface compression, Desphande et al. (2012) and Berberovic (2010) offers an in-depth description.

4. Experimental setup

We compare the simulations with experimental data gathered from fully concentric and eccentric annuli in a medium scale (45 m long and 99 mm inner diameter) flow loop at IFE. Note, that the inclined experiments are performed in a shorter flow-loop, with the same type of testing equipment. From the experiments, we extract 4 types of data; mixture velocity, instantaneous holdup, pressure gradient, and visual data of the flow field. We define the instantaneous holdup as the volume fraction of liquid within the cross-section. In the case of the experiments, the cross-sectional holdup was determined by using broad beam gamma densitometers (G) at 3 separate locations (Fig. 3). The gamma densitometers acquire holdup data at 50 Hz and function by measuring the average attenuation of the signal. The attenuated signal is then used to calculate the resulting phase fractions within the sampled cross-section, a simple enough procedure given that we know the total distance travelled and the properties of each fluid.

In general terms, the intensity (γ) of an incident beam (γ_o), which has passed through a medium is determined by

$$\gamma = \gamma_o exp(-\mu t), \tag{7}$$

where μ is the linear attenuation coefficient, and t distance traveled. For two-phase flows, the average cross-sectional holdup is calculated by

$$\alpha = \frac{log(\frac{\gamma_m}{\gamma_g})}{log(\frac{\gamma_l}{\gamma_g})}. \tag{8}$$

The calculated liquid holdup (α_l) is thus a ratio of the calibrated single-phase gas and liquid gamma intensities (γ_g, γ_l), as well as the measured gamma intensity (γ_m). The calibrated intensities are determined by single-phase measurements of the gamma beam attenuation, as described by Eq. (7). As the incident gamma beam passes through a fluid, the radiation intensity of the signal is reduced exponentially as a function of distance traveled through the fluid and the attenuation coefficient. The beam attenuation during the two-phase experiments determines the measured gamma intensity.

Table 1
Uncertainty estimates of flow parameters from experiments.

Variable	Uncertainty
ρ_g (kg/m^3)	± 0.5 kg/m^3
ρ_l (kg/m^3)	± 1.5 kg/m^3
u_{sg} (m/s)	± 2.3%
u_{sl} (m/s)	± 1.7%
α_l	± 1.5%
$\Delta P/\Delta L$ (Pa/m)	± 4.5%
σ (N/m)	± 10%

The pressure gradient was measured at 5 separate locations by differential pressure transducers (DP) along the top of the pipe. The DP consist of two pressure measurement devices separated by 3 m with an acquisition rate of 1.2 Hz. By measuring the pressure instantaneously at two locations, the pressure gradient is simply the difference divided by the distance between the measurement devices. The simulations, on the other hand, calculate the required pressure gradient to drive the flow. The calculation is performed as a corrector to the momentum equation and is independent of domain length.

One unfortunate side effect of the low sampling frequency of the experimental pressure gradient is that it does not match the experiment holdup or the simulation data, which both sample at 50 Hz. The low fidelity of the experiment pressure data makes it complicated to compare experiment and simulation with regards to pressure behavior. The obvious solution would be to down-sample the simulation data to match the sampling frequency of the experiments (1.2 Hz). However, for a time-series of 25 s, the simulations would then only have 30 unique data points. The measurement uncertainty of the experiments are summarized in Table 1.

Besides the inherent measurement uncertainty, there are specific physical interactions present in the experimental lab that we do not model in the simulations. Primarily, there are separate inlets for the two phases; a thin plate separates the two inlets, which ensures a smooth stratified initial flow. The second physical inconsistency of the experiments compared to the simulations is that the inner cylinder is kept in place by small spokes. As explained in Nguyen et al. (2019) and Benoit et al. (2018), small flow disturbances such as the spokes, although designed to be non-intrusive, can affect the flow, and even alter the flow regime in some cases.

5. Results

The fluid properties of the liquid and gas phases are consistent across each horizontal case (Tab. 2). However, phase fractions and mixture velocities are altered to induce different flow regimes. The mixture viscosity and density can be determined using Eq. (2). Each concentric experiment has an eccentric counterpart of the same mixture velocity but heightened liquid phase fraction. In order to exemplify the difference that occurs when the holdup fraction is changed, we have simulated all the experiment cases in a partly eccentric domain

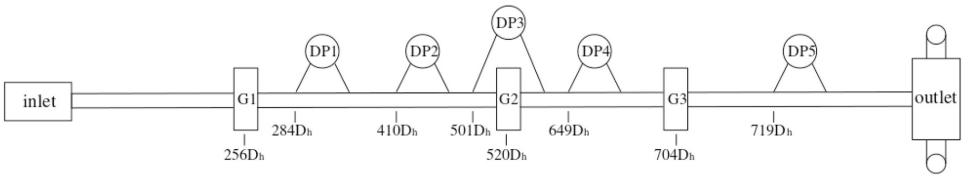

Fig. 3. Schematic of Flow loop, Hydraulic diameter (Dh) = 0.05m, G= Gamma densitometer, DP=Differential pressure transducer, separated inlets for the two phases, with flow straightener in between inlets.

Table 2
Fluid properties of gas (SF_6) and liquid (Exxsol D60) for horizontal annulus experiments and simulations.

Property	Magnitude	unit
ν_l	$1.75{\cdot}10^{-6}$	$\frac{m^2}{s}$
ν_g	$6.2{\cdot}10^{-7}$	$\frac{m^2}{s}$
ρ_l	801.0	$\frac{kg}{m^3}$
ρ_g	24.30	$\frac{kg}{m^3}$
σ	0.0285	N/m

($E = 0.5$). We mention the phase fractions and mixture velocities for each case in their respective sections. We also summarize the fluid properties for the inclined experiment and simulation in the appropriate section.

5.1. Experiment results

The experimental results presented in this section fall under 3 separate categories, horizontal concentric, horizontal eccentric, and inclined eccentric. The concentric and eccentric horizontal experiments are similar, in that they have the same mixture velocities, but different phase fractions and eccentricities. The averaged mixture velocity and fractional holdup data gathered in experiments serve as starting points for the simulations. Furthermore, we compare the experimental pressure gradient and instantaneous cross-sectional holdup with the simulations.

5.1.1. Horizontal concentric annulus experiments

As previously mentioned, the horizontal experimental cases are conducted both in a concentric annulus and fully eccentric annulus, with the same mixture velocities. We summarize the mixture velocities and phase fractions for the concentric cases in Table 3[1]. As reported by Ibarra et al. (2019), the absolute measurement uncertainty for this particular experimental setup is ± 1.5%. Note that the latter two cases employ a significantly higher mixture velocity than the first two cases.

As shown in Fig. 4, there are two cases with low pressure gradient and two cases with high pressure gradient. The cases with low pressure gradients are intuitively believed to be wavy flow cases (possibly with a single slug in case 1), while the high pressure gradient cases are likely to experience slugs. The highly fluctuating behavior displayed in cases 3 and 4 are indicative of slug flow; however, in order to ascertain the flow regime, the pressure data is supplemented with cross-sectional holdup data. The entire data set for the pressure gradient readings consists of 100 seconds and 120 independent measurements. Table 4 presents a summary of the concentric horizontal annulus pressure gradient data.

In Table 4, we have separated the data into three columns corresponding to the 5 and 95% thresholds as well as the mean value. The 5 and 95% thresholds indicate the pressure gradients, where 5% of the data is either below or above the respective threshold. These serve as an estimator for the minimum and maximum values of the pressure gradient. We use the thresholds in place of global maximum and minimum values to alleviate the likelihood of including an extreme outlier. In combination with the pressure data, the holdup data (Fig. 5) is analyzed to determine the flow regime of each case.

We accompany the experiment cases shown in Fig. 5 by three horizontal lines, each of which represents a meaningful metric. The central line is the overall mean holdup, while the upper and lower lines represent the fractional holdup determined as the threshold for a likely slug and likely bubble for the slug cases. The slug indicators are constructed by following the slug identification procedure utilized in Nuland (1999). The method builds upon first determining the mean holdup; we then classify the data as above or below the mean. The data above the mean functions to determine a threshold for a slug. The data below the mean is used to determine a bubble threshold, which

Table 3
mixture velocity and liquid holdup fractions for horizontal concentric experiment cases.

Case #	$\bar{u}$ (m/s)	α (%)
1	1.20	44.75
2	2.70	23.19
3	4.20	38.56
4	4.10	46.62

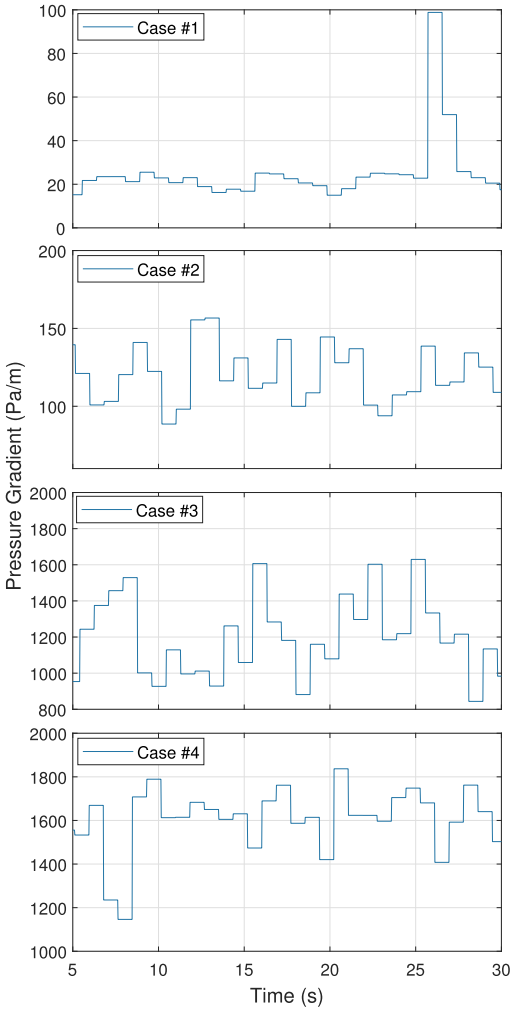

Fig. 4. Pressure gradient as a function of time for horizontal concentric experiment cases.

[1] Case # 1,2,3 and 4 correspond to experiment # 3051, 3054, 3102 and 3117 in the IFE experiment database.

Table 4
Pressure gradient summary, horizontal concentric experiment cases with mean, low (5%) and high (95%) threshold values.

Case #	5% (Pa/m)	mean (Pa/m)	95% (Pa/m)
1	16.80	31.56	67.92
2	84.59	118.22	149.28
3	782.62	1196.49	1624.38
4	1179.12	1560.04	1789.92

separates slugs, in order for the indicator to identify a new slug, the profile must have transitioned through the bubble-slug-bubble criterion. The horizontal lines help illustrate the larger intermittent waves for the wavy flow cases.

There are indications that the large waves seen in case #1 (Fig. 5) arrive in packets, as seen in the period between 15 and 20 s. Case #2, on the other hand, displays more evenly distributed occurrences of large waves, and they appear reasonably periodic in time without any significant discrepancies.

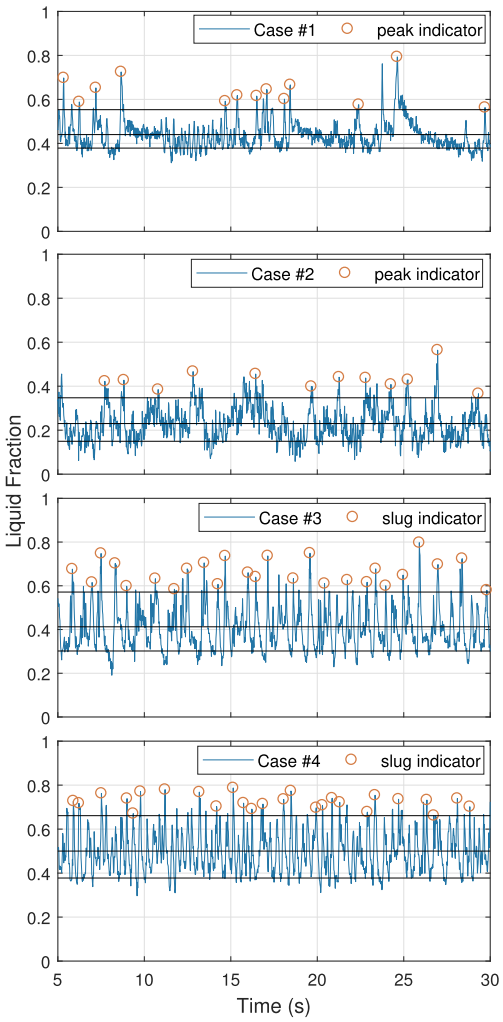

Fig. 5. Liquid holdup fraction as a function of time for horizontal concentric experiment cases, including peak indicators for slugs and waves and thresholds for mean, bubble and slug.

Table 5
Slug and wave frequencies for horizontal concentric annulus experiments (E = 0).

Case #	Slug frequency (Hz)	Wave frequency (Hz)
1	-	0.47
2	-	0.52
3	1.06	-
4	1.09	-

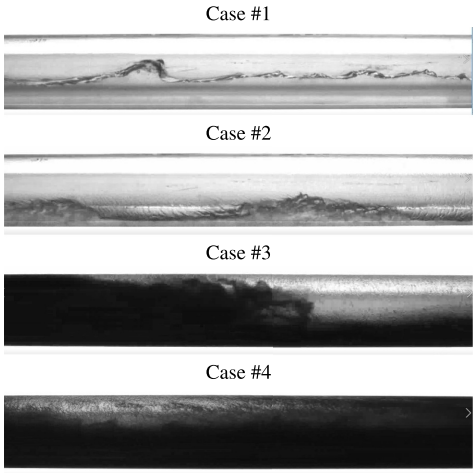

Fig. 6. Snapshots of flow regime for horizontal concentric annulus experiments (E = 0).

The holdup data indicate that the flow regime of the two low velocity cases (1 & 2) are consistent with high frequency waves. Case 2 behaves more regular in terms of the wave amplitude as the liquid holdup varies between 0.15 and 0.4. Case 1 consists of high frequency small waves, with a few intermittent large waves, while cases 3 and 4 experience slugs, with a slug frequency of 1.06 - 1.09 Hz. Note that the slug and wave frequencies summarized in Table 5 are extracted from the entire 100 s time series, while we show only 25 s for illustration purposes.

Alongside the fractional holdup data, the experiments also utilized various cameras located along the test section. The location of one of these image-capturing stations was 35 m downstream of the inlet. The visual data at this test section corroborates the flow regimes identified from the holdup data, as shown in Fig. 6.

We represent each case with a snapshot of the observed flow regime (Fig. 6). The snapshot for experiment case 1 shows several small waves followed by a larger breaking wave. The image for case 2 shows two relatively large waves following each other, while cases 3 and 4 both represent slug flow. Although the liquids appear visually different in each snapshot, the fluids present are the same hydrocarbons in each case. Small bubbles of gas permeating through the liquid layer cause the observed darkening effect of the liquid, the effect is worsened in the two slug flow cases.

5.1.2. Horizontal eccentric annulus experiments with E = 1.0

The important flow properties which we extract from the experimental data and utilize as initialization values for the related simulations (Sim. cases 5–8) are summarized in Table 6.

Table 6
Mixture velocities and liquid holdup fraction for horizontal eccentric annulus experiment cases (E = 1.0).

Case #	$\bar{u}$ (m/s)	α %
5	1.20	62.54
6	2.70	47.58
7	4.20	44.95
8	4.10	53.49

The horizontal eccentric annulus experiments[2] are similar to their concentric counterparts. The mixture velocities are consistent with the concentric annulus cases. However, they differ in that the liquid phase fractions are higher than their concentric counterparts; also, the inner cylinder is fixed against the bottom of the outer cylinder ($E = 1.0$).

At first glance, the eccentric (Fig. 4) and concentric (Fig. 7) pressure gradient measurements appear to be similar. Cases 1 and 5 are both at 1.2 m/s mixture velocity, and display similar pressure gradient trends, with a low overall pressure gradient accompanied by sudden spikes. The pressure gradient spikes are several times higher than the normal behavior and are likely an effect of large waves.

Case #6, which corresponds to case #2, also appears to behave similarly concerning the pressure gradient. There is a slightly higher average pressure gradient in the case of the concentric experiment; however, the amplitudes of the individual pressure spikes are similar.

There are no discernible changes in the measured pressure gradients between the eccentric and concentric experiments that would indicate a significant difference in the flow regime between cases of the same mixture velocity. Cases 5 and 6 appear to behave as wavy flow, while cases 7 and 8 are reminiscent of slug flow, as seen by the highly fluctuating pressure behavior. The slug flow cases display pressure spikes of several hundred Pa/m in the span of a single timestep. These observations follow the trends observed for the corresponding concentric experiments (Fig. 4). The only noticeable difference is that there appears to have been a pressure gradient decrease between the concentric cases 2, 3, and 4 and the eccentric cases 6, 7, and 8. Tables 7 and 4 present an overview of the pressure gradient data for the horizontal eccentric annulus experiment cases.

Relative to their concentric counterparts (Fig. 4), the eccentric cases 6, 7, and 8 (Fig. 7) have undergone a 20% reduction to the mean pressure gradient. Compared to a concentric annulus, a fully eccentric configuration has a reduced friction factor through a combination of factors, one of which is the narrow gap separating the cylinders. The reduction of the friction factor makes the pressure gradient drop a predictable outcome. Interestingly, case 5 is an exception. As noted, there is a phase fraction difference between the eccentric and concentric experiments. The liquid phase fraction increase offers a possible reason for why case 5 is the only case without a reduced mean pressure gradient as there is significantly more liquid in case 5 compared to case 1. In subsequent simulations, we will notice that for every case, an increase in holdup fraction equates to an increased mean pressure gradient.

The threshold values for the respective cases also undergo similar reductions. The consistency of pressure gradient behavior is an indicator but does not confirm that the concentric and eccentric cases are consistent with regards to the flow regime. For confirmation, we have to delve into the holdup data and account for any potential differences.

As shown in Fig. 8, cases 5 and 6 are fundamentally different to 7 and 8. The two prior cases indicate wavy flow with large intermittent waves. These observations are consistent with the low pressure variations shown in Fig. 7. For the low velocity flow cases, the increase in average liquid holdup between the concentric and eccentric cases

[2] Case # 5,6,7 and 8 correspond to experiment # 6005, 6008, 6089 and 6106 in the IFE experiment database.

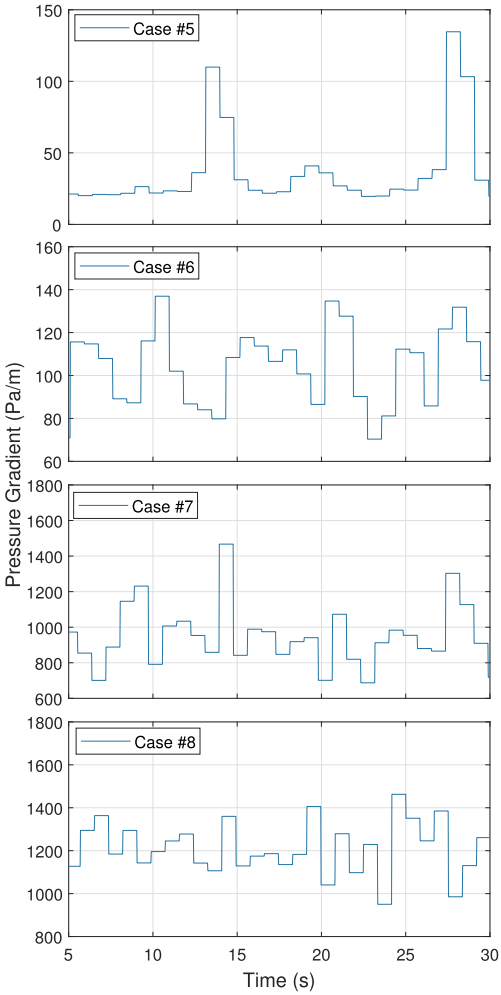

Fig. 7. Pressure gradient as a function of time for horizontal eccentric annulus experiment cases (E = 1.0).

combined with the changed eccentricity results in larger waves. Especially case #5 (Fig. 8) has less extended periods of ripple waves and more large waves when compared to case #1 (Fig. 5).

Cases 2 and 6 appear similar with no significant change in the holdup pattern, although the large waves are of a higher amplitude. The two slug cases remain sluggish but at an increased frequency (Tables 8 & 5). For the experiments, changing the eccentricity and phase fractions while maintaining the same mixture velocity, appear to have had little

Table 7
Pressure gradient summary for horizontal eccentric annulus experiment cases (E = 1.0) with mean, low(5%) and high (95%) threshold values.

Case #	5% (Pa/m)	mean (Pa/m)	95% (Pa/m)
5	15.29	36.27	98.20
6	74.90	102.95	136.95
7	696.43	961.00	1332.89
8	1031.45	1207.22	1405.03

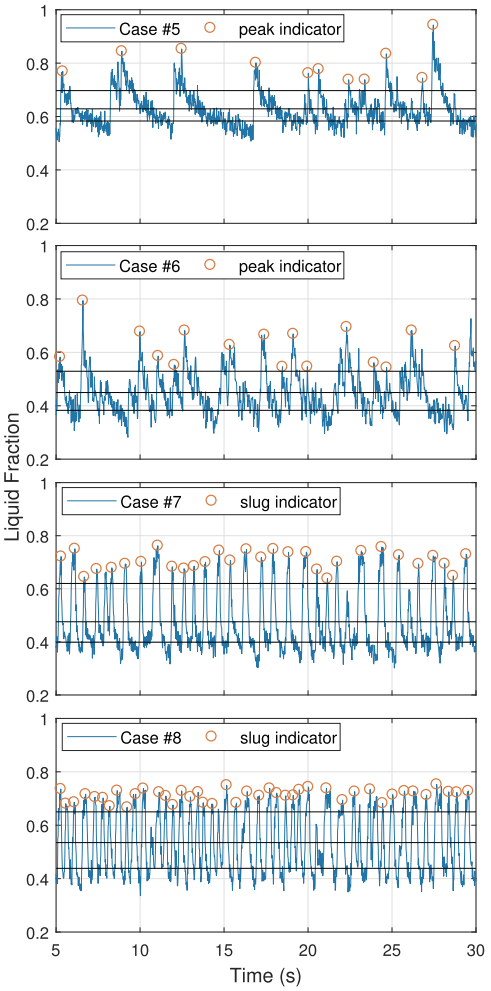

Fig. 8. Liquid holdup as a function of time for horizontal eccentric annulus experiment cases (E = 1.0), including peak indicators for slugs and waves, and thresholds for mean, bubble and slug.

Table 8
Wave and slug frequencies for horizontal eccentric experiment cases (E = 1.0).

Case #	Slug frequency (Hz)	Wave frequency (Hz)
5	-	0.44
6	-	0.64
7	1.16	-
8	1.64	-

impact on the resulting flow regime, apart from increasing the slug frequency and wave amplitude.

The typically observed flow regimes (Fig. 9) of the entirely eccentric experimental cases are similar to the concentric experimental cases (Fig. 6). Although each case has a higher average liquid holdup, the flow regimes are consistent. Case # 5 is perhaps the one exception. The average liquid level means the interface between liquid and gas coincides with the top of the inner pipe. The result is that there are shorter

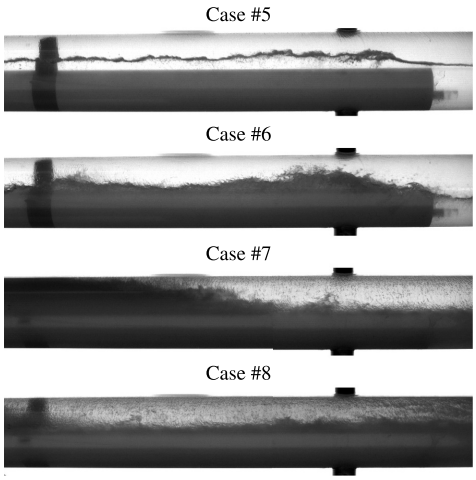

Fig. 9. Snapshots of flow regime for horizontal eccentric annulus (E = 1.0).

periods with ripple waves interrupted by large intermittent waves. Both of these wave types are discernible from the holdup data (Fig. 8); the high amplitude waves are marked by indicators, while the smaller waves are the erratic region following the large waves.

The two slug flow cases visually behave the same as the concentric cases; however, with an increased slug frequency. While both the concentric cases had a slug frequency of 1.06-1.09 Hz, cases 7 and 8 have slug frequencies of 1.16 and 1.64 Hz, respectively. The observation is interesting and could be an effect of either the increased average holdup or comparing two cases with different eccentricity. Because the simulations all share the same eccentricity, we can use the simulations to ascertain if the eccentricity is contributing to the difference in slug frequency or if it is an effect of the increased holdup between cases 1–4 and 5–8.

5.1.3. 4 Degree inclined eccentric annulus experiment

The 4° inclined experiments[3] were performed in a completely eccentric configuration (E = 1.0), in a similar but shorter flow loop compared to the previously presented experiments (Fig. 3). The fluid properties are slightly different than for the horizontal configuration (Tab. 2) as summarized in Tab. 9.

The primary differences between the inclined flow experiments and the horizontal ones are that the liquid mixture containing Exxsol D60 and Marcol 82 is significantly more viscous than the pure Exxsol D60 utilized in the horizontal experiments. The inner pipe also had a smaller diameter of 40 mm compared to 50 mm for the horizontal cases. Both fluids used in the inclined experiment are also denser than their horizontal experiment counterparts; the reason for the higher gas density is a higher system pressure in the inclined experiment.

The inclined experiment time series lasts for 120 s; however, we show 25 s for illustration purposes (Fig. 10), while we analyze the entire 120 s for the statistical behavior of the flow. The pressure gradient behavior is reminiscent of large waves or potentially slug flow. Typically, a slug flow at this mixture velocity will have a higher average pressure gradient; however, a low frequency slug flow could potentially behave as shown. The relative difference from the mean to maximum and minimum thresholds are roughly 35 - 45% as summarized in Table 10.

The histogram presents a visual representation of the pressure

[3] Case # 9 correspond to experiment # 7049 in the IFE experiment database.

Table 9
Fluid properties of gas (SF_6) and liquid (Exxsol D60/Marcol 82) for inclined eccentric experiment (E = 1.0).

Property	Magnitude	Unit
ν_l	$2.6 \cdot 10^{-5}$	$\frac{m^2}{s}$
ν_g	$3.42 \cdot 10^{-7}$	$\frac{m^2}{s}$
ρ_l	854.60	$\frac{kg}{m^3}$
ρ_g	43.83	$\frac{kg}{m^3}$
σ	0.0285	N/m

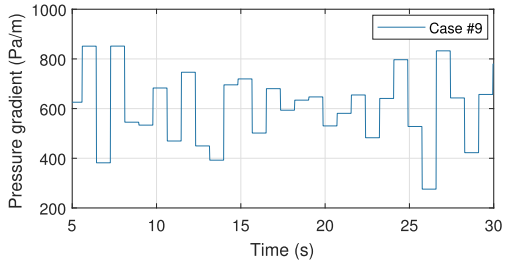

Fig. 10. Pressure gradient as a function of time for inclined eccentric experiment (E = 1.0).

Table 10
Pressure gradient summary for 4 ° inclined eccentric experiment (E = 1.0) including mean, low (5%) and high (95%) thresholds.

Case #	5% (Pa/m)	Mean (Pa/m)	95% (Pa/m)
9	385.11	601.66	877.98

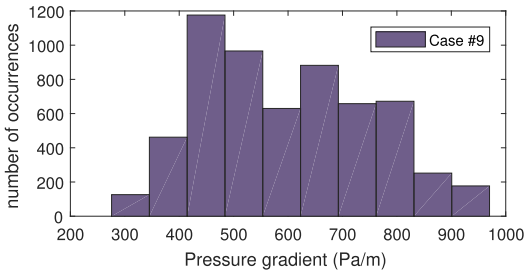

Fig. 11. Pressure gradient histogram for inclined eccentric experiment (E = 1.0).

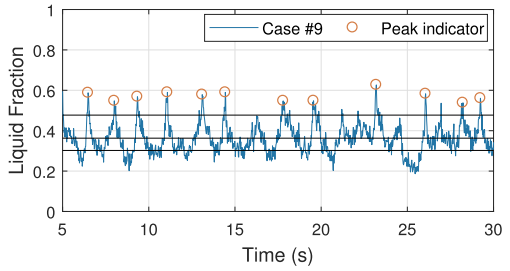

Fig. 12. Holdup as a function of time for inclined eccentric experiment with E = 1.0, including peak indicators for waves.

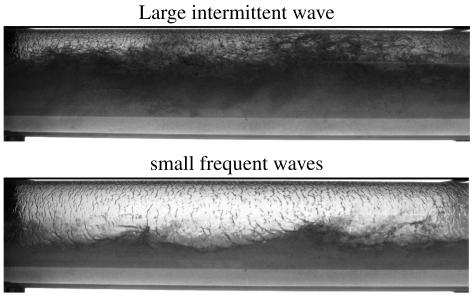

Fig. 13. Snapshots of flow regime for 4° inclined eccentric experiment case # 9 (E = 1.0).

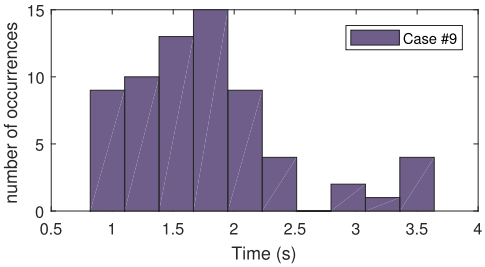

Fig. 14. Large wave event interval, inclined eccentric experiment case # 9 (E = 1.0).

gradient behavior. As shown in Fig. 11, there are rare occurrences of pressure gradient spikes and troughs at near 1000 and 300 Pa/m. The shape is reminiscent of a Gaussian distribution. However, the left tail abruptly stops while the right tail extends; this is known as a right-skewed distribution.

The peak holdup readings seen in Fig. 12 indicate that this is either a significantly aerated slug flow or more likely intermittent large waves. In order to verify the flow regime, we cross-reference with the visual data (Fig. 13) captured at the second camera location (Fig. 3).

The visual data suggests that the peaks indicated in Fig. 12 are thoroughly aerated liquid waves. Between large liquid waves, there is a period of smaller high frequency waves.

Note that the band seen at the bottom of each image is not a gap between the inner and outer cylinder but rather an optical disturbance, in fact, the band is visible near the middle of the images for the horizontal cases (Figs. 6 & 9). There are several problems when taking images of a see-through pipe filled with two fluids. The most likely cause for the bright band is that refraction has caused an optical distortion, which makes it appear that the inner pipe is not touching the outer pipe.

If we analyze the entire time-series of which 25 s is shown in Fig. 12 and determine the period between each peak, we can say something about the wave frequency and frequency distribution. In this case, we have converted the data into a histogram (Fig. 14). We notice that the majority of the periods between large waves are in the region from 1 to 2 seconds, the average frequency of large waves is 0.5667 Hz or a wave period of 1.76 s.

5.2. Simulation results

Following the previously established convention, we separate the simulation results into three categories, corresponding to the experiment sections. The categories are horizontal eccentric cases 1–4, horizontal eccentric cases 5–8, and inclined eccentric. The horizontal cases

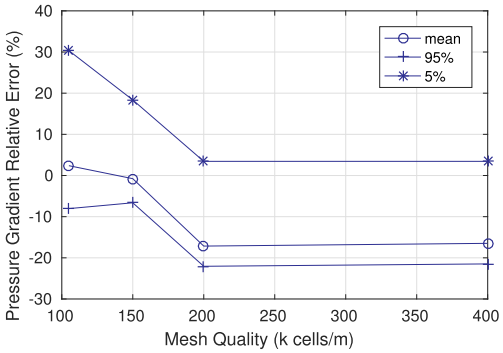

Fig. 15. Relative error of pressure gradient as a function of mesh count for u_{mix} = 3.6 m/s and α = 0.53. Adapted from Friedemann et al. (2019).

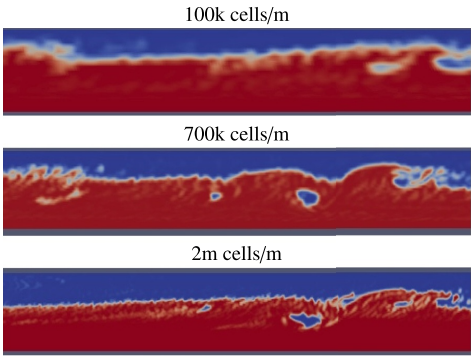

Fig. 16. Effect of mesh density on phase-mixing, bubble formation and interface sharpness.

are split into two sets corresponding to the experiments they are based on. The first 4 are based off of concentric experiments, while cases 5–8 are based off of fully eccentric experiments. Within each category, we sort the data by holdup and pressure gradient results. As was the case in the experiment section, we will start with cases 1–4. These simulations use the phase fractions and average mixture velocities extracted from the experimental data. However, as mentioned, the simulations are run in a domain with an eccentricity of 0.5, which means we do not expect the simulations to behave as replications of the experiments. The eccentricity difference allows us to analyze whether it has a significant impact on the flow regime and pressure gradient behavior.

Based on previous work (Friedemann et al., 2019), the 7 m domain is the chosen domain length for the simulations. Although the work showed that shorter domains could be reasonable approximations of experiments, an extended domain minimizes the risk of inadvertently altering the flow by restricting the amount of available liquid within the domain. This effect is more pronounced in strong periodic flows such as slugs or plugs, while wavy flow should be less prone to flow regime deviations caused by domain deficiencies.

Although the 7 m domain was overall the best representation of both slug frequencies and pressure gradient based on previous simulations, there is an additional computational cost related to a longer domain. To compensate for the prohibitive computational cost, we run the simulations at a lower mesh density than ideally desired. Keep in mind that the previous work indicated that the flow regime is not affected by the mesh density in the range of meshes studied. The pressure gradient is affected to some degree; however, they were shown to be reasonable approximations of the expected result in concentric horizontal configurations. The common trend was that the pressure gradients would be overestimated at low mesh resolution and underestimated at high mesh counts, while flow regime and slug frequencies remained consistent throughout meshes. The effect of mesh count on the pressure gradient and interface is illustrated in Figs. 15 & 16

Though neither of these cases is an exact representation of the current research, the expectancy is that the mesh effect is representative of current behavior. The pressure gradient relative error data (Fig. 15) was collected for a slug flow with an mixture velocity of 3.6 m/s and α = 0.53. It should be reasonably representative of the higher velocity cases studied in this paper. Although, the current study includes an intended discrepancy with regards to the pressure gradient due to the different eccentricity of the simulations compared to the experiments.

The mesh's effect on the interface is clearly illustrated through Fig. 16, the images are captured at the same location and time, and through them, we can identify an increased phase-mixing from increasing the mesh density and also an increase in ripple waves present on the interface between the two phases. As shown, the coarsest mesh does a sufficient job at capturing the large scale movements; however, the finer details like gas entrainment and submerged large bubbles are smeared out or removed. The preservation of the large-scale structures corroborates previous findings that the frequency of proto-slug and large waves is maintained even at coarse meshes. In contrast, information about gas entrainment and bubble formation is lost.

5.2.1. Horizontal simulation cases 1–4 with eccentricity of 0.5

Fig. 17 displays pressure as a function of time for the 4 horizontal cases. The wavy flow cases (1 & 2) display a nearly constant pressure gradient state compared to the experiments. We believe this is a side effect of the periodic boundary conditions combined with the low velocity flow. The two slug cases (3 & 4) behave as expected; the periodic build-up and dissipation of slugs result in a violent pressure reaction, varying with several hundred Pa/m within seconds.

The histograms (Fig. 18) represent a statistical overview of the pressure gradient behavior for simulation cases 1–4. They show that the slug pressure drop distributions are relatively concentrated. The wavy cases are slightly different, and there are indications that case # 1 is perhaps not fully developed yet, as the pressure drop seems to be increasing until it drops at the very end. This observation is at odds with previous simulations, which have indicated that after 5 s the flow is developed and in a periodic state.

Table 11 summarizes the pressure gradient information from simulation cases 1 to 4. We notice that the mean pressure gradients from the simulations are a surprisingly good match to the experimental data, to within 10% for the three latter cases. We emphasize that these simulations are not supposed to be an exact match to the experiments as the inner cylinder location does not match the experiment location. Instead, they are meant to highlight changes to the flow behavior that may occur due to the eccentricity difference.

We notice that for case 1, there is a quite significant mean pressure gradient change. For this particular case, the experiment has an unbroken liquid surface below the concentric pipe when there are no waves, while for the eccentric simulation, the interface between fluid and gas occurs in the presence of the interior pipe. The different eccentricities mean the interfacial area between liquid and gas is more significant in the experiments, while the interface between the cylinder wall and liquid is higher in the simulations, which in turn alters the frictional forces as well as the transfer of energy between phases.

We have previously worked on similar cases at similar mesh densities and established that the simulations tend to underestimate the maximum pressure gradient by roughly 10% and overestimate the minimum and mean pressure gradients by 23.7% and 2.3% respectively at 100k cells/m. If we similarly determine the relative error compared to the experiments, we see a major difference between the concentric

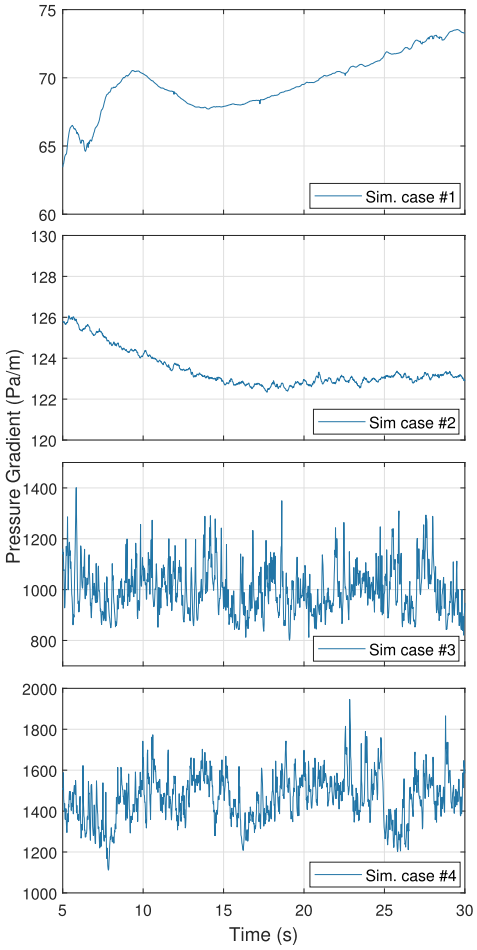

Fig. 17. Simulated pressure gradient as a function of time for horizontal eccentric annulus with E = 0.5 and 100k cells/m.

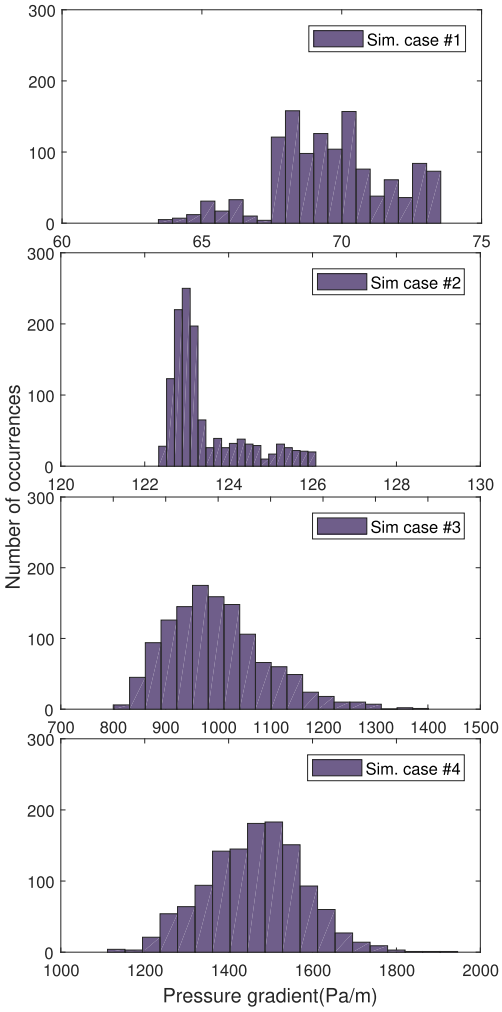

Fig. 18. Histogram of simulated pressure gradient for horizontal eccentric annulus with E = 0.5 and 100k cells/m.

experiments and partly eccentric simulations for case 1, as shown in Table 12.

The deviations compared to the experiments are as high as 291% for case 1. These behavioral changes could occur due to the narrow gap below the inner cylinder. Alternatively, the cause is the altered location of the interface between fluids and the inner pipe. Considering that the largest differences occur in the wavy flow cases, it is also possible that the computation of the pressure gradient for wavy flow is extremely dependent on both holdup rates and wave type. As shown in Figs. 21 and 5 the wave behavior is significantly different in the simulated case with E = 0.5 compared to the experiment with E = 0.0. We believe the different flow behavior is responsible for the majority of the pressure gradient shift. There is also some small error involved in the measurement of mean holdup in the experiments, the discrepancy between actual experiment holdup and simulation holdup could contribute to the computed relative difference.

The remaining cases are in better agreement, yet the errors are still as high as 45% for case 2, and below 30% for the two slug cases. We notice that for the slug cases, the general trend is that the difference between simulation and experiment is shifted negatively compared to the previous work. The negative shift coincides with the idea that the pressure gradient should decrease in a more eccentric configuration.

As we refine the mesh (Fig. 19), we notice that there are some slight differences to the pressure gradient behavior (Table 13).

Both the low velocity cases (1 & 2) agree with the behavior seen in the coarser mesh in terms of the relatively constant pressure gradient, although slightly decreased for simulation case 1. Also, there is a slight change in the overall behavior of the first case. Instead of the weakly increasing pressure gradient shown for the coarser mesh (Fig. 17, case 1), the pressure gradient flattens out at 65 Pa/m after a period of slowly increasing and decreasing over time.

Case 2 displays the same type of behavior in both meshes, while the two slug cases are at a slightly lower overall pressure gradient. The trend that the pressure gradient decreases with increased mesh density was also noted in Friedemann et al. (2019) for slug cases. We believe that this occurs due to an inability to resolve minor bubbles and finer flow structures. It is well known that an inability to resolve the minor

Table 11
Pressure gradient summary for horizontal eccentric annulus with E = 0.5 and 100k cells/m, with mean, low (5%) and high (95%) threshold values.

Sim #	5% (Pa/m)	mean (Pa/m)	95% (Pa/m)
1	65.69	69.61	73.08
2	122.60	123.45	125.51
3	863.89	998.68	1168.83
4	1270.03	1464.04	1648.63

Table 12
Relative difference of horizontal eccentric simulations (E = 0.5 and 100k cells/m) compared to concentric experiments (E = 0.0).

Sim #	5% (%)	mean (%)	95% (%)
1	291.0	120.5	7.6
2	44.93	4.4	−15.92
3	10.4	−16.53	−28.05
4	7.71	−6.2	−7.89

structures will alter the turbulent field through the energy cascade. Thereby also how turbulence is treated at the fluid interface and wall regions. The effective viscosity is also affected through a lack of mixing. Additionally, the difference in wave amplitude observed for the two case #2 meshes (Figs. 21 and 22) likely contributes to why the finer mesh does not show a reduced mean pressure gradient.

Comparing the histograms, Fig. 18 and 20, and Tables 11 and 13, for the two meshes, there is one noticeable trend; as we increase the mesh density, the computed pressure gradients decrease. While the minimum values are near the experiment results, the mean and maximum pressure gradient estimator is considerably off for the slug flow cases. The reason the minimum results are reasonable is likely a combination of effects and hard to identify. There are several probable contributors; the overall level of turbulence in the calmer state, the transference of turbulent energy at the interface, and the dampening at the wall. In combination with these effects, during the calmer flow state, there are fewer bubbles present in the experimental measurements, which is more representative of the behavior of the simulations. Conversely, the inability to resolve minor bubbles results in large bubbles forming near the top of the slugs, reducing the required pressure gradient to drive the flow, which affects the peak values of the simulations.

Previous work (Friedemann et al., 2019) indicates an error estimate of roughly 21 and 28% undershoot of the mean and maximum pressure gradient at this mesh density, as well as an expected overshoot of the minimum pressure gradient of 3.4% at 200k cells/m.

Comparing the corresponding relative differences for the 100 and 200k cells/m meshes (Tables 12 and 14), we notice a persistent negative shift for all cases apart from Sim. 2. We attribute the discrepancy to the altered flow pattern of that particular case, as shown in Figs. 21 and 22. The presence of larger waves coincides with an increase of turbulent kinetic energy and, thereby, an increased pressure gradient. The two slug cases behave relatively similar to the experiments; however, consistently undershoots the experiment pressure gradient. The behavior is expected as the friction factor is lower in any eccentric configuration compared to a concentric configuration.

Concerning the holdup profile for the coarsest mesh (Fig. 21) compared to the experiment data (Fig. 5), there is one significant difference. Namely, case 1 has a complete lack of minor waves or ripple waves. We believe numerous aspects could cause the effect. One of which is a poor choice of initial conditions, which could induce a near steady-state flow regime that is not the expected physical result. Conversely, the low velocity cases, in particular case 1, takes a significant time to develop; by this logic, the simulation could yet be developing. Another possible cause is that the different eccentricity results in large waves with less small wave effects. Interestingly, there are indications

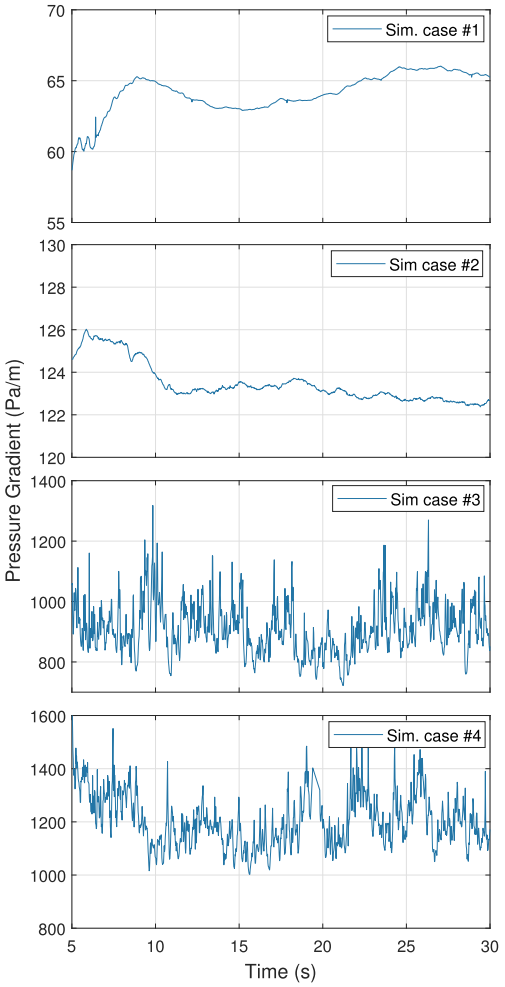

Fig. 19. Simulated pressure gradient as a function of time for horizontal eccentric annulus with E = 0.5 and 200k cells/m.

Table 13
Pressure gradient summary for horizontal eccentric annulus with E = 0.5 and 200k cells/m, with mean, low (5%) and high (95%) threshold values.

Sim #	5% (Pa/m)	mean (Pa/m)	95% (Pa/m)
1	60.91	64.15	65.87
2	122.54	123.47	125.53
3	785.07	909.25	1064.34
4	1063.04	1203.92	1383.30

that the wavy flow eccentric experiment cases (Fig. 8) are showing this type of behavior, as shown by the more prominent large waves with the gradual drop off of holdup in between large waves.

The other cases are more consistent with their experimental counterparts. Case 2 is exhibiting more uniform waves than that seen in the experiments and also at a significantly higher frequency after 15 s (2.2 Hz). The increased frequency is thought to be caused by the intentional difference between simulation and experimental setup with regards to the eccentricity for these cases. The slug flow cases 3 and 4

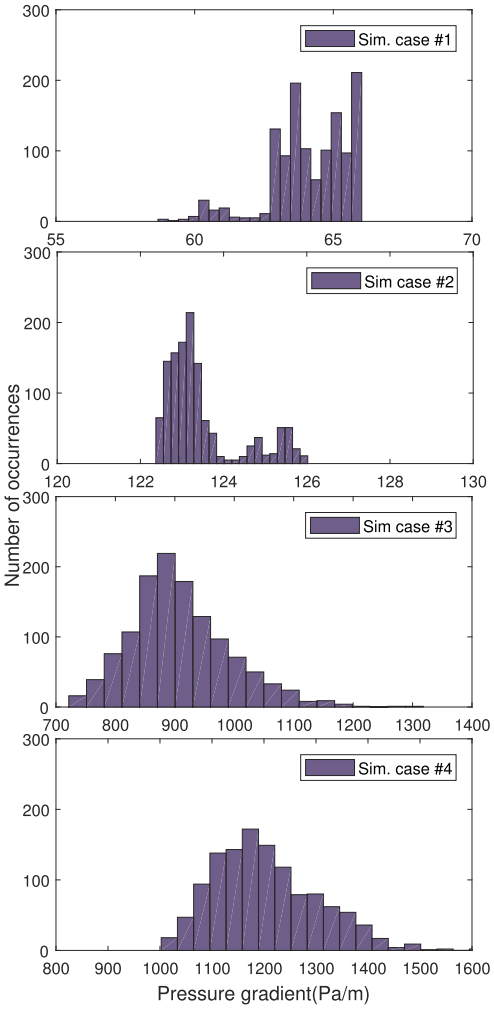

Fig. 20. Histogram of simulated pressure gradient summary for horizontal eccentric annulus with E = 0.5 and 200k cells/m.

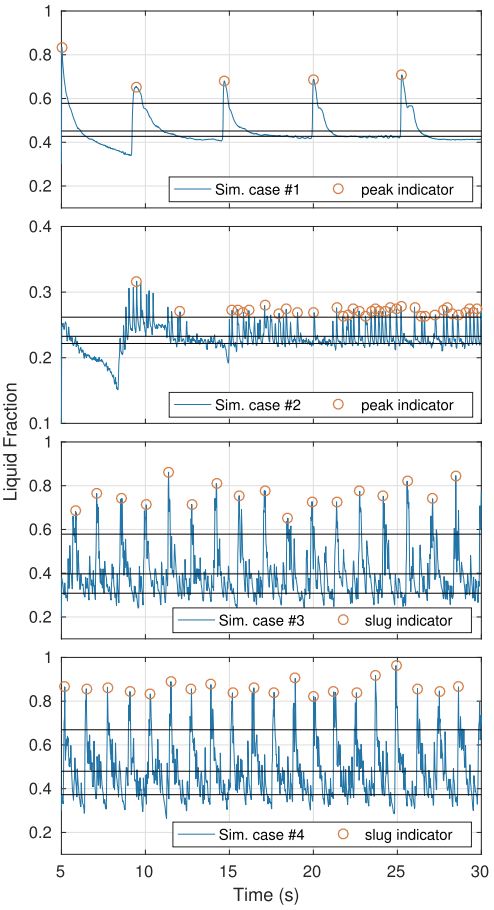

Fig. 21. Liquid holdup fraction as a function of time for horizontal eccentric annulus (E = 0.5 and 100k cells/m). Peak indicators for proto-slugs and waves as circles and horizontal lines for mean holdup and bubble and slug threshold values.

are also represented as proto-slug flow by the simulations at a reduced slug frequency of 0.68 and 0.8 Hz compared to 1.06 and 1.09 Hz.

Compared to the concentric experiments, we have noticed both a change in the wave pattern for cases 1 and 2 as well as slug frequency (cases 3 & 4). Accompanying these holdup pattern changes, we observe, in some cases, drastic pressure gradient changes, which to us indicates that altering the eccentricity from E = 0 to E = 0.5 has had an immediate effect on the resultant flow.

The simulations for the increased mesh density (Fig. 22) show one noticeable difference compared to the lower density simulations (Fig. 21). The waves produced in the second simulation case are significantly larger. The wave structures have an amplitude of $\tilde{5}\%$ liquid holdup, while for the coarser mesh, they are nearer to $\tilde{2.5}\%$.

Concerning the comparison between experiments and simulations, we again observe that simulation case 2 maintains an increased wave frequency. If we exclude the initial 15 s where there appears to be some transient behavior, the wave frequency is 2.47 Hz. The frequency is similar to the 100k cells/m simulation (2.2 Hz), but a significantly increased deviation compared to the experiment (0.64 Hz). Both mesh densities indicate that the eccentricity of the annulus has had a significant impact on the flow regime of this case. While not transitioning to a different flow regime, the wave behavior, amplitude, and frequency have changed.

For the 3 remaining cases, the finer mesh remains consistent with the 100k cells/m simulation with regards to the holdup pattern. The wave frequency and amplitude remain similar (case 1) while we note a small increase in the slug frequency from 0.68 and 0.78 Hz to 0.72 and 0.96 for case 3 and 4, respectively.

When we compare the snapshots of the eccentric simulation cases 1 to 4 (Fig. 23) with their corresponding experiment images (Fig. 6), the most immediate observation is the altered flow state of simulation case 1 compared to the experiment. We do not observe the long rolling

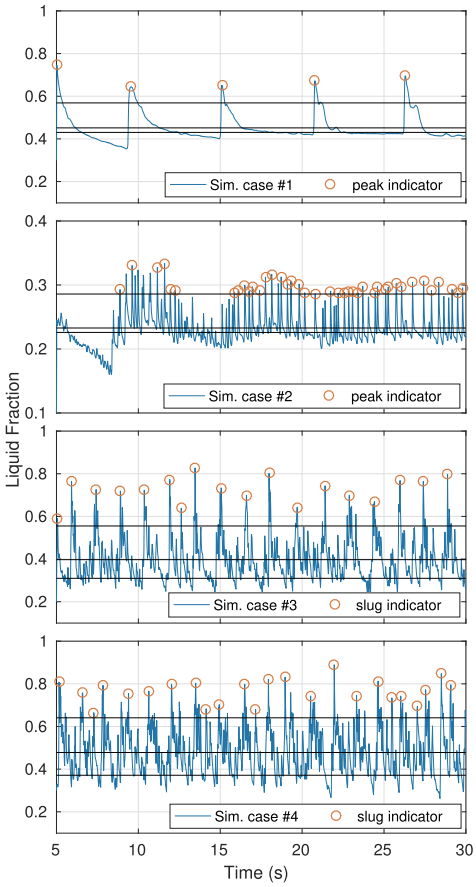

Fig. 22. Liquid holdup as a function of time for horizontal eccentric annulus (E = 0.5 and 200k cells/m). Peak indicators for proto-slugs and waves as circles and horizontal lines representing mean holdup and bubble and slug threshold values.

Table 14
Relative difference of horizontal eccentric simulations (E = 0.5 and 200k cells/m) compared to concentric experiments (E = 0.0).

Sim #	5% (%)	mean (%)	95% (%)
1	262.6	103.3	−3.0
2	44.9	4.4	−15.9
3	0.3	−24.0	−34.5
4	−9.8	−22.8	−22.7

waves observed in the experiments. The long waves observed in the experiments are usually both preceded and followed by a region of smaller waves reminiscent of ripples. The reason there are no ripple waves in the simulation is likely two-fold. A combination of the initial conditions and the mesh density can produce unexpected flow patterns. In the case of ripple waves, if the mesh is not able to resolve them, the complete removal is a possible outcome. For the remaining cases, the observations are more subtle and better observed by the holdup fractions.

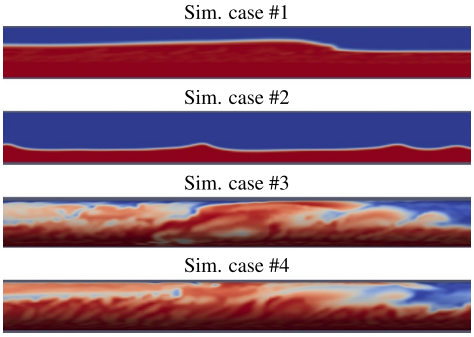

Fig. 23. Snapshots of flow regime with liquid phase in red and gas phase in blue, horizontal eccentric annulus with E = 0.5 and 200k cells/m. Snapshots for cases 1 and 2 are interior, while Cases 3 and 4 snapshots are exterior images. (For interpretation of the references to colour in this figure legend, the reader is referred to the web version of this article.)

5.2.2. Horizontal simulation cases 5–8 with E = 0.5

Simulation cases 5 to 8 (Fig. 24) were only run in the 100k cells/m mesh, as the flow regime shows a limited change between meshes for cases 1 to 4. Additionally, the pressure results are of comparable values.

The pressure gradient solutions for cases 5 and 6 drastically overshoot the experimental results. However, the tendency is less surprising when we also account for the change in the central pipe location from E = 1.0 to E = 0.5. In short, this particular eccentricity change should result in a pressure gradient increase due to the increase in friction factor caused by the development of flow within the narrow gap of the annulus. The narrow gap reduces the velocity of the flow within the region, as shown in Fig. 25; however, it is still significantly faster than for E = 1.0, which contributes to an increased pressure gradient.

The velocity field within the gap is somewhat stagnant compared to the free-flowing liquid within the central region of the annulus. The combination of the stagnant region and the pressure gradient computation method results in an increased pressure gradient when compared to a case with E = 1.0. This effect occurs because the slowed down region is a significant contributor to the averaged field, which is accounted for when the simulation determines the pressure gradient required to maintain the mixture velocity. Physically speaking, there is also an increased friction factor at E = 0.5 compared to E = 1.0, as stated by Caetano (1985), the friction factor is always lower in a more eccentric annulus.

The slug cases are closer to the experimental results, although by no means a perfect match. What we can determine through these case presentations is limited with regards to the pressure gradient solutions themselves without also accounting for the flow regime. It is highly likely, however, that the leading cause of the increased pressure gradients is the different eccentricities of the simulated (E = 0.5) and experimental (E = 1.0). In addition to the mentioned stagnant flow, in some cases, the partly eccentric configuration results in a partial submersion of the interior pipe, which significantly alters the flow conditions compared to an entirely submerged inner pipe in a fully eccentric configuration.

However, we can say something about possible reasons why the slug cases are better representations of the pressure solutions than the wave solutions. The slug case pressure distributions (Fig. 26) experience a higher degree of dependency of the slug structures with regards to pressure gradient. As the proto-slugs form, they create a large fluid structure. The slug, which has a higher mixture density and viscosity, requires more force to push through the domain. As such, when there are slugs present, the pressure gradient is dominated by density and turbulent forces compared to the low velocity cases, where perhaps viscosity and laminar friction are prevalent.

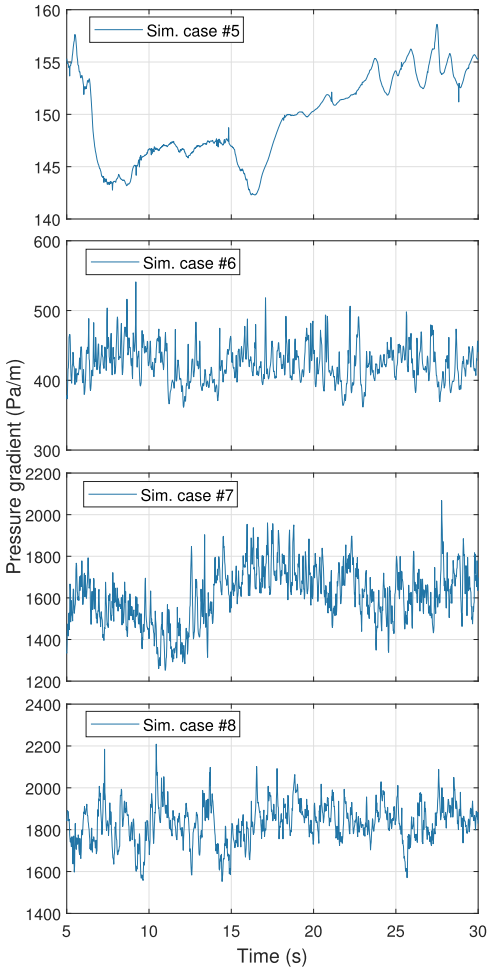

Fig. 24. Simulated pressure gradient as a function of time for horizontal eccentric annulus with E = 0.5 and 100k cells/m.

Comparing the two sets of simulation cases with the same mesh density (Tables 11 and 15), the higher liquid holdup results in a significantly higher pressure gradient for all cases of the same mixture velocity, sometimes dramatically, as shown by the difference in simulation case 2 and 6. Simultaneously, comparing the simulation to the experiments (Tables 15 and 7), the relative differences are quite large. We attribute the majority of the change to two aspects, the coarse mesh and the gap left between the inner and outer cylinder, which increases the friction factor. However, even if we account for mesh associated errors, the pressure gradients are drastically higher than for the fully eccentric experiments.

As shown in Tables 16 and 12, the differences are higher when we compare with experimental data at E = 1.0, which we expected. We believe the cause of the substantial differences in Sim. 5 is a persistent slug formed at startup, as seen in Fig. 27.

Similarly to simulations compared with E = 0, the slug cases perform

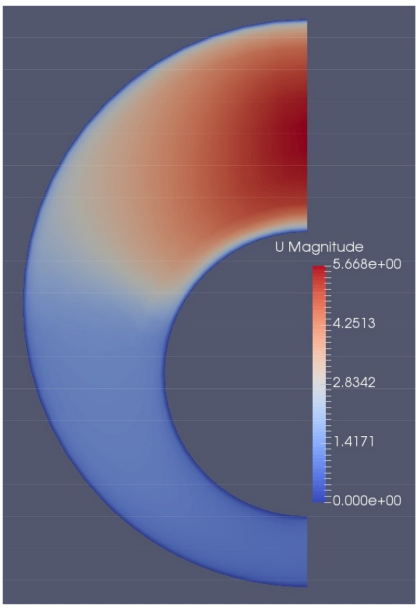

Fig. 25. Velocity field of simulation case #6, horizontal eccentric annulus (E = 0.5).

significantly better; however, we notice the expected pressure gradient increase when comparing simulations of a partly eccentric annulus with fully eccentric experiments.

As can be seen in Fig. 27, simulations 5 to 8 undergo a behavioral change for each case compared to cases 1–4. If we look past the average holdup increase, which is stipulated by the initial conditions, we can also notice that there are some fundamental changes to the holdup pattern. Case 2 has shifted from high frequency small waves (Fig. 5) to large periodic waves (Fig. 27, Sim case #6), or potentially proto-slug. The drastically altered pressure gradient solution suggests the simulation is in a different flow state compared to the experiment, which is an intriguing result of the eccentricity.

We also notice a similar change in the behavior of case 5. Past the initial transient, structures emerge that imply infrequent large waves or proto-slugs followed by a region of smaller waves as the holdup drops off. If wavy, this behavior is consistent with that seen during the experiments and signifies a drastic change to the flow regime when compared to the lower holdup case shown in Fig. 5.

It is important to note that the initial transient slug structure observed during simulation case 6 is likely formed by poor initial conditions, which results in a prolonged slug. For most cases, the resolution of the transient occurs during the first 5 s of the simulation. However, for this particular case with a very low average mixture velocity (1.2 m/s), the transient persists for nearly 15 s, after which the holdup behavior is closer to the experiment. Even so, the significant pressure gradient errors combined with the holdup pattern indicate that both simulation cases 5 and 6 behave fundamentally different compared to their experiment counterparts.

The slug frequencies of cases 7 and 8 are 0.84 and 0.88 Hz respectively. These values are consistent with the simulation cases 3 and 4. However, particularly for case 8 it is a marked decrease compared to the experiment which was 1.64 Hz.

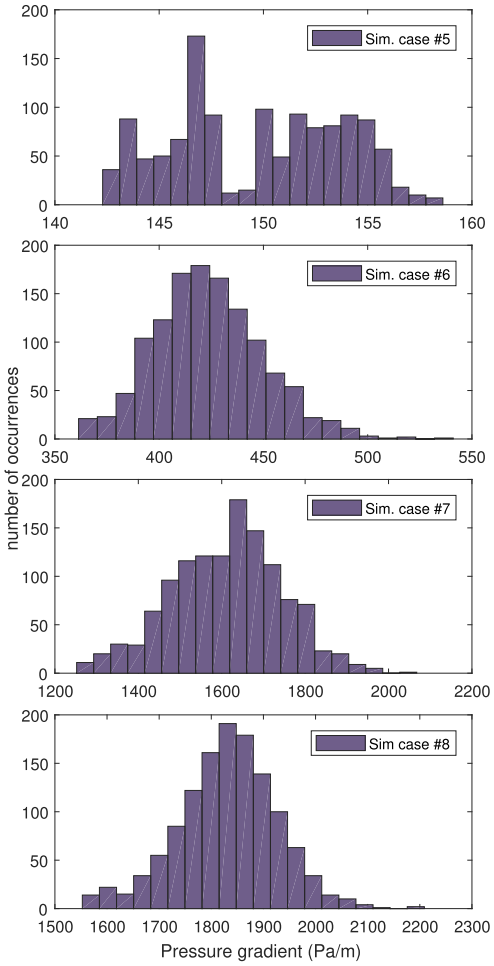

Fig. 26. Histogram of simulated pressure gradient for horizontal eccentric annulus with E = 0.5 and 100k cells/m.

Table 15
Pressure gradient summary for horizontal eccentric annulus (E = 0.5 and 100k cells/m), with mean, low (5%) and high (95%) threshold values.

Sim, #	5% (Pa/m)	mean (Pa/m)	95% (Pa/m)
5	143.45	149.69	155.67
6	384.25	423.59	467.41
7	1377.30	1612.39	1818.22
8	1662.94	1831.31	1981.58

Table 16
Relative difference of eccentric simulations (E = 0.5 and 100k cells/m) and eccentric experiments.

Sim #	5% (%)	mean (%)	95% (%)
5	838.2	312.7	58.5
6	413.0	311.5	241.3
7	92.0	67.8	36.4
8	61.2	51.8	41.03

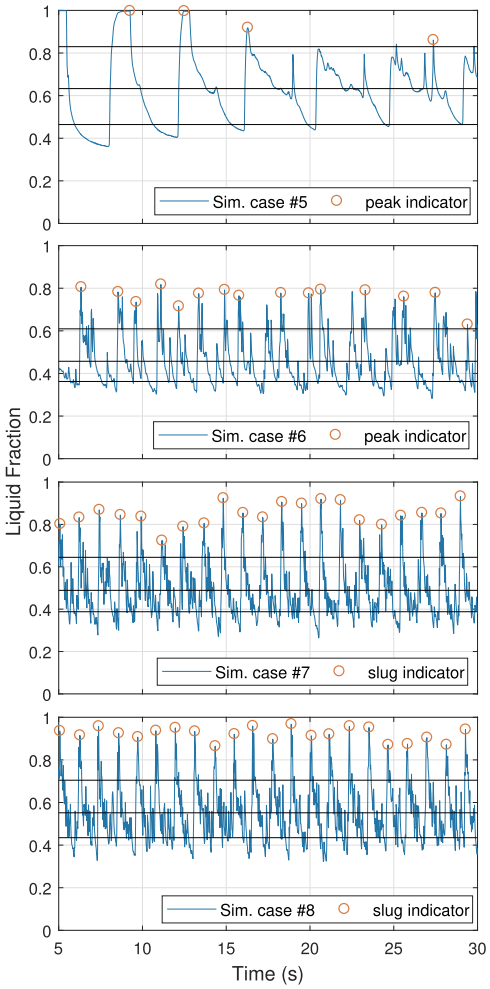

Fig. 27. Liquid holdup as a function of time for horizontal eccentric annulus with E = 0.5 and 100k cells/m. Peak indicators for proto-slug and waves as circles and horizontal lines indicating mean and slug and bubble thresholds.

5.2.3. 4 Degree inclined simulation with E = 0.5

We simulate the inclined eccentric case with the modified version of interFoam described briefly Section 3 and a 150k cells/m mesh within a 5 m domain. When using periodic boundary conditions, without this modification, the solver may be unable to converge regardless of the number of allowed iterations. The convergence problem for the unmodified interFoam becomes more prevalent with increasing inclination; however, for horizontal cases, the problem is non-existent.

The pressure gradient (Fig. 28) of the 4^o inclined simulation is several hundred Pa/m higher than the experiment case. This behavior is consistent with the other simulation cases, which are run at $E = 0.5$ while their experiment counterparts are at E = 1.0. Table 10 shows that for the experiments, the deviation from mean to the 5 and 95% thresholds is roughly 35–45% of the mean. Comparatively, the simulations maximum and minimum thresholds are within 10% of the mean pressure gradient value. Even when accounting for the increased mean pressure gradient, the numerical difference is still significantly smaller for the simulated case.

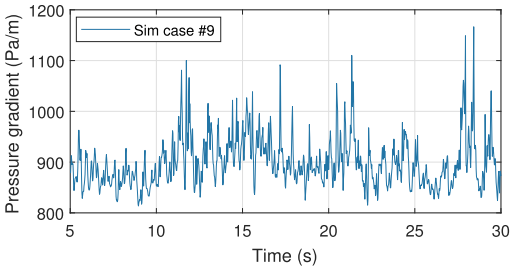

Fig. 28. Simulated pressure gradient as a function of time for 4° inclined eccentric simulation with E = 0.5 and 150k cells/m.

Table 17
Pressure gradient summary for 4° inclined eccentric simulation (E = 0.5 and 150k cells/m) with mean, low (5%) and high (95%) threshold values.

Sim #	5% (Pa/m)	Mean (Pa/m)	95% (Pa/m)
9	839.2	899.1	989.4

Compared to the fully eccentric experiments (Tab 10), we notice that there has been a significant increase in the simulated pressure gradient (Table 17). The minimum is increased by 118% while the mean and maximum are increased by 49 and 12% respectively. Keep in mind that we expect some increase in the pressure gradient because of the coarseness of the mesh. However, we believe the majority of this discrepancy is caused by the eccentricity of the simulations (E = 0.5) compared to the experiments (E = 1.0) and subsequent a relatively significant change in the flow regime (Figs. 12 and 30).

The histogram (Fig. 29) provides a second visual representation of the behaviour of the pressure gradient. As noted when discussing the threshold data (Table 17), when we cross-reference with the experiment histogram (Fig. 11), we notice that the bulk of the data is more concentrated about the mean and also that the distribution is altered. While for the experiment the distribution is closely resembling a Gaussian distribution, the simulation on the other hand is a right skewed distribution, with a few high pressure gradient data points extending the right tail to 1150 Pa/m.

The flow pattern (Fig. 30) appears to be representative of the experiments (Fig. 12); however, the peak holdup is slightly higher in the simulations. The simulation typically peaks at a liquid holdup of between 0.6 and 0.7, while the experiment rarely exceeds 0.6. The frequency of the holdup peaks is 0.76 Hz, which is 0.2 Hz higher than the experimental measurement. During the simulation, the flow regime which develops is reminiscent of the wavy flow identified from the experimental data (Fig. 12).

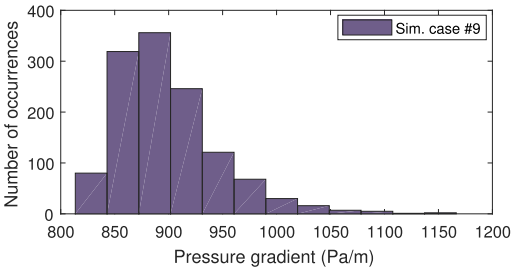

Fig. 29. Histogram of simulated pressure gradient for 4° inclined eccentric simulation with E = 0.5 and 150k cells/m.

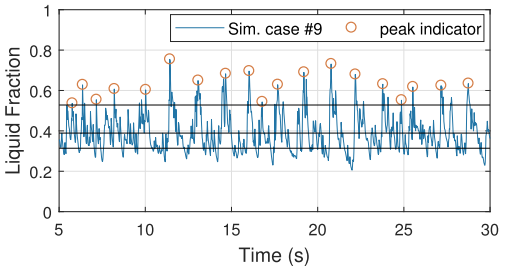

Fig. 30. Liquid holdup fraction as a function of time for inclined eccentric simulation (E = 0.5 and 150k cells/m). Peak indicators for waves as circles and horizontal lines representing mean holdup and bubble and slug threshold values.

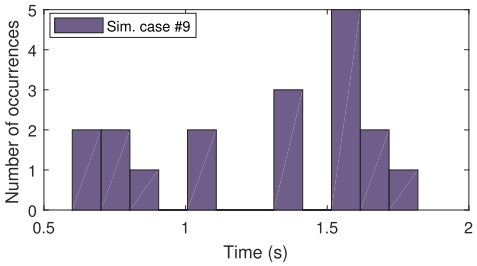

Fig. 31. Histogram of wave/proto-slug time-wise distribution for 4° inclined eccentric (E = 0.5) simulations with 150k cells/m.

In summary, the holdup pattern and peak frequency are in good agreement with the experiments however we experience an elevated pressure gradient, in particular of the minimum pressure gradient. The pressure gradient increase is slightly larger than what is expected from the difference in eccentricity of the two cases. However, we typically observe a moderate pressure gradient increase at this mesh density.

The average proto-slug/large wave frequency is 0.76 Hz, with the majority of instances separated in two intervals between 0.5 to 1.1 s and 1.3 to 1.8 s. The distribution of simulated wave (Fig. 31) events coincides with the large wave distribution observed in the experiment (Fig. 14)

6. Conclusions

Two-phase flow simulations were run in an eccentric annulus using OpenFoam and periodic boundary conditions. The simulations consist of 9 individual cases, of which 8 are horizontal, and 1 is inclined at 4°. The annulus eccentricity was 0.5 for all cases.

For the horizontal domain, the simulations resulted in two distinct flow regimes. We compared the simulations with experimental data collected in both a fully eccentric and fully concentric configuration in order to study the effect of altering the eccentricity. The flow regimes of the experiments were wavy flow or slug flow; the simulations represented these well in all but two cases (5 & 6), where we arguably observe an altered flow state as an effect of the different eccentricity. We show that altering the liquid fraction and location of the inner pipe has an effect on the flow, such as altering the wave and slug frequency, increasing the pressure gradient, and in simulation cases 5 and 6 transitioning the flow to a different flow state.

The horizontal cases simulated were split into cases referred to as 1–4 and 5–8. These two sets are cases with the same mixture velocity; however, different fluid fractions. In experiment, they result in similar

flow regimes with some minor differences with regard to wave and slug frequency (5 & 8) as well as pressure gradient (4 & 7).

As noted in previous works (Friedemann et al., 2019), the slug structures noted in the simulations resemble proto-slugs, a precursor to a slug, which tends to leave a gap near the upper wall filled with gas. The cause of the void is thought to be an inability to resolve minor bubbles, which would typically permeate through the liquid layer of the slug. When the VOF type solver interFoam is not able to resolve these, the gas bubbles tend to coalesce and rise to the top in order to follow conservation laws.

By comparing the experimental data with the simulations, we can establish that we can simulate both wavy and flow resembling slug structures within an eccentric domain. The cases conform to the experimental data within reasonable tolerance with regards to holdup pattern. However, we notice a significant discrepancy of the pressure gradient results due to a change of eccentricity.

We did not expect that the simulations would be perfect replications for several reasons. One is that the simulations utilize periodic boundary conditions, which impose some restrictions on the results. For example, the domain length can affect the number of slugs present and thereby alter the slug frequency. The geometry simulated has an eccentricity of 0.5, while the experiments are at E = 0 and E = 1.0. We purposefully adjusted the eccentricity of the simulation cases to analyze the impact of eccentricity on the pressure gradient and flow regime.

The most significant deviations from experiments occur when comparing results with a completely eccentric experiment (E = 1.0). For one wavy flow case, we observed a mean pressure gradient increase of as much as 303% (Table 16). The simulation slug case results are generally closer to the experimental case results, and the deviation caused by the change of eccentricity is within 65% for the cases where we compare to an eccentric experiment, and 20% when comparing to a concentric experiment (Tables 12 and 14). Based on previous work, the mesh densities studied here typically overestimate the pressure gradients by a modest amount. While a finer mesh reduces the mesh associated errors, the simulation time is sufficiently prohibitive that we opted for the coarser mesh.

Through these studies, we have learned about the effect of eccentricity on the flow regime and pressure gradient. We notice that the pressure gradient of the slug flow cases behave as expected, the reduction of the pressure gradient corresponds with an increased eccentricity, and vice versa. We also note that for the low velocity cases, the simulations tend to overestimate the pressure gradient significantly; however, they too conform to the expected effect of eccentricity as we note a smaller over-prediction when increasing the eccentricity. The flow regime shows a lesser dependence on eccentricity for the slug cases than the wavy flow cases. In particular, for simulation case # 2, we notice a significantly increased wave frequency when compared to the corresponding experiment. Through the cases studied, we establish that both the flow regime and pressure gradient is altered through the location of the interior pipe. While we do not observe a complete change of flow regime, we do observe mostly minor changes in the wave and slug frequency accompanied by significant changes to the pressure gradient.

CRediT authorship contribution statement

C. Friedemann: Methodology, Software, Validation, Formal analysis, Investigation, Data curation, Writing - original draft, Writing - review & editing, Visualization. **M. Mortensen:** Software, Resources, Writing - review & editing, Supervision. **J. Nossen:** Conceptualization, Methodology, Resources, Writing - review & editing, Supervision, Project administration, Funding acquisition.

Acknowledgements

This work is part of a larger project called Multiphase Flow in Concentric and Eccentric Annulus Spaces (project number 255481) and has been performed thanks to funding from the Research Council of Norway through the PETROMAKS2 programme.

References

Adachi, T., Imai, S., 2007. Three-dimensional linear stability of natural convection in horizontal concentric annuli. Int. J. Heat Mass Transf. 50, 1388–1396. https://doi.org/10.1016/j.ijheatmasstransfer.2006.09.029.
Archibong-Eso, A., Baba, Y., Nsefik-Eyo, E., Enyia, J., Ikpe, I., 2016. A study of two-phase air-water flow in horizontal and inclined pipelines. Int. J. Sci. Eng. Res. 7, 296–303.
Beggs, D., Brill, J., 1973. A study of two-phase flow in inclined pipes. J. Petroleum Technol. 25, 607–618. https://doi.org/10.2118/4007-PA.
Benoit, L., Nguyen, M., Peixinho, J., Shadloo, M., A.Hadjadj, 2018. A new mechanism for periodic bursting of the recirculation region in the flow through a sudden expansion in a circular pipe. Phys. Fluids 30 (3), 031701. https://doi.org/10.1063/1.5022872.
Berberovic, E., 2010. Investigation of Free-surface Flow Associated with Drop Impact: Numerical Simulations and Theoretical Modeling. TU Darmstadt Ph.D. thesis.
Blinkov, V., Boltenko, E., Elkin, I., Melikhov, O., Solovev, S., 2010. Prospects for using annular fuel elements in nuclear power engineering. Therm. Eng. 57, 213–218. https://doi.org/10.1134/S0040601510030043.
Bonnecaze, R., Jr, W.E., Greskovich, E., 1971. A study of two-phase flow in inclined pipes. Am. Inst. Chem. Eng. J. 17, 1109–1113. https://doi.org/10.1002/aic.690170516.
Buyruk, E., Barrow, H., Owen, I., 1999. Heat transfer in laminar flow in a concentric annulus with peripherally varying heat transfer. Int. J. Heat Mass Transf. 42 (3), 487–496. https://doi.org/10.1016/S0017-9310(98)00166-5.
Caetano, E., 1985. Upward Vertical Two-Phase Flow Through an Annulus. The University of Tulsa Ph.D. thesis.
Chen, J., Spedding, P., 1981. An extension of the lockhart-martinelli theory of two phase pressure drop and holdup. Int. J. Multiphase Flow 7, 659–675. https://doi.org/10.1016/0301-9322(81)90037-9.
Das, G., Das, P., Purohit, N., Mitra, A., 1998. Rise velocity of a taylor bubble through concentric annulus. Chem. Eng. Sci. 53, 977–993. https://doi.org/10.1016/S0009-2509(97)00210-8.
Das, G., Das, P., Purohit, N., Mitra, A., 2000. Phase distribution of gas-liquid mixtures in concentric annuli-inception and termination of asymmetry. Int. J. Multiphase Flow 26, 857–876. https://doi.org/10.1016/S0301-9322(99)00034-8.
Denton, J., 1963. Turbulent Flow in Concentric and Eccentric Annuli. The University of British Columbia Master's thesis.
Deokule, A., Vishnoi, A., Umasankari, K., Chandraker, D., Vijayan, P., 2015. Reactor physics adn thermal hydraulic analysis of annular fuel rod cluster for advanced heavy water reactor. Energy Procedia 71, 52–61. https://doi.org/10.1016/j.egypro.2014.11.854.
Desphande, S., Anumolu, L., Trujilo, M., 2012. Evaluating the performance of the two-phase flow solver interfoam. Comput. Sci. Discov. 5, 14–16. https://doi.org/10.1088/1749-4699/5/1/014016.
Dukler, A., Taitel, Y., 1986. Flow pattern transitions in gas-liquid systems: measurements and modeling. Vol. 2. pp. 1–94. 10.1007/978-3-662-01657-2_1.
Escudier, M.P., Gouldson, I.W., Jones, D.M., 1995. Flow of shear-thinning fluids in a concentric annulus. Exp. Fluids 18, 225–238.
Friedemann, C., Mortensen, M., Nossen, J., 2019. Gas-liquid slug flow in a horizontal concentric annulus, a comparison of numerical simulations and experimental data. Int. J. Heat Fluid Flow 78. https://doi.org/10.1016/j.ijheatfluidflow.2019.108437.
Ghajar, A., Bhagwat, S., 2014. Gas-liquid two phase flow phenomenon in near horizontal upward and downward inclined pipe orientations. Int. J. Mech. Mechatron. Eng. 8, 1091–1105.
Hanks, R.W., Bonner, W.F., 1971. Transitional flow phenomena in concentric annuli. Ind. Eng. Chem. Fundament. 10 (1), 105–113. https://doi.org/10.1021/i160037a018.
Harvel, G., Hori, K., Kawanishi, K., Chang, J., 1999. Cross-sectional void fraction distribution measurements in a vertical annulus two-phase flow by high speed x-ray computed tomography and real-time neutron radiography techniques. Flow Meas. Instrum. 10 (4), 259–266. https://doi.org/10.1016/S0955-5986(99)00008-4.
Hasan, A., Kabir, C., 1992. Two-phase flow in vertical and inclined annuli. Int. J. Multiphase Flow 18, 279–293. https://doi.org/10.1016/0301-9322(92)90089-Y.
Hibiki, T., Situ, R., Mi, Y., Ishii, M., 2003. Local flow measurements of vertical upward bubbly flow in an annulus. Int. J. Heat Mass Transf. 46, 1479–1496. https://doi.org/10.1016/S0017-9310(02)00421-0.
Hills, J., Chéty, P., 1998. The rising velocity of taylor bubbles in an annulus. Chem. Eng. Res. Des. 76, 723–727. https://doi.org/10.1205/026387698525423.
Hosseini, R., Ramezani, M., Mazaheri, M., 2009. Experimental study of turbulent forced convection in vertical eccentric annulus. Energy Convers. Manage. 50, 2266–2274. https://doi.org/10.1016/j.enconman.2009.05.002.
Hout, R., Shemer, L., Barnea, D., 2003. Evolution of hydrodynamic and statistical parameters of gas-liquid slug flow along inclined pipes. Chem. Eng. Sci. 58, 115–133. https://doi.org/10.1016/S0009-2509(02)00441-4.
Høyland, L., Papatzacos, P., Skjaeveland, S., 1989. Critical rate for water coning: correlation and analytical solution. SPE Reservoir. Eng. 4, 495–502. https://doi.org/10.2118/15855-PA.
Ibarra, R., Nossen, J., Tutkun, M., 2019. Holdup and frequency characteristics of slug flow in concentric and fully eccentric annuli pipes. J. Petroleum Sci. Eng. 182. https://doi.org/10.1016/j.petrol.2019.106256.
Ilic, V., 1986. Two phase pressure drop in an inclined pipe. 9th Australasian fluid mechanics conference. Auckland, Australia. pp. 196–199.
Iyer, S., Vafai, K., 1998. Buoyancy induced flow and heat transfer in a cylindrical annulus

with multiple perturbations. Int. J. Heat Mass Transf. 41 (20), 3025–3035. https://doi.org/10.1016/S0017-9310(98)00053-2.
Kelessidis, V., Dukler, A., 1989. Modeling flow pattern transitions for upward gas-liquid flow in vertical concentric and eccentric annuli. Int. J. Multiphase Flow 15 (2), 173–191. https://doi.org/10.1016/0301-9322(89)90069-4.
Kelessidis, V., Dukler, A., 1990. Motion of large gas bubbles through liquids in vertical concentric and eccentric annuli. Int. J. Multiphase Flow 16 (3), 375–390. https://doi.org/10.1016/0301-9322(90)90070-Y.
Liu, L., Jiang, P., Li, X., 2015. Mechanical energy losses in horizontal, inclined, and vertical intermittent two-phase flows with drag-reducing polymer. Chem. Eng. Commun. 202, 864–875. https://doi.org/10.1080/00986445.2013.867261.
Michiyoshi, I., Nakajima, T., 1968. Fully developed turbulent flow in a concentric annulus. J. Nucl. Sci. Technol. 5, 354–359. https://doi.org/10.1080/18811248.1968.9732470.
Mizushima, J., Hayashi, S., Adachi, T., 2001. Transitions of natural convection in a horizontal annulus. Int. J. Heat Mass Transf. 44, 1249–1257. https://doi.org/10.1016/S0017-9310(00)00188-5.
Nguyen, M.Q., Shadloo, M.S., Hadjadj, A., Lebon, B., Peixinho, J., 2019. Perturbation threshold and hysteresis associated with the transition to turbulence in sudden expansion pipe flow. Int. J. Heat Fluid Flow 76, 187–196. https://doi.org/10.1016/j.ijheatfluidflow.2019.01.018.
Nikitin, N., WANG, H., Chernysenko, S., 2009. Turbulent flow and heat transfer in eccentric annulus. J. Fluid Mech. 638, 95–116. https://doi.org/10.1017/S002211200900812X.
Nuland, S., 1999. Bubble fraction in slugs in two-phase flow with high viscosity liquid. Proceedings of the 2nd International Symposium on Two-phase Flow Modeling and Experimentation. Pisa, Italy. https://doi.org/10.1088/1757-899X/121/1/012018.
Oddie, G., Shi, H., Durlofsky, L., Azis, K., Pfeffer, B., Holmes, J., 2003. Experimental study of two and three phase flows in large diameter inclined pipes. Int. J. Multiphase Flow 29, 527–558. https://doi.org/10.1016/S0301-9322(03)00015-6.
Ozar, B., Jeong, J., Dixit, A., Juli, J., Hibiki, T., Ishii, M., 2008. Flow structure of gas-liquid two-phase flow in an annulus. Chem. Eng. Sci. 63, 3998–4011. https://doi.org/10.1016/j.ces.2008.04.042.
Perez, V., Azzopardi, B., Morvan, H., 2007. Slug flow in inclined pipes. 6th International Conference on Multiphase Flow. Leipzig, Germany.
Salem, A., 2008. Multiphase flows in horizontal and inclined pipelines by CFD simulations. The 5th Mediterranean Offshore Conference and Exhibition. Alexandria, Egypt.
Sato, H., Ohashi, H., Tachibana, Y., Kunitomi, K., Ogawa, M., 2013. Thermal analysis of heated cylinder simulating nuclear reactor during loss of coolant accident. J. Nucl. Sci. Technol. 51, 1317–1323. https://doi.org/10.1080/00223131.2014.919883.
Schulkes, R., 2011. Slug frequencies revisited. 15th International Conference on Multiphase Production. Cannes, France. pp. 311–325.
Strazza, D., Grassi, B., Demori, M., Ferrari, V., Poesio, P., 2011. Core-annular flow in horizontal and slightly inclined pipes: existence, pressure drops and hold-up. Chem. Eng. Sci. 66, 2853–2863. https://doi.org/10.1016/j.ces.2011.03.053.
Sun, L., Peng, M., Xia, G., Lv, X., Li, R., 2017. Numerical study on coolant flow distribution at the core inlet for an integral pressurized water reactor. Nucl. Eng. Technol. 49, 71–81. https://doi.org/10.1016/j.net.2016.07.005.
Taitel, Y., Barnea, D., Dukler, A.E., 1980. Modelling flow pattern transitions for steady upward gas-liquid flow in vertical tubes. AlChE J. 26 (3), 345–354. https://doi.org/10.1002/aic.690260304.
Taitel, Y., Dukler, A., 1976. A model for predicting flow regime transitions in horizontal and near horizontal gas-liquid flow. AlChE J. 22, 47–55. https://doi.org/10.1002/aic.690220105.
Vaughn, R., 1963. Laminar flow of non-newtonian fluids in concentric annuli. Soc. Petroleum Eng. 3, 274–276. https://doi.org/10.2118/615-PA.
Wein, O., Nebrensky, J., Wichterle, K., 1970. Non-newtonian flow in annuli. Rheol. Acta 9, 278–282. https://doi.org/10.1007/BF01973488.
Wongwises, S., Pipathattakul, M., 2006. Flow pattern, pressure drop and void fraction of two-phase gas-liquid flow in an inclined narrow annular channel. Exp. Therm. Fluid Sci. 30, 345–354. https://doi.org/10.1016/j.expthermflusci.2005.08.002.
Yoo, J., 2003. Dual free-convective flows in a horizontal annulus with a constant heat flux wall. Int. J. Heat Mass Transf. 46, 2499–2503. https://doi.org/10.1016/S0017-9310(02)00539-2.
Yu, B., Kawaguchi, Y., Kaneda, M., Ozoe, H., Churchill, S., 2005. The computed characteristics of turbulent flow and convection in concentric circular annuli. part ii. uniform heating on the inner surface. Int. J. Heat Mass Transf. 48, 621–634. https://doi.org/10.1016/j.ijheatmasstransfer.2004.08.022.

Paper III

Two-phase co-current flow simulations using periodic boundary conditions in horizontal, 4, 10 and 90^o inclined eccentric annuli, flow prediction using a modified interFoam solverand comparison with experimental results

C. Friedemann, M. Mortensen, J. Nossen

To be published in International Journal of Heat and Fluid flow, April 2021, volume 88, DOI:10.1016/j.ijheatfluidflow.2020.108754

III

International Journal of Heat and Fluid Flow 88 (2021) 108754

Contents lists available at ScienceDirect

International Journal of Heat and Fluid Flow

journal homepage: www.elsevier.com/locate/ijhff

Two-phase co-current flow simulations using periodic boundary conditions in horizontal, 4, 10 and 90° inclined eccentric annulus, flow prediction using a modified interFoam solver and comparison with experimental results

C. Friedemann [a,*], M. Mortensen [a], J. Nossen [b]

[a] Department of Mathematics, University of Oslo, Moltke Moes vei 35, 0851 Oslo, Norway
[b] Institute for Energy Technology, 2007 Kjeller, Norway

ARTICLE INFO

Keywords:
Annulus
Slug flow
Wavy flow
Churn Flow
Volume of fluid
Reynolds-averaged Navier–Stokes equations

ABSTRACT

Two-phase oil and gas flow were simulated in an entirely eccentric annulus and compared with experimental data at horizontal, 4, 10, and 90° inclination. The gas-phase was sulphur hexafluoride and the liquid phase a mixture of Exxsol D60 and Marcol 82 for the inclined cases (5–16), and pure Exxsol D60 for the horizontal cases (1–4). The diameter of the outer and inner cylinders was 0.1 and 0.04 m, respectively, for the inclined domains and 0.1 and 0.05 m for the horizontal domain. The cases studied consist of liquid phase fractions between 0.3 and 0.65 and mixture velocities from 1.2 to 4.25 m/s. The mean pressure gradient is within 33% of the expected experimental behavior for all inclined cases. In contrast, the low-velocity horizontal domains exhibit significant deviation, with a drastic over-prediction of the mean pressure gradient by as much as 200–335% for cases 1 and 2. The two remaining horizontal cases (3 and 4) are within 22% of the expected mean pressure gradient. Cases 13–16 are a replication of cases 5–8 at an increased inclination; the mean pressure gradient is within 6.5% of the expected increase due to the increase in hydrostatic pressure. By comparing cases 1–4 to previous published simulations at a lower eccentricity, we found a decrease of the mean pressure gradient by 30–40%, which is in line with existing literature, although for single-phase flows. The simulated and experimental liquid holdup profiles are in good agreement when comparing the fractional data; wave and slug frequencies match to within 0.5 Hz; however, at closer inspection, it is apparent that there is a decrease in the amount of phase-mixing of the simulations compared to the experiments. When increasing the mesh density from 115 k cells/m to 2 million cells/m, the simulations exhibit significantly more phase mixing, but are still unable to produce conventional slugs. In a simplified case, conventional slugs are observed at grid sizing of $1 \times 1 \times 1$ mm, whereas the cells of the 2 million cells/m mesh are roughly $1.5 \times 1.5 \times 1.5$ mm.

1. Introduction

The study of two-phase flow through simulations is a complex and time-consuming exercise, yet important in order to complement the existing experimental literature. It is crucial to understand multiphase flow within an annulus, because of its purpose and prevalence in industry. In the petroleum industry, annuli are found within wells and pipe-in-pipe heating systems in pipelines and risers and transients, pressure gradient and flow regime prediction are imperative for flow assurance, pipeline maintenance and design. In the nuclear industry, similar geometries are found related to the cooling rods, and it is even found in the aerospace industry within the combustion chamber of an engine. These industries share the potential for catastrophic failures to occur, which will impact the environment and ecosystem, and potentially prove fatal.

Simulations allow us to gaze into the behavior of flow within complicated geometries. Several facets make the annulus geometry studied in this work a complex problem, such as the size and relative positions of the two cylinders. In addition, the annulus configuration represents a simplified version of more complex geometries, including rod bundles in a nuclear reactor (Julia and Hibiki, 2011). Fluid interaction with the interior cylinder also causes the friction factor to be a

* Corresponding author.
E-mail address: chrisjfr@student.matnat.uio.no (C. Friedemann).

https://doi.org/10.1016/j.ijheatfluidflow.2020.108754
Received 10 April 2020; Received in revised form 14 September 2020; Accepted 12 November 2020
Available online 18 January 2021

function of the annulus eccentricity.

One of the factors studied in this work is the effect of eccentricity, while all present cases are fully eccentric, the effect is studied based on previous published work (Friedemann et al., 2020). Eccentricity is a measure of the relative positions of the cylinder centers. The annulus is fully eccentric when the distance between the two cylinder centers is maximized, while the annulus is concentric when the centers coincide. Although it is easily assumed that the friction factor is increased due to the surface area introduced through the inner cylinder, multiple sources state that for an eccentric annulus, the friction factor is always lower than for an equivalent hollow pipe, and the opposite for a concentric annulus (Denton, 1963; Caetano, 1985). In addition, the rate of change of the friction factor is not linear and depends on whether the flow is turbulent or laminar (Hanks and Bonner, 1971). We must also consider the variable interface as the liquid height varies with the flow regime leaving a thin liquid lubricating film on the cylinder. For periodic flow, such as slugs or waves, the cross-sectional holdup oscillates, thereby creating a variable phase-interaction with the cylinder walls.

The annulus configuration has been studied experimentally since the early 1960s, when Denton (1963) wrote his thesis on turbulent flow in a concentric annulus and Vaughn (1963) studied laminar flow of non-Newtonian fluids. However, these studies were based on single-phase flows; two-phase flow models were developed at a significantly later time.

The modern-day study of two-phase annulus flow was initiated by Kelessidis and Dukler (1989) and Kelessidis and Dukler (1990), who published several papers on vertical gas–liquid flow, discussing flow regime transition point modeling. Their work could be seen as an extension of the correlation-based modeling for horizontal (Taitel and Dukler, 1976) and vertical (Taitel et al., 1980) tubing. Although correlations are a historically significant part of multiphase-flow studies, they have one crucial flaw; they are by nature extremely application sensitive. Factors that may interfere with a correlation model's accuracy are fluid properties, annulus dimensions, flow rates and holdup fractions, as mentioned by Julia and Hibiki (2011), and shown by Ozar et al. (2008) in their work related to modeling of transition points of two-phase flow in an annulus. Beyond transition point modeling and flow regime mapping, studies have explored pressure losses (Erge et al., 2015; Ozbayoglu and Sorgun, 2010), pressure gradients (Ferroudji et al., 2019; Ibarra and Nossen, 2019), void fractions (Harvel et al., 1999), heat transfer (Hamad et al., 1998), slug frequencies, and Taylor bubble rise velocity (Das et al., 1998; Hills and Chéty, 1998).

Although there are recent computational studies, such as the research by Kiran et al. (2020) using Fluent to study annular flow in a vertical annulus and the work by Friedemann et al. (2019) and Friedemann et al. (2020) analyzing pressure gradients and slug frequencies in concentric and partly eccentric annuli, the vast majority of multiphase studies are experimental. However, there are several published articles that focus on other aspects of computational annulus flow including those analyzing buoyancy induced flows (Iyer and Vafai, 1998), turbulent flow and heat transfer (Nikitin et al., 2009), and natural convection (Adachi et al., 2007; Mizushima et al., 2001; Yoo, 2003; Yu et al., 2005).

Before simulations can be considered as predictive of behavior within a flow conduit, it is essential to verify simulations with experiments. The authors have previously worked on horizontal simulations in a concentric annulus configuration (Friedemann et al., 2019) and shown that the simulations are accurate within 25% of the expected pressure gradient and within 10% of the expected slug frequency. However, some simulation artifacts are hard to minimize; for example that conventional slugs are replaced by proto-slugs. A proto-slug is a structure that behaves as a slug but falls short of fulfilling conventional slug criteria. Mainly, it is observed that the proto-slug seldom covers the cross-section. It is possible that the proto-slugs stem from a lack of mesh resolution and thereby an inability to resolve minor bubbles immersed within the liquid. In simplified slices conventional slugs occur when the mesh elements are 1x1x1 mm. For coarse meshes, large gas bubbles accumulate toward the top of the annulus as their rise velocities are higher and thus they are more likely to overcome the turbulent dispersion as compared to smaller bubbles. In a typical slug, small gas bubbles permeate through the liquid, which we observe in the simplified slices; however, there are other possible explanations such as surface tension, wall effects, and choice of boundary conditions.

Pressure gradient transients are essential for industrial applications because it affects the operating limits, maintenance schedule, cost, and impact of potential ruptures. Flow regime and slug frequencies are also crucial; with this information, preventive steps can be taken to minimize slugging using slug catchers (gas/liquid pre-separators that can accommodate large slugs) and establish accurate leakage estimates in the case of a malfunction using slug frequency and holdup fractions as estimation parameters.

Finally, there is inclination, which is an essential parameter to study due to its effect on flow regime and pressure drop (Wongwises et al., 2006). There may be various solutions for transport in specific petroleum fields; some pipelines extend along the seabed, while others run vertically up to an offshore facility (Ozbayoglu et al., 2012). Different transport solutions suggest we have to account for the effect of a variable inclination. Therefore, the 10° cases are simply the 4° cases at a higher inclination, in order to study potential changes, such as backflow in the narrow region of the annulus or in the film region of a slug (Hernandez-Perez, 2008). Inclined flow is a perfect candidate for CFD studies, due to the physical restrictions imposed on an inclined experimental flow loop. In order to study inclined flow, the test section must be long for the flow to fully develop. Physical restrictions are easily overcome computationally; however, simulations come with their own limitations, mostly related to the solution time's exponential scaling tied to mesh density.

Although CFD as a tool to study multiphase flow is becoming more prevalent, extensive studies for annuli are rare. Furthermore, horizontal and vertical configurations dominate the existing literature. In this paper, a small spectrum is studied; horizontal, 4°, 10° and vertical. Ideally, steep inclinations would also be studied, but preliminary studies indicate that periodic boundary conditions and steep inclinations produce an unexpected amount of back-flow. Given the theoretical framework, the solutions are possible and highlight that periodic boundary conditions do have some problems. Studies must be careful to examine whether the behavior is representative of experimental results. The amount of liquid within the domain is determined by the initial conditions; therefore, simulating slug flow in a too short domain could result in insufficient liquid to form slugs. Similarly, if the domain length is an odd multiple of the slug to slug length, then the slug frequency could be affected.

Prohibitive solution time is another drawback. Periodic boundary conditions alleviate the computational demands by simulating an "infinite" pipe. With normal boundary conditions, in order for a slug to form, the domain needs to allow the flow to transition from a stratified inlet flow. The required domain length depends on the flow regime and phase properties. Ideally, the domain would be of the same size as the experimental loop which in our case, translates to 50 m. The fastest of our current simulations took roughly three weeks on four cores when each core was assigned 200 k cells. Axtmann et al. (2016) studied the scalability of OpenFOAM and suggests 15–20 k cells/core. We experience that the scaling reduces at around 80 k cells/m. It should be noted that Axtmann's research was done on single-phase flows, and that scaling can depend on the network configuration and communication protocols. If we extend the domain to 50 m and assume the scaling stays constant, each simulation would require 40 cores. Unfortunately, with our computational resources, that is not a viable option while covering several configurations and initial conditions.

The focus of this paper is two-phase flow within an entirely eccentric annulus. The flow behavior in four inclinations; 0, 4, 10, and 90° is studied using a modified (inclined) version of the OpenFOAM solver interFoam and regular interFoam (horizontal), in combination with periodic boundary conditions. These horizontal simulations are similar

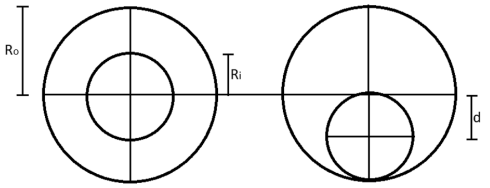

Fig. 1. Eccentricity of annulus, R_o = outer cylinder radius, R_i = inner cylinder radius, d = distance between cylinder centers.

to and share experimental data with previous simulations which were partly eccentric (E = 0.5) (Friedemann et al., 2020), with the main difference being the use of an entirely eccentric annulus. Even minor changes to the eccentricity of the annulus can have a significant effect on the flow regime, pressure gradient, and velocity profile, therefore the present simulations should be considered a novel geometry. Each simulation is accompanied by an experiment, except the 10° simulations which are a modified iteration of the 4° simulations. The experimental mixture velocity and phase fractions are used to initialize the simulations while we compare the pressure gradient, flow regime, wave or slug frequency, and the effect of a change of inclination on the above parameters.

Although CFD has come a long way since its inception, it is likely still too early to consider CFD robust and error-proof enough to replace, mechanistic models, correlations and flow regime maps for two-phase flows with petroleum applications. However, combining CFD with experimental data and comparing the results, eventually CFD can at the very least supplement the existing experimental data bases with additional metrics which are easier to evaluate through CFD and potentially be considered predictive with enough research and validation, especially for geometries that are difficult to study in a laboratory environment. This paper is a step towards prediction and validation.

2. Geometry and mesh

The geometry studied is an approximation of a fully eccentric annulus, the outer cylinder diameter is 0.1 m for all cases, while the interior cylinder diameter is 0.05 (horizontal) and 0.04 m (inclined). The domain is studied in both horizontal and inclined orientations. The inclined (and vertical) cases are at 4,10 and 90°. The eccentricity (E) of the annulus is defined a function of the radii of the inner (R_i) and outer (R_o) cylinder, as well as the distance between cylinder centers (d) as illustrated in Fig. 1 and expressed in Eq. (1)

$$E = \frac{d}{R_o - R_i}. \tag{1}$$

Eccentricity plays an essential role on flow formation by affecting the friction factor. When the distance between the cylinder centers is maximized, the annulus is fully eccentric, while an annulus where the centers coincide is fully concentric. The annulus is designed with the interior cylinder resting against the bottom wall of the outer cylinder, there is a tiny gap (0.5 mm) between two cylinders modeled as a wall, resulting in E = 0.983 and 0.98 for the inclined and horizontal domains respectively.

Meshing an eccentric annulus is complicated due to the tiny gap between the cylinders where the walls converge. Because OpenFOAM prefers hexahedral elements, in order to have the majority of elements well arranged, there are two small regions of distorted elements. The elements in question are mostly within the region where the flow velocity is decreased due to wall effects. OpenFOAM's built-in tools report no overly skewed or distorted elements, and the maximum skewness and non-orthogonality are within the OpenFOAM accepted limits of 70 for non-orthogonality and 4 for cell skewness, the maximum non-orthogonality is 65, and cell skewness is 0.68, while the average non-orthogonality is 16.

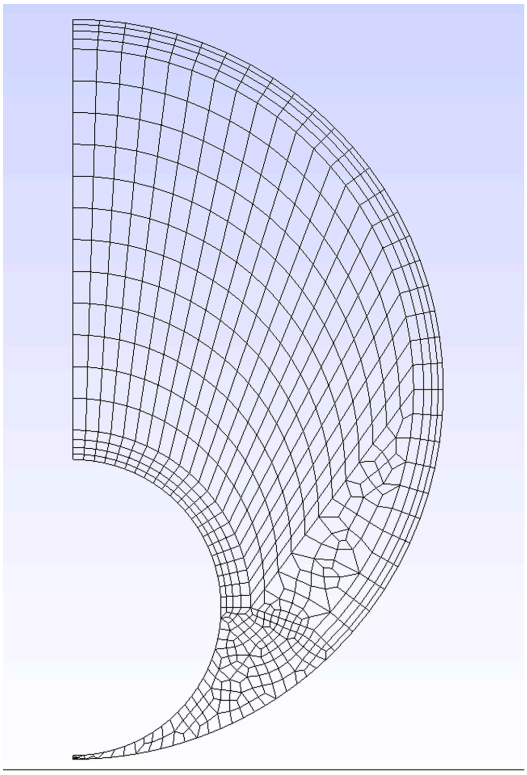

Fig. 2. Cross-sectional view of computational domain with R_0 = 5 cm and R_i = 4 cm.

The meshes employ a constant axial cell spacing of 3.9 mm, while the cross-sectional cell size vary as a function of the wall to wall distance (Fig. 2). Each mesh is approximately 115 k cells/m unless otherwise specified, and the domains utilized are 5 m in the inclined cases and 7 m for the horizontal cases. The walls are treated with wall functions, which relax the resolution requirements. The available wall functions are so called adaptive wall functions, which allows the first cell center to be located either within the log-layer or within viscous sub-layer (Kalitzin et al., 2005; Liu, 2016), some are even reportedly acceptable within the buffer layer, although steps were made to avoid this region. The viscous sublayer is located at dimensionless wall distance (y^+) below 5, and the log-layer exists for $30 \leqslant y^+ \leqslant 200$. For the 16 cases presented, the average y + is $38 \leqslant y^+ < 68$.

The initial conditions for the flow field was described using built-in OpenFOAM commands, and was based on the holdup fractions,mixture and superficial velocities attained from the experimental data (Fig. 1). For the horizontal and low inclination simulations, the flow was initialized as a stratified flow with holdup fractions and slip velocity according to the phase velocities, while the vertical simulations were initialized as intermittent sections of oil and gas. For all cases the flow is driven by a momentum-source equivalent to the experiment mixture velocity, this momentum-source is specified in the case files.

Periodic boundary conditions are applied to the domain. The entire flow field is thus transferred seamlessly through two "adjacent" patches, in this case the inlet and outlet. The flow transfer ensures that even in a short domain the flow field is allowed to developed in an "infinite" pipe. With this approach, some flows like wavy flow are almost independent

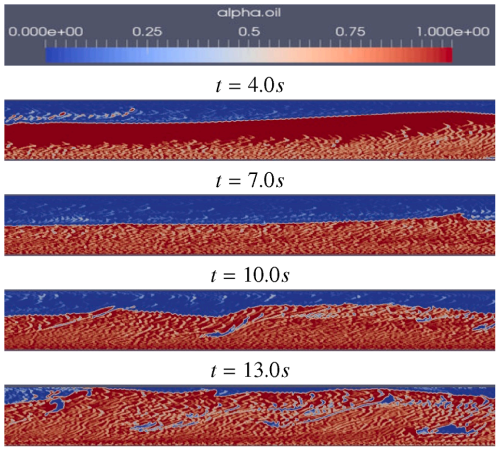

Fig. 3. Snapshots of simplified geometry inclined at 4° with gas in blue and liquid in red and cell volume = $1e-9\ m^3$.

of domain length, while other flows like slug flow could be drastically altered due to the set amount of liquid within the system (Frank, 2005; Friedemann et al., 2019). The slug frequency dependency occurs because the phase fractions are set by the initial conditions. Therefore, it is essential to pay close attention to specific parameters such as slug to slug length and phase velocities when creating a domain with the intent of utilizing periodic boundary conditions.

Vertical domains are less reliant on the domain's length as there are fewer domain length-dependent structures such as slugs. As we know, most slugs are a mixture of liquid and gas. By restricting the amount of liquid within the domain, if the domain length is not scaled to an integer value of the slug to slug length, then the slug frequency could be severely altered. The effect is minimized in domains with space for several concurrent slugs. Lastly, the low mesh density restricts bubble formation because the mesh is too coarse to resolve minor gas bubbles within the liquid layer. Instead, the gas tends to coalesce and form large bubbles which may be within the liquid layer but are typically near the top. Due to the bubble coalescence, we often observe similar holdup patterns to the experiments in terms of the cross-sectional holdup, however, the liquid does not cover the cross-section and thus does not conform to the definition of a slug. We have simulated conventional slugs in a simplified geometry without the interior pipe and a cell size of 1x1x1 mm (Fig. 3-4). The simplified case is best compared to simulation case # 6 as it has the same phase fractions, inclination, and mixture velocity.

The flow field (Fig. 3) shows the effect of phase mixing. At $t = 4.0$ s a massive wave has introduced gas into the lower liquid layer recognized by the light red patches. Ideally, in a VOF simulation, the domain should be refined until the flow is completely resolved. In a completely resolved flow, one of the visible results is that the smallest bubbles are resolved by several cells, which would reduce the large sections of cells in Fig. 3 which are neither red or blue and are represented by a mixture color. In such a refined mesh, if the contour range is reduced to 2, the phase field would be near identical to a larger contour range, because the majority of cells would be single phase, apart from the cells which contain an interface. As time progresses, the mixing increases, and gas bubbles permeate throughout the liquid, wave merging results in a naturally occurring slug at 13.0 s. Unfortunately, this mesh results in excess of 10 million cells/m if employed for our annulus, which is beyond our computational resources. As the small bubbles are introduced at very fine meshes, it is likely a grid independence test would result in a false positive. We have found the solution to be "mesh independent" in terms of pressure gradient and flow regime at around 400 k cells/m (Friedemann et al., 2019); at this stage, there are few bubbles, and the solution is near identical to both a 200 k and 500 k cells/m mesh in terms of statistical pressure and slug frequency behavior, true mesh convergence is likely reached at a much higher mesh density.

3. InterFoam and fundamental equations

InterFoam is a volume of fluid (VOF) type multiphase solver in OpenFOAM, and solves the continuity and momentum equations for an averaged fluid. One benefit of the VOF approach is that it saves computational time; however, by averaging the phases some information about phase behavior is lost. The averaging of the fluid properties is performed using conventional mixture rules based on the phase fraction within a cell. As an example, the mixture viscosity or phase-averaged viscosity is calculated as

$$\overline{\nu} = (1-\alpha)\nu_g + \alpha\nu_l. \tag{2}$$

In Eq. (2), α is the liquid fraction within a computational cell, while ν_g and ν_l are the gas and liquid viscosities. The phase fraction (α) is described as

$$\alpha = \begin{cases} 1 & \text{if cell is occupied by liquid} \\ 0 < \alpha < 1 & \text{if cell contains both gas and liquid} \\ 0 & \text{if cell is occupied by gas.} \end{cases} \tag{3}$$

α is 1 if the cell is filled with liquid, and 0 if filled with gas, and a fraction between 0 and 1 if both phases are present. The indicator function α is solved for in a modified advection equation (Eq. 4)

$$\frac{\partial\alpha}{\partial t} + \nabla\cdot\left(\alpha\overline{u}\right) + \nabla\cdot\left(u_c\alpha\left(1-\alpha\right)\right) = 0, \tag{4}$$

where the interface compression velocity, u_c, "compresses" the surface, in effect sharpening the interface. With phase-averaging implemented, and assuming incompressible flow, the governing continuity (Eq. 6) and momentum (Eq. 5) equations can be simplified as

$$\frac{\partial\overline{u}}{\partial t} + \nabla\cdot\left(\overline{u}\overline{u}\right) = -\frac{1}{\overline{\rho}}\nabla p + \nabla\cdot\left(\overline{\nu}\left(\nabla\overline{u} + (\nabla\overline{u})^T\right)\right) + g + \frac{F_s}{\overline{\rho}}, \tag{5}$$

$$\nabla\cdot\overline{u} = 0, \tag{6}$$

where $\overline{\rho}, \overline{\nu}$, and F_s represent mixture density, viscosity, and surface tension force, while $\overline{u}$ is the shared velocity field (Berberovic et al., 2009; Rusche, 2002). The calculation of the mixture components follows the

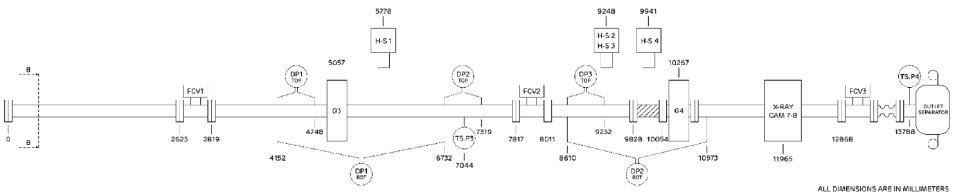

Fig. 4. Schematic of inclined Flow loop, HS = high-speed camera, G = Gamma densitometer, DP = Differential pressure transducer.

established mixture rule (Eq. (2)).

Lastly, A necessary modification to interFoam is introduced for the inclined simulations. InterFoam imposes a pressure discontinuity between periodic boundaries in an inclined domain due to the way gravity is included in the pressure equation.

$$p_d = p - \overline{\rho}\mathbf{g}\cdot\mathbf{x}, \tag{7}$$

$$\nabla p_d = \nabla p - \overline{\rho}\mathbf{g} - \mathbf{g}\cdot\mathbf{x}\nabla\overline{\rho}, \tag{8}$$

where $\mathbf{x}$ is the position vector. As is shown in Eqs. (7) & (8) there is a gravity term within the pressure equations. This gravity term creates a discontinuity for the periodic boundary condition between the inlet and outlet when the domain is inclined. In order to rectify this discontinuity, the boundary condition and momentum equation specification must be re-written from the modified pressure (p_d) to p, and the momentum equation must be further amended by adding the hydrostatic component back into the equation as a separate term. For a more thorough description of interFoam, the thesis by Rusche (2002) and Berberovic (2010) are the most complete descriptions of the solver that are publicly available.

4. Experimental setup

The experimental flow loops at IFE consists of a 50 and 15 m long loop in the horizontal and inclined configurations. The gas and liquid inlets are separated by a thin sheet which acts as a flow straightener, and the interior cylinder is held in place by spokes. The spokes and flow straighteners represent two geometrical elements that are not modeled in the simulations, and introduce some uncertainty to the experimental results through flow disturbances.

Along the test section, there are 3 broad-beam gamma densitometers (G) and 5 differential pressure transducers (DP). The gamma densitometers acquire holdup data at 50 Hz by measuring the incident beam attenuation. Using the fluid properties and attenuation coefficient, the liquid holdup within the test section is solved through Eq. (9) and (10). The intensity (γ) of an incident beam (γ_o) after passing through a fluid is

$$\gamma = \gamma_o exp(-\mu t), \tag{9}$$

where μ is the attenuation coefficient, and t the beam travel distance. For two-phase flows, the average cross-sectional holdup is calculated by

$$\alpha_l = \frac{log\left(\frac{\gamma_m}{\gamma_g}\right)}{log\left(\frac{\gamma_l}{\gamma_g}\right)}. \tag{10}$$

The ratio of the calibrated single-phase gamma intensities (γ_g,γ_l) and measured gamma intensity (γ_m) are used to calculate the liquid holdup within the test section. Single-phase measurements of the beam attenuation are used to determine the calibrated intensities through Eq. (9). The radiation intensity of the original incident beam is reduced exponentially as a function of the fluid thickness, distance traveled, and attenuation coefficient. The measurement gamma intensity is determined through the beam attenuation of the two-phase experiments.

5. Fluid properties and mixture velocities

The fluid properties and mixture velocities are reflected in the simulations as initial conditions and as a momentum-source (mixture velocity). The average pressure gradient over each measurement interval can vary, and for cases where the holdup fraction on either side of the pressure gradient measurement varies significantly an average of the readings are used for the simulations. Therefore, the initialized holdup fraction of the simulation may be slightly different from the values recorded in Table 1, which in turn will affect the simulated pressure gradient. For example, case #1; one measuring station has an average of 63% holdup while the next has 58.5%.

Table 1
Liquid holdup fraction, mixture velocity and superficial liquid velocity.

Case #	α	U_{mix} (m/s)	u_{sl} (m/s)
1	0.63	1.2	0.2
2	0.45	2.7	0.2
3	0.48	4.2	1.2
4	0.53	4.1	1.6
5	0.44	2.25	0.25
6	0.53	2.75	0.75
7	0.43	3.75	0.75
8	0.46	4.25	0.75
9	0.30	2.25	0.25
10	0.40	2.75	0.75
11	0.32	3.75	0.75
12	0.46	3.25	1.25

Table 2
Summary of fluid properties for cases 1–4 with sulphur hexafluoride (gas) and Exxsol D60 (liquid) in a horizontal eccentric annulus (E = 1.0).

Case #	ρ_l ($\frac{kg}{m^3}$)	ρ_g ($\frac{kg}{m^3}$)	ν_l ($\frac{m^2}{s}$)	ν_g ($\frac{m^2}{s}$)
1	801.3	24.2	$1.75{\cdot}10^{-6}$	$6.19{\cdot}10^{-7}$
2	801.1	24.3	$1.75{\cdot}10^{-6}$	$6.17{\cdot}10^{-7}$
3	803.0	25.7	$1.74{\cdot}10^{-6}$	$5.83{\cdot}10^{-7}$
4	802.1	26.4	$1.75{\cdot}10^{-6}$	$5.69{\cdot}10^{-7}$

Table 3
Summary of fluid properties for cases 5–8 with sulphur hexafluoride (gas) and Exxsol D60/Marcol 82 mixture (liquid) in a 4° inclined eccentric annulus (E = 1.0).

Case #	ρ_l ($\frac{kg}{m^3}$)	ρ_g ($\frac{kg}{m^3}$)	ν_l ($\frac{m^2}{s}$)	ν_g ($\frac{m^2}{s}$)
5	854.1	43.8	$2.61{\cdot}10^{-6}$	$3.42{\cdot}10^{-7}$
6	854.3	43.9	$2.62{\cdot}10^{-6}$	$3.42{\cdot}10^{-7}$
7	854.4	43.9	$2.62{\cdot}10^{-6}$	$3.42{\cdot}10^{-7}$
8	856.1	44.0	$2.62{\cdot}10^{-6}$	$3.41{\cdot}10^{-7}$

Table 4
Summary of fluid properties for cases 9–12 with sulphur hexafluoride (gas) and Exxsol D60/Marcol 82 mixture (liquid) in a vertical eccentric annulus (E = 1.0).

Case #	ρ_l ($\frac{kg}{m^3}$)	ρ_g ($\frac{kg}{m^3}$)	ν_l ($\frac{m^2}{s}$)	ν_g ($\frac{m^2}{s}$)
5	854.3	44.8	$2.60{\cdot}10^{-6}$	$3.35{\cdot}10^{-7}$
6	855.3	45.1	$2.62{\cdot}10^{-6}$	$3.32{\cdot}10^{-7}$
7	855.6	45.0	$2.61{\cdot}10^{-6}$	$3.33{\cdot}10^{-7}$
8	857.4	45.5	$2.61{\cdot}10^{-6}$	$3.30{\cdot}10^{-7}$

In addition to the summarized data in Table 1, the surface tension coefficient is 0.0285 N/m. The fluids used during the horizontal (1–4) and inclined (5–12) experiment cases[1] are all the same, but due to system pressure, the density and viscosity vary slightly as summarized in Tables -2–5. In addition, simulation cases 13–16 are composed using the basic information from experiment cases 5–8, in order to study the effect of an increased inclination.

[1] cases 1–12 correspond to experiment # 6005, 6008, 6089, 6106, 7048, 7053, 7054, 7059, 7185, 7190, 7191 and 7195 in the IFE database

Table 5
Liquid holdup fraction, mixture velocity and superficial liquid velocity.

Case #	f	h/d_h	regime
1	0.25	0.60	I
2	0.63	0.46	I
3	0.76	0.49	I
4	0.63	0.52	I
5	0.61	0.45	I
6	0.61	0.52	I
7	0.91	0.45	I
8	1.06	0.47	I/DB
13	0.61	0.45	I
14	0.61	0.52	I
15	0.92	0.45	I
16	1.07	0.47	I/DB

6. Flow regime prediction

There are only a few mechanistic models that can be applied uniformly to the 16 cases analyzed in the present work. One of these models is a unified model proposed in Shoham (2006) and builds upon models established by Taitel and Dukler (1976) and Barnea (1987). The proposed unified model is applicable for the full range of inclinations studied in this article and can be utilized to predict the flow regime of all cases. However, the model was originally intended for hollow pipes, and may therefore be sensitive to geometrical influences. In particular, this unified model is heavily dependent on the liquid height. Due to the interior cylinder, the liquid height in an annulus is drastically different than it would be in a hollow pipe. The reader should also note that the Barnea and Taitel models were designed the using units lbf, lbm and ft. Because there are no available unified models for flow regime prediction developed specifically for an annulus geometry, the proposed unified model represents one of the better methods for flow regime prediction. For a thorough description of the unified flow regime prediction model, the book by Shoham (2006) or publication by Gomez et al. (1999) offer an in-depth description of the model and the underlying methodology.

The Barnea unified model works under the assumption that there are 5 distinct flow regimes, Stratified (SS), intermittent (I), bubble (B), dispersed bubble (DB) and annular (A) flow. Because some flow regimes, such as churn flow, predominantly occur at very high inclinations, it is considered part of the intermittent regime of the unified model. Stratified-wavy (SW) was another flow regime, which was not included in the model but is considered a sub-regime of the stratified flow regime. The solution procedure can be summarized in a few simple steps. First determine the dimensionless parameters which depend on the geometry and fractional holdups. Thereafter using these dimensionless parameters, check the transition criteria sequentially for stratified to intermittent flow, intermittent to annular flow, and intermittent to bubbly and dispersed bubbly flow.

We compare the expected flow regimes from both the Taitel flow regime map and Barnea unified model, which is presented in Shoham (2006). The flow regime map by Taitel was created using a similar approach as the Barnea model, but is only applicable to a small range of inclinations from horizontal to inclined flows up to 10°. Further, the flow regime map only requires the calculation of the Froude number and a dimensionless number referred to as the equilibrium liquid height ($\widetilde{h_L}$), which is the liquid level (h_L) divided by the hydraulic diameter (d_h) to be utilized.

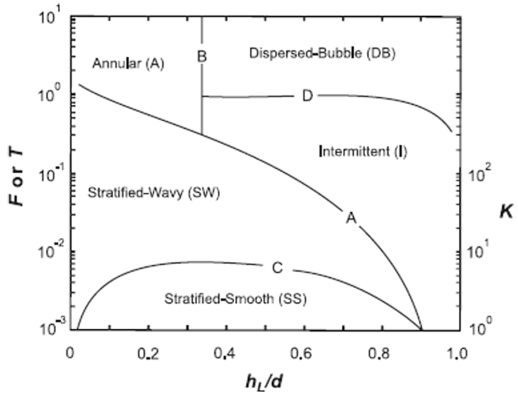

Fig. 5. Generalized flow regime map for horizontal and near horizontal inclinations, adapted from Taitel and Dukler (1976).

$$\widetilde{h_L} = \frac{h_L}{d_h}. \tag{11}$$

The equilibrium liquid height (Eq. 11) is determined using geometry assuming an equivalent hydraulic diameter for a hollow pipe. Together with $\widetilde{h_L}$, the Froude number (F), modified by the density ratio (Eq. 12) determines the transition points for the flow pattern map.

$$F = \sqrt{\frac{\rho_g}{\rho_L - \rho_g}}\ \frac{u_{sg}}{\sqrt{d_h g cos\theta}}, \tag{12}$$

where, the subscript s symbolizes superficial velocity. Calculating the two dimensionless numbers, the generalized flow regime map for horizontal and near horizontal inclinations (Fig. 5) can be utilized to predict the expected flow regimes for cases 1–8 and 13–16.

As described by the plotted data (Fig. 5), based on the generalized flow regime map, the expected flow regime for all low inclination cases are predicted as an intermittent flow regime except cases 8 and 16 which are on the transition line between dispersed bubbly and intermittent. In addition to cases 8 and 16, cases 1,2, and 5 are relatively close to the stratified wavy transition line. Due to the uncertainty caused by the annulus geometry when utilizing a flow regime model based on hollow pipes, we consider that these cases may be wavy.

In order to predict the remaining vertical cases, the full Barnea model, which is applicable from −90° to 90° is applied, and the low inclination cases were re-tested with this model. However, due to the similarities of the models, the expectation is that the low inclination cases will remain intermittent.

Please note that the transition test procedure must be done sequentially and in a specific order (Shoham, 2006). The test criteria is summarized below. If the reader is interested in a more in-depth description, Shoham (2006), Gomez et al. (1999) and Barnea (1987) are appropriate resources. The first transition point that the Barnea model analyzes is the stratified to intermittent transition. The criterion for the Barnea model is derived from a Kelvin–Helmholtz stability analysis and is also the same criterion utilized to create the transition boundary from stratified to intermittent in the Taitel flow regime map (Fig. 5).

$$F^2\left[\frac{1}{\left(1-\widetilde{h}_L\right)^2}\frac{\widetilde{u}_g^2\widetilde{S}_I}{\widetilde{A}_g}\right]\geqslant 1 \tag{13}$$

where $\widetilde{S}_I = \sqrt{1-(2\widetilde{h}_L-1)^2}$, $\widetilde{u}_g = \frac{u_g}{u_{sg}}$, and $\widetilde{A}_g = A_g/d_h^2$, and A_g is the cross-sectional area occupied by gas in the equilibrium state. If Eq. (13) is not true, then further analysis can establish whether the flow is stratified wavy. If the relationship is true, then the flow is either intermittent, bubbly, or annular. The next transition point considered is intermittent to dispersed bubbly. This transition requires the calculation of 4 terms for inclinations below 10° and 3 terms for higher inclinations.

The first term is the void fraction. In the unified model, the transition from intermittent to dispersed bubbly flow can only occur if the void fraction is less than 0.52 (Shoham, 2006), expressed as

$$1-\alpha < 0.52, \tag{14}$$

where α is the liquid holdup.

The unified model, proposes solving the void fraction by

$$\alpha_g = \frac{u_{sg}}{u_{sl}+u_{sg}} \tag{15}$$

If the void fraction is less than 0.52, the remaining transition criteria from intermittent to dispersed bubbly can be performed. The value of 0.52 is significant because it is the theoretical maximum packing of bubbles. Above this void fraction bubble agglomeration occurs, causing slug or intermittent flow (Gomez et al., 1999). After the void fraction criteria is passed, the maximum (d_{max}, Eq. 16) and two critical bubble diameters (d_{cd} & d_{cb}, Eqs. 17 & 18) are established. For the cases presented in this paper, both Eq.(15), and the measured void fraction was checked, and if either qualified for the criterion, we performed the transition tests. It should be noted, that this particular void fraction equation quite drastically overestimated the measured void fraction.

$$d_{max} = \left[0.725+4.15\left(\frac{u_{sg}}{u_m}\right)^{0.5}\right]\left(\frac{\sigma}{\rho_L}\right)^{0.6}\left(\frac{2f_m u_m^3}{d_h}\right)^{-0.4} \tag{16}$$

$$d_{cd} = 2\left[\frac{0.4\sigma}{(\rho_L-\rho_g)g}\right]^{0.5} \tag{17}$$

$$d_{cb} = \frac{3}{8}\frac{\rho_L}{(\rho_L-\rho g)}\frac{f_m u_m^2}{g cos\theta} \tag{18}$$

The transition to dispersed bubble flow occurs for low inclination flows when $d_{max} < d_{cd}\, and\, d_{cb}$, while it occurs for high inclination flows when $d_{max} < d_{cd}$ (Shoham, 2006).

The transition from annular to intermittent flow has two requirements, instability of the film near the wall and the liquid holdup (Gomez et al., 1999). Due to the formulation, the flow will remain intermittent if either condition is satisfied. The first condition is very straight forward, and states that there will not be annular flow if

$$\alpha > 0.24, \tag{19}$$

This condition coincides with the low inclination flow regime map (Fig. 5). At inspection, the transition (B) from the intermittent to annular flow regime occurs at $h_L/d_h \approx 0.35$, which equates to a liquid holdup of 0.25 which holds true for all of the vertical cases studied here. For the other transition requirement, the reader can refer to Shoham (2006) and Gomez et al. (1999).

The final transition considered in the unified model is the transition to bubble flow, which is separate from dispersed bubble flow, and occurs only below a critical void fraction of 0.25 and when the inclination is between 60 and 90°. Typically, the solution procedure given in Shoham (2006) requires the numerical solution of the void fraction; however, since the void fraction within our vertical domains is known, and it is always above 0.25, the cases are not expected to be bubble flow. At void fractions above 0.25, there is bubble agglomeration and transition to an intermittent flow.

$$u_{sL} = \frac{1-\alpha_g}{\alpha_g}u_{sg} - 1.53\left(1-\alpha_g\right)^{0.5}\left[\frac{g(\rho_L-\rho g)\sigma}{\rho_L^2}\right]^{1/4} sin\theta \tag{20}$$

When following the uniform model approach by numerically solving the void fraction based on the above relationship, the void fractions are within 0.2 of the measured void fractions, and well above the critical void fraction of 0.25. Based on the unified model, the 4 vertical cases

Table 6
Summary of Wave and slug frequencies for horizontal eccentric experiment cases (E = 1.0), with sulphur hexaflouride (gas) and Exxsol D60 (liquid).

Case #	Slug frequency (Hz)	Wave frequency (Hz)
1	–	0.49
2	–	0.65
3	1.16	–
4	1.72	–

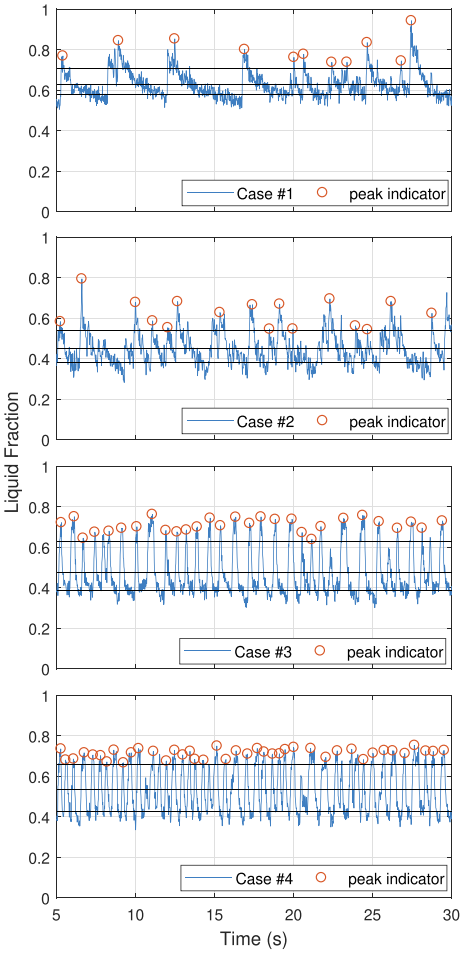

Fig. 6. Experimental liquid holdup as a function of time for horizontal eccentric annulus (E = 1.0) cases 1–4 with sulphur hexaflouride (gas) and Exxsol D60.

should all be intermittent flow.

As described above, the analysis suggests that all cases satisfy the conditions for intermittent flow. In the vertical cases, this may be churn flow as it is included in the intermittent phase. It is also possible to construct specific flow regime maps using the above relationships. In order to do so, several closure relationships are required. If the reader is interested in doing so Shoham (2006) contains an in-depth explanation of the procedure.

7. Summary of experimental results

The experimental results are split into three categories; horizontal (1–4), 4° (5–8), and 90° (9–12). The phase fractions and mixture velocities extracted from the experiments are utilized in the simulations to initiate and drive the flow (mixture velocity). Allowing the pressure gradients (Pa/m) and holdup transients to be simulated. In the following section, the slug and wave frequency of each case as well as the pressure gradient measured at the 4th DPT location are shortly summarized in order to give context to the computational results.

The entirely eccentric horizontal cases (1–4) summarized in Table 6 and shown in Fig. 6, consist of two wavy and two slug cases. The slug identification procedure follows the method outlined in Nuland (1999) and is built on utilizing thresholds to determine Taylor bubble and slug occurrences. Case 1 exhibits a few large long-period waves separated by a relatively calm state. Each successive case afterward has an increased frequency of waves or slugs, corresponding to an increased mixture velocity (Table 1). To confirm the flow regime of each case, visual data recorded at the third high-speed camera location 37 m downstream of the inlet is cross-referenced.

Each snapshot shown in Fig. 7, represent the case's dominant flow regime. Case #1, exhibits a few large waves separated by a region of calmer flow. Case #2 is dominated by large waves of varying amplitude, with significantly more phase mixing than Case #1, as shown by the darkening of the liquid. The darkening effect occurs when gas bubbles permeate throughout the liquid, also noticeable in the two slug cases (3 & 4). The two slug cases show an emerging slug (Case #3) together with the calmer region in front, and the Taylor bubble (Case #4) separating two slugs.

Table 7 summarizes the pressure gradient transients (Fig. 8) for cases 1–4. The three values recorded correspond to two threshold values (95 and 5%) and the mean pressure gradient. The two thresholds are defined, such that 5% of the data is below the minimum threshold and

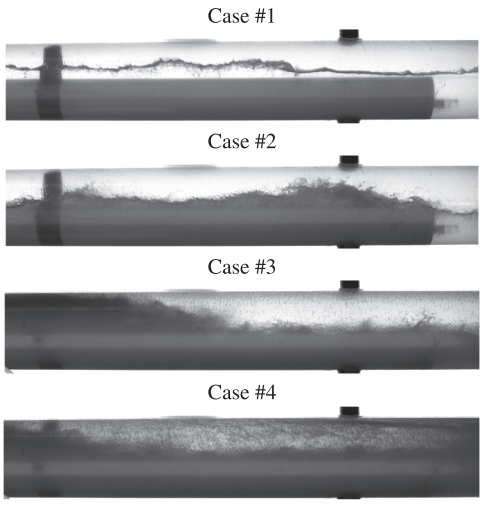

Fig. 7. Snapshots of flow regime for horizontal eccentric annulus experiments.

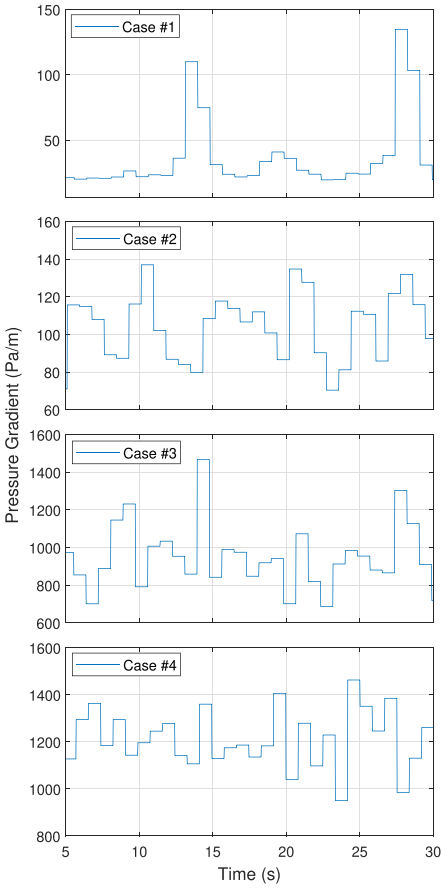

Fig. 8. Experimental pressure gradient as a function of time for horizontal eccentric annulus (E = 1.0) cases 1–4 with sulphur hexaflouride (gas) and Exxsol D60 (liquid).

Table 7
Pressure gradient summary for horizontal eccentric annulus experiment cases (E = 1.0) with sulphur hexaflouride (gas) and Exxsol D60 (liquid)..

Case #	5% (Pa/m)	mean (Pa/m)	95% (Pa/m)
1	15.29	36.27	98.20
2	74.90	102.95	136.95
3	696.43	961.00	1332.89
4	1031.45	1207.22	1405.03

Table 8
Summary of Wave and slug frequencies for 4° inclined eccentric annulus experimental cases (E = 1.0) with sulphur hexafluoride (gas) and Exxsol D60/ Marcol 82 mixture (liquid).

Case #	Slug frequency (Hz)	Wave frequency (Hz)
5	–	0.58
6	0.83	–
7	0.98	–
8	1.27	–

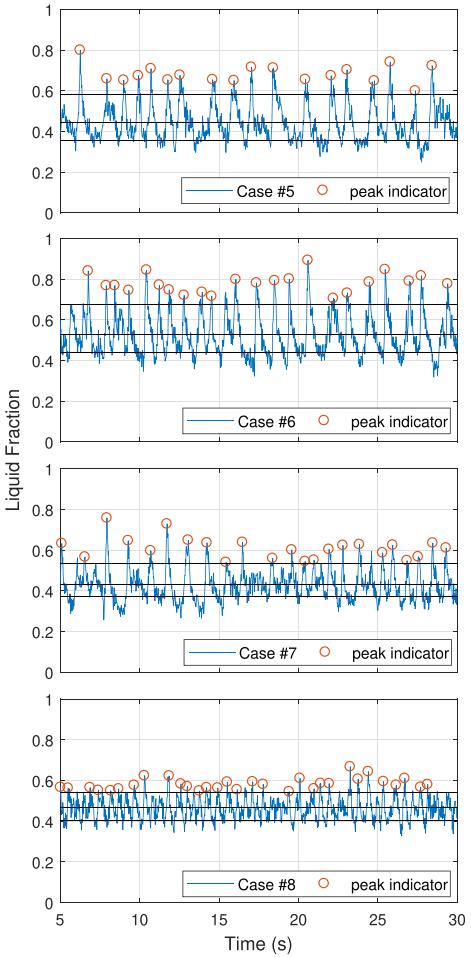

Fig. 9. Experimental liquid holdup fraction as a function of time for eccentric annulus (E = 1.0) cases 5–8 at 4° inclination with sulphur hexafluoride (gas) and Exxsol D60/Marcol 82 mixture (liquid).

5% above the maximum threshold. In general, the pressure gradient increases with increasing mixture velocity and with liquid holdup (Table 1); Case 4 has a 0.1 m/s lower mixture velocity compared to case 3, however, the pressure gradient is higher, in part due to a 0.05 fractional holdup increase. There is also a significant increase of several hundred Pa/m between the wave and slug flow cases.

The flow regime of the inclined cases (Table 8) is more complicated to analyze due to the increased amount of mixing, as shown by the darker images in Fig. 10; Case #5 is most likely dominated by large waves. The remaining three cases (6–8) are all likely slug cases, with some uncertainty with regards to case #8 due to the low peak holdup (Fig. 9); however, the combination of significant aeration and high-pressure gradient (Table 9) indicates case 8 is probably a high-frequency slug flow.

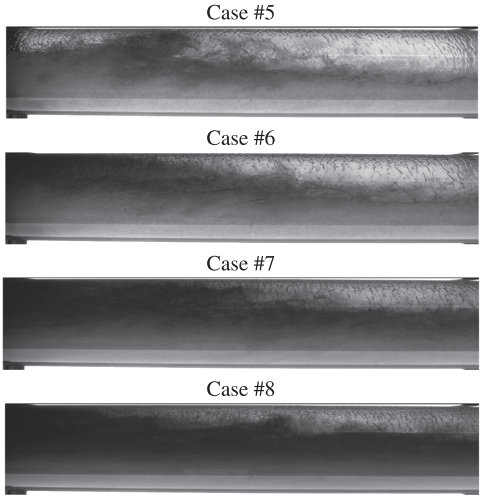

Fig. 10. Snapshots of flow regime for 4° inclined eccentric annulus experiments.

Table 9
Pressure gradient summary for 4° inclined eccentric annulus experimental cases (E = 1.0) with sulphur hexaflouride (gas) and Exxsol D60/ Marcol 82 mixture (Liquid).

Case #	5% (Pa/m)	mean (Pa/m)	95% (Pa/m)
5	261.4	497.2	802.7
6	645.6	1018.7	1375.5
7	850.9	1188.3	1612.3
8	1616.3	1791.0	1956.4

The most noticeable differences between the horizontal and 4° inclined cases (Figs. 7 & 10) is the increased darkening of the liquids in the inclined cases and increased pressure gradient when the holdup fractions and mixture velocities are similar. The leading cause for the darkening is the increased mixing caused by the higher mixture velocity and inclination. The inclination also introduces strong shear flows through backflow in the lower liquid layer, most prominent in cases 5 and 6. Carefully inspecting the case images, small gas bubbles are visible; by following the bubbles in a series of images counter-current flow (backflow) is observed.

Case #5 (Fig. 11), which is at 0.45 m/s lower U_{mix} than horizontal case #2 (Table 1) and nearly identical holdup, has an almost 5 times higher pressure gradient (Tables 7 & 9). The increased pressure gradient shows the pronounced effect of inclination on the pressure gradient caused due to the static head. From the respective holdup profiles (Figs. 6 & 9), we also notice that the flow regime is affected by inclination. The inclined flow is a wavy flow or perhaps a slug flow with a clear periodic trend, while the horizontal case is wavy with a less defined wave-period. As with the horizontal cases (Table 7), there are also clear pressure gradient trends with respect to mixture velocity and fractional holdup (Table 1) for the 4° inclined cases (Table 9).

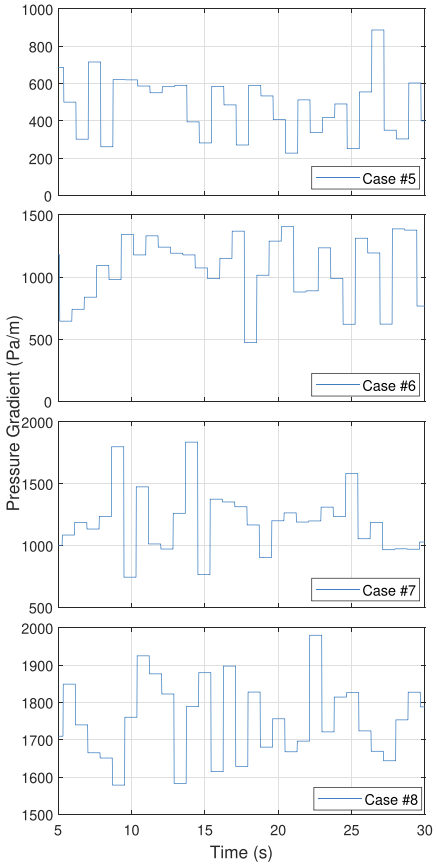

Fig. 11. Experimental pressure gradient as a function of time for eccentric annulus (E = 1.0) at 4° inclination with sulphur hexaflouride (gas) and Exxsol D60/ Marcol 82 mixture (Liquid).

Table 10
Holdup peak frequency for 90° inclined eccentric annulus experimental cases (E = 1.0), with sulphur hexafluoride (gas) and Exxsol D60/Marcol 82 mixture (liquid).

Case #	Frequency (Hz)
9	1.71
10	1.94
11	1.69
12	2.48

The frequencies identified for the 90° inclined eccentric annulus flow (Table 10) are obtained in the same way as for the wave and slug cases for the horizontal and 4° cases. However, the frequencies represent holdup peaks of the churn/wispy annular flow. All of the vertical cases are significantly harder to analyze due to the extreme amount of mixing and

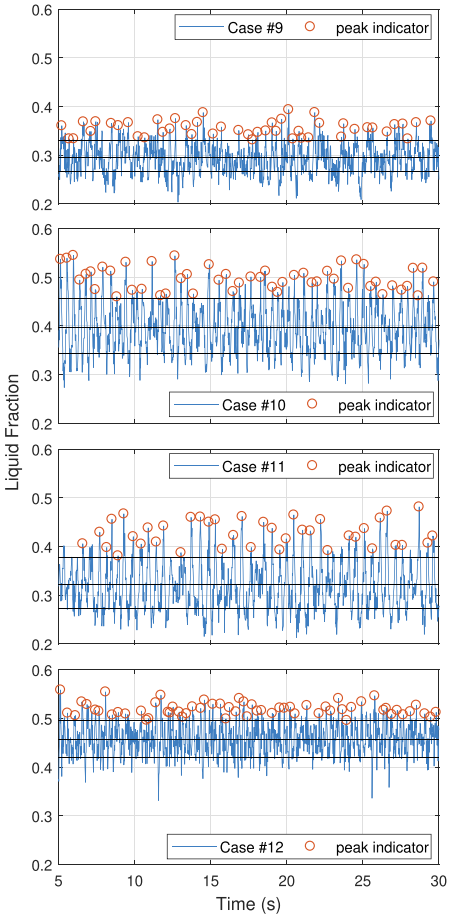

Fig. 12. Experimental liquid holdup as a function of time for eccentric annulus (E = 1.0) cases 9–12 with sulphur hexafluoride (gas) and Exxsol D60/Marcol 82 mixture (liquid).

liquid covering of the outer cylinder walls (Fig. 13). Therefore, flow regime identification is based on the liquid holdup (Fig. 12). Because the holdup is predominantly within the region of 30–50%, which is too high for conventional annular flow, and the walls are wetted by liquid, we believe the cases are most likely churn flow. There is also a possibility that the flow observed is a type of wispy annular flow with elongated bubbles of liquid within a gas core. In this case, the inside is presumably dominated by a gas core with flakes of liquid passing up through the gas layer.

The outer cylinder wall for cases 9–12 is covered in a liquid film (Fig. .13). The lighter regions are either sections where the liquid film very thin or wholly removed; most likely thin layers. The liquid film is observed moving slowly upward through a time-lapse; however, near the contact line between the interior cylinder wall and outer cylinder wall, there is a region of backflow. When backflow collides with a counter-directional flow, it may splash out into the interior and follow

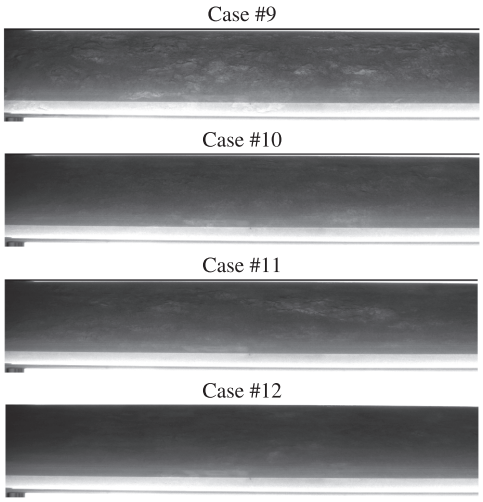

Fig. 13. Snapshots of flow regime for 90° inclined eccentric annulus experiments.

Table 11
Pressure gradient summary for 90° inclined eccentric annulus experimental cases (E = 1.0) with sulphur hexafluoride (gas) and Exxsol D60/Marcol 82 (liquid).

Case #	5% (Pa/m)	mean (Pa/m)	95% (Pa/m)
9	2281.0	2440.8	2586.7
10	3846.6	4054.7	4215.4
11	3357.4	3606.7	3857.1
12	5198.9	5274.1	5345.1

the core upwards. There are also regions where the liquid oscillates up and down, which is typical of churn flow.

The spread of the pressure gradient data is modest, with the vast majority of data points being within ±5% of the mean (Table 11 & Fig. 14). For churn flow, the pressure gradient is expected to be lower when large gas bubbles pass through the test section, and higher when the test section is mostly filled with liquid. The DPT test sections are approximately 1 m long, which may smear that data, therefore the pressure gradient data alone is insufficient to distinguish the potential flow regimes, and we will continue to classify the flow in the experimental cases 9–12 as churn flow.

Compared to the unified model and flow regime map, the experimental data agrees with the small caveat of cases 1,2 and 5. The experimental data indicates that these are wavy flows, while the flow regime map and unified flow model both predict intermittent flows. Small discrepancies are to be expected when using a model not distinctly designed for the geometry studied in this, and cases 1, 2 and 5 are as noted very close to the transition line between stratified wavy and intermittent flow.

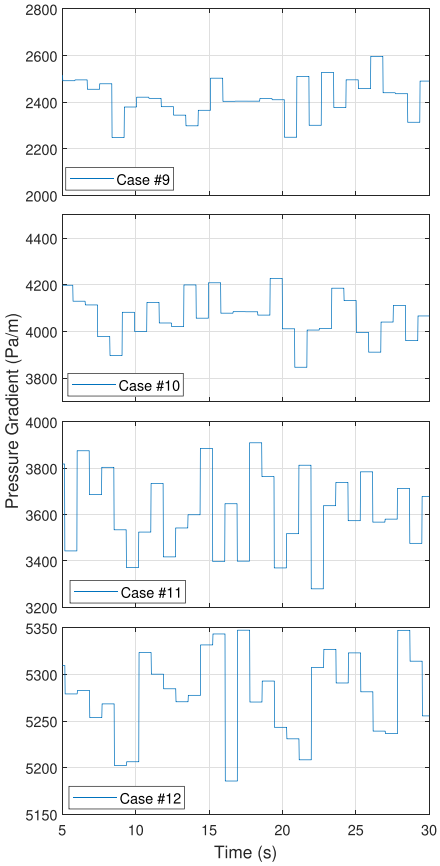

Fig. 14. Experimental Pressure gradient as a function of time for vertical eccentric annulus (E = 1.0) cases 9–12 with sulphur hexafluoride (gas) and Exxsol D60/Marcol 82 (liquid).

8. Simulation results

The experimental fluid properties, average holdup, and mixture velocities are extracted in order to initiate and drive the simulations. Simulation cases 13–16 are a replica of cases 5–8 at an increased inclination in order to study the effect of a small change of inclination. The fluid properties of each case mirrors the experimental cases and can be reviewed in Tables 1–4. The results are separated into four categories; horizontal, 4°, 90°, and 10° inclination. Following the established structure, the holdup results and key numbers are presented followed by the pressure gradient results. The solver used for the inclined simulations is a modified interFoam.

8.1. Simulated pressure gradient and holdup fraction results for horizontal eccentric annulus (E = 0.98) cases 1–4 with sulphur hexafluoride (gas) and Exxsol D60 (liquid).

Compared to the predicted flow regime using a unified model, the horizontal cases are in agreement for cases 3 and 4. Correspondingly, based on the holdup transients, the horizontal cases (Fig. 15) are in reasonable agreement with their experimental counterparts (Fig. 6), especially case 1, which is dominated by low-frequency waves. The three remaining horizontal cases are better compared through the simulation (Table 12) and experiment (Table 6) peak frequency. The key

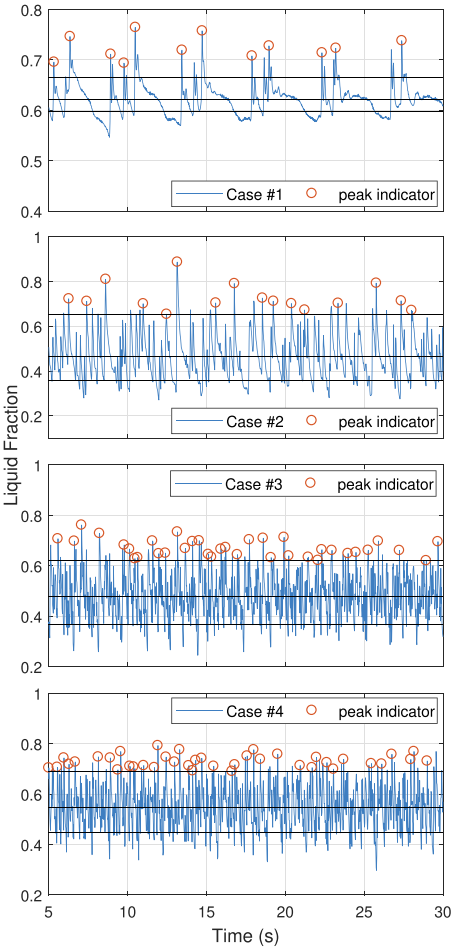

Fig. 15. Simulated liquid holdup fraction for horizontal eccentric annulus (E = 0.98) with sulphur hexaflouride (gas) and Exxsol D60 (liquid).

Table 12
Simulated wave and slug frequencies for horizontal eccentric (E = 0.98) cases 1–4 with sulphur hexaflouride (gas) and Exxsol D60 (liquid).

Case #	Slug frequency (Hz)	Wave frequency (Hz)
1	–	0.48
2	–	0.64
3	1.44	–
4	1.60	–

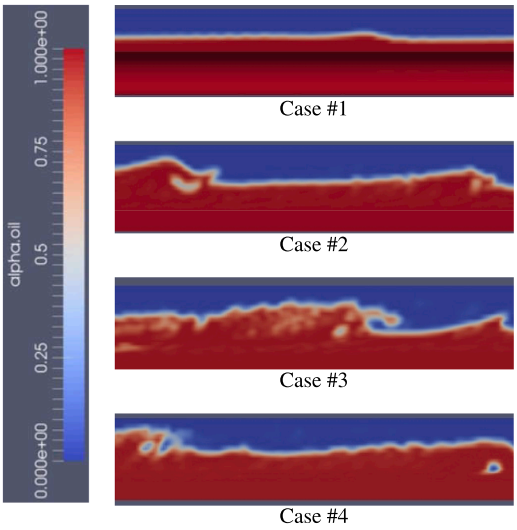

Fig. 16. Snapshots of flow regime for horizontal eccentric annulus simulations.

figures shows that the frequencies are within 0.3 Hz for all cases. Simulation cases 1 (wave), 3 (slug), and 4 (slug) appear to share a flow regime with the experiments. In regards to case 2, the cross-sectional holdup peaks are in the region of 0.7, with a few peaks at 0.8 or higher in both experiment and simulation, however, the simulations could be a proto-slug. The experiment flow regime images (Fig. 7) are cross-referenced with the streamwise slices of the simulated flow field to more accurately determine the flow regimes.

The simulated cases exhibit a near-complete lack of minor gas bubbles entrapped within the liquid. When the mesh is incapable of resolving small bubbles, they coalesce to form large gas bubble, as shown in case 4 (Fig. 1617) or remain outside of the liquid layer. Other factors such as surface tension treatment and turbulence modeling could also affect bubble formation. As shown by the holdup profiles, the simulated liquid holdup peaks (Fig. 15) are in line with the experimental cases (Fig. 6); however, due to a lack of gas penetration into the liquid, there are no conventional slugs observed in the simulations (Fig. 16). Therefore, the simulated slug structures are referred to as proto-slugs, proto-slugs resemble a short conventional slug and may or may not develop into a persistent slug. The image for case 1 is captured at the symmetry line, while the remaining images are an interior slice.

The most noticeable pressure gradient discrepancies in comparison with the experiments occur for cases 1 and 2 (Tables 13 & 14). These are low velocity cases, and a possible reason for the discrepancy is how turbulence is handled and generated in a VOF solver combined with the k-*omega* RANS model. A VOF solver functions by using an averaged imaginary liquid, the procedure could artificially induce turbulence throughout the fluids, while experiments have less turbulence in the liquid. Another alternative is the pressure solutions sensitivity to wall effects. Based on previous simulation campaigns (Friedemann et al., 2019), the 115 k cells/m mesh and solution method often over-predicts the pressure gradient.

When the simulations at a reduced eccentricity from Friedemann et al. (2020) but identical in all other matters are compared to these results, the pressure gradients for the fully eccentric simulations are reduced by 30–40% for all cases except case 2. Caetano (1985) found that the single-phase pressure gradient ratio for an annulus at E = 0.5 to be roughly 0.45 of an equivalent hollow pipe, while a fully eccentric annulus was roughly

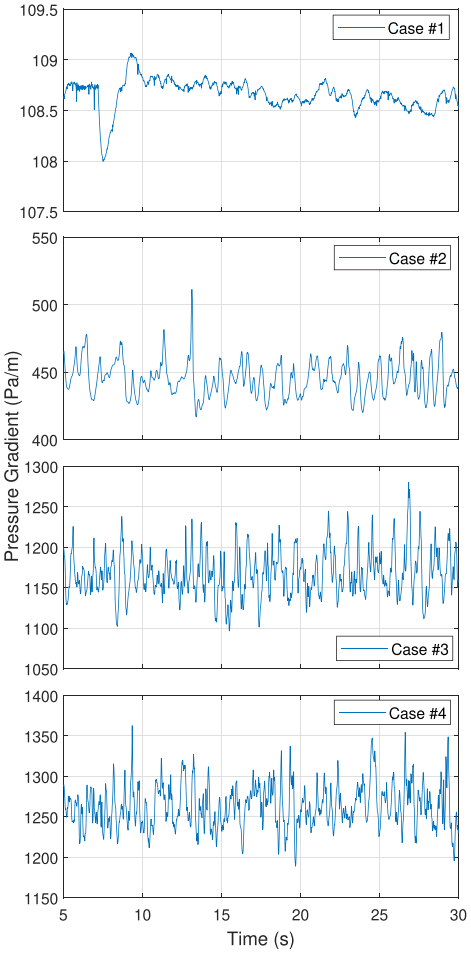

Fig. 17. Simulated pressure gradient as a function of time for horizontal eccentric annulus (E = 0.98) cases 1–4 with sulphur hexaflouride (gas) and Exxsol D60 (liquid).

Table 13
Simulated pressure gradient summary for horizontal eccentric annulus (E = 0.98) cases 1–4 with sulphur hexaflouride (gas) and Exxsol D60 (liquid).

Case #	5% (Pa/m)	mean (Pa/m)	95% (Pa/m)
1	108.5	108.7	108.8
2	425.9	445.1	467.8
3	1126.0	1167.5	1215.7
4	1223.8	1263.3	1307.9

Table 14
% difference between simulated pressure gradient and experimental pressure gradient for horizontal eccentric annulus simulation cases with E = 0.983.

Case #	5% (%)	mean (%)	95% (%)
1	610	196	10.7
2	469	332	242
3	61.7	21.5	−8.8
4	19.6	4.6	−6.9

Table 15
Simulated Wave and slug frequencies for 4° inclined eccentric annulus (E=.983) cases 5–8 with sulphur hexaflouride (gas) and Exxsol D60/ Marcol 82 mixture (Liquid).

Case #	Slug frequency (Hz)	Wave frequency (Hz)
5	–	1.04
6	1.36	–
7	1.24	–
8	1.72	–

0.25 of a hollow pipe for annulus with diameter ratios (D_i/D_o) of 0.5, in other words a 45% reduction of the pressure gradient as an effect of increasing the eccentricity from 0.5 to 1.0, while Ferroudji et al. (2019) found a decrease in pressure drop of roughly 17% when increasing the eccentricity from 0.6 to 0.9 for a power-law fluid or 25% when increasing from 0.3 to 0.9, also for a pipe diameter ratio of 0.5.

It is likely case #2 does not have a similar reduction due to the development of a different flow regime, with increased slug frequency in the previous publication. Compared to the experiments, the deviation

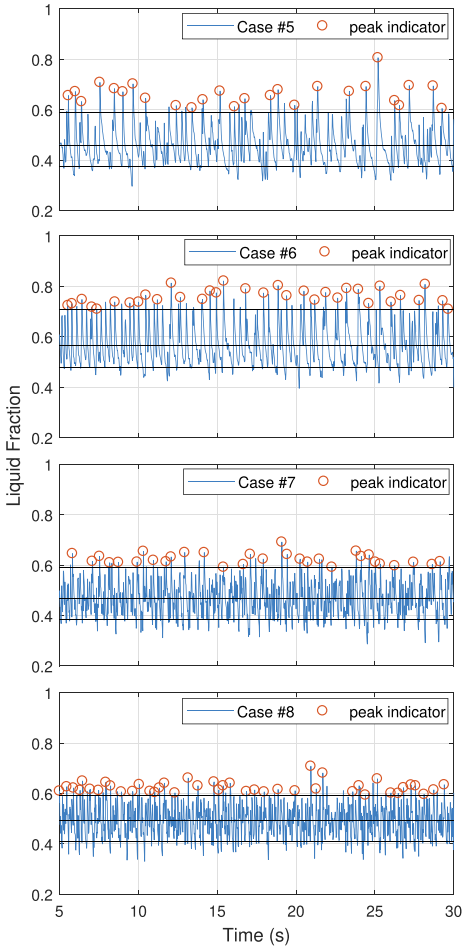

Fig. 18. Simulated liquid holdup fraction for eccentric annulus (E = 0.983) cases 5–8 at 4° inclination with sulphur hexaflouride (gas) and Exxsol D60/ Marcol 82 mixture (Liquid).

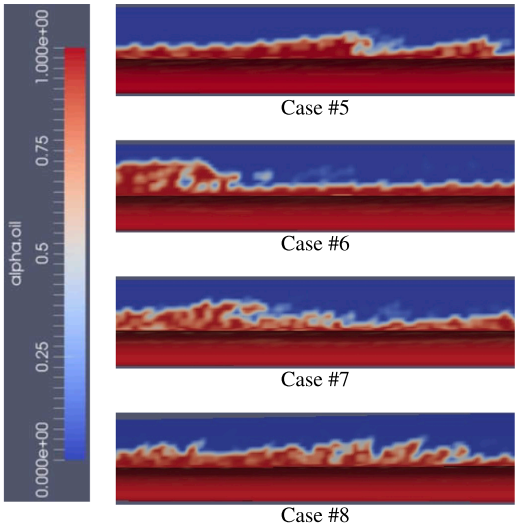

Fig. 19. Snapshots of flow regime for eccentric annulus simulations at 4° inclination.

from mean to either threshold is noticeably reduced. It will subsequently be shown that the relatively concentrated data persists for the inclined simulations. Compared to the experimental data, the simulated mean pressure gradient is within 4–22% for cases 3 and 4, while the two low velocity cases are off by 200–335%. There are several possible explanations for the over-prediction at low velocity cases, some of which were briefly mentioned, and needs to be further examined through other solution methods like an euler-euler multiphase approach, different wall functions, mesh densities, turbulence models or software such as Ansys Fluent.

8.2. Simulated pressure gradient and holdup fraction results for fully eccentric annulus (E = 0.983) at 4° inclination with sulphur hexaflouride (gas) and Exxsol D60/ Marcol 82 mixture (Liquid).

The wave and slug frequencies for cases 5–8 (Table 15) are consistently around 0.3–0.5 Hz higher than the experiments. Because the experiment time-series is 120 s, while the simulations are 30 s intervals with 25 s analyzed, some deviation is expected. For example, for the 25 s of experiment case 5 shown in Fig. 9 the wave frequency is 0.72 Hz, or 0.14 Hz higher than the data-set average, which indicates that even though there is a seemingly significant discrepancy, it is likely that within the full time-series there are periods where the simulations and experiments agree. The peak holdup for cases 5–8 (Fig. 18) are consistent with the experimental measurements (Fig. 9) with the exception the isolated holdup reading above 0.8 for experiment case #7. see Fig. 19-20.

Similarly to the horizontal cases (Fig. 16) there are no conventional slugs at 4° inclination (Fig. 10). Even when increasing the mesh density to 400 k cells/m no conventional slugs are produced. However, slugs are maintained for a prolonged period if they are part of the initial conditions, alternatively, created by initializing with a significantly lower

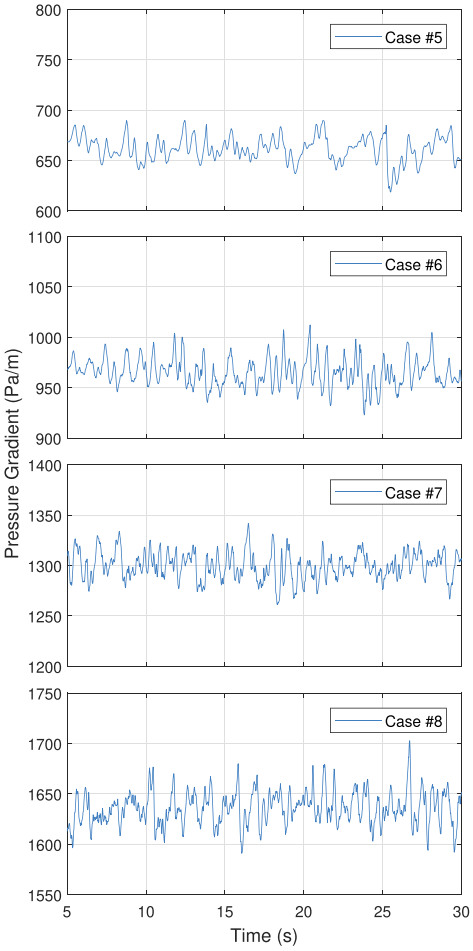

Fig. 20. Simulated pressure gradient as a function of time for an eccentric annulus (E = 0.983) at 4° inclination with sulphur hexaflouride (gas) and Exxsol D60/ Marcol 82 mixture (Liquid).

mixture velocity and then accelerating the flow. In both cases, the flow will eventually stabilize to the same proto-slug flow regime. The forced slugs which occur with the alternate initialization schemes are a transient occurrence. It is likely possible to achieve slug flow by altering the experimental surface tension. However, by altering the surface tension, the simulations are no longer attempted replicas of the experiments. see Fig. 24-28.

The lowest velocity case, case # 5 (Table 16 & 17), oscillates between 650 and 690 Pa/m. Remember that the horizontal cases that the simulations drastically over-predict the pressure gradient for the low velocity flows; however, the inclined simulations are likely in better agreement

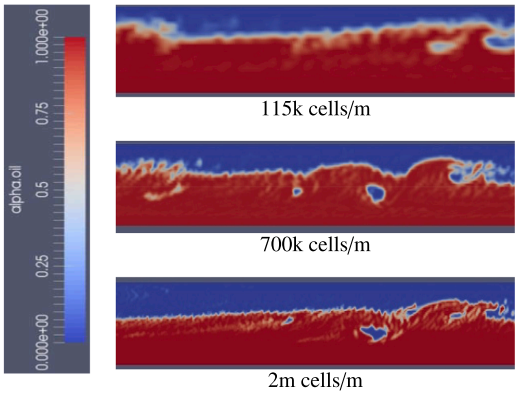

Fig. 21. Case #6, effect of mesh density on phase-mixing and bubble formation.

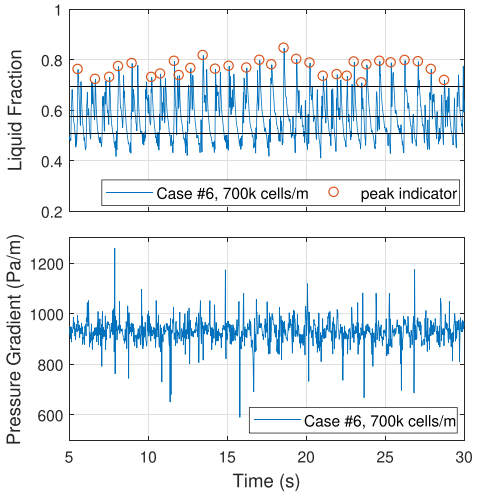

Fig. 22. Simulated liquid holdup fraction and pressure gradient as a function of time for 4° eccentric annulus case # 6 with 700 k cells/m and $E = 0.983$.

due to effect of the static head and higher mixture velocities, The simulated cases are within 35% of the experimental mean pressure gradient, and cases 6–8 are all within 10% of the mean. The threshold values are also better representation of the experiments. By increasing the mesh density for case #6 to 700 k (Fig. 22 and 2 million cells/m (Fig. 23) we noticed an increase in phase mixing (Fig. 21); however, there are no conventional slugs. see Fig. 30.

Fig. 21 shows that the number of light patches within the liquid (red) increases with mesh density, the increased gas entrapment is especially noticeable between 115 and 700 k cells/m. Unfortunately, even the 2 million cells/m mesh does not produce slug flow. Perhaps for a plug flow, which has less gas entrapment the mesh densities would be

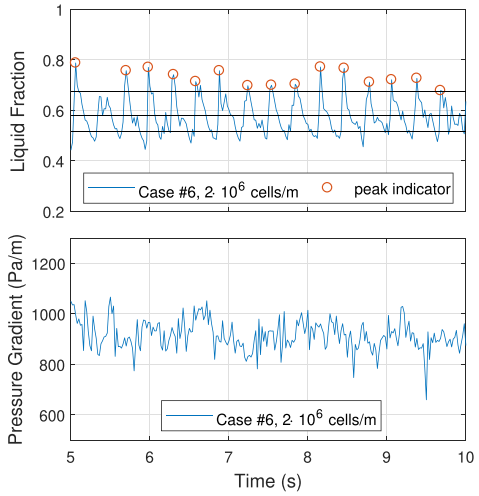

Fig. 23. Simulated liquid holdup fraction and pressure gradient as a function of time for 4° eccentric annulus case # 6 with 2 million cells/m and $E = 0.983$.

sufficient, which could be the reason why there are simulations of successful water–air slug flow, such as (Shuard et al., 2016). The higher surface tension between water and air results in less gas entrapment and spray from waves. It is also possible that phenomenological modeling of bubble formation, adaptive meshing or different turbulence models and boundary conditions would improve simulation accuracy.

Because the 2 million cells/m simulation requires such significant computational resources it was simulated for 10 s in a shortened domain. By analyzing similarly short periods for complete simulations it is found that the average and threshold values are well established even at a low sample count of 250.

As shown by Table 18, the mean pressure gradient decreases with mesh density, while the distance between mean and extreme values increases. It is appealing to theorize that the effect is triggered by increased phase-mixing, and ability to resolve minor structures and wall effects. Note that the frequency of the proto-slug structures is artificially increased for the finest mesh due to the shortened domain, an effect noted in both (Frank, 2005; Friedemann et al., 2019).

8.3. Simulated pressure gradient and holdup fraction results for eccentric annulus ($E = 0.983$) at 90° inclination with sulphur hexafluoride (gas) and Exxsol D60/Marcol 82 mixture (liquid)

The vertical cases behave differently than the $0-4^0$ cases. Mainly, due to the direction of gravity. Instead of encouraging layered flows with typical waves and slugs, vertical flow at these holdup fractions typically includes walls covered by a liquid film and a high velocity core. The resultant is a very high frequency holdup oscillation (Table 19) accompanied with a high mean pressure gradient (Table 20). The flow regime is difficult to determine by the holdup plots and externally images due to the liquid film wetting the cylinder walls. Compared to the experiments, the holdup peak frequency of the simulations is in reasonable agreement except for case 11, where the frequency is 0.47 Hz

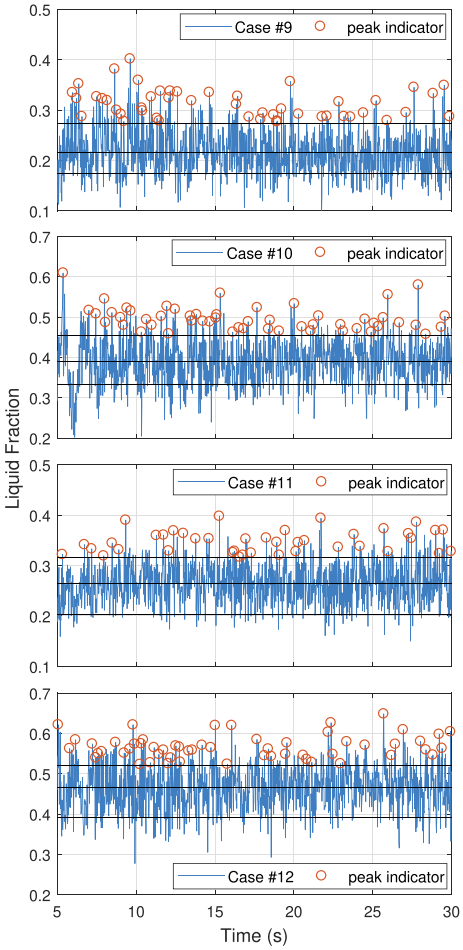

Fig. 24. Simulated liquid holdup fraction for 90° inclined eccentric annulus (E = 0.983) cases 9–12 with sulphur hexafluoride (gas) and Exxsol D60/Marcol 82 mixture (liquid).

higher than the experiment. For the remaining cases, the agreement is within 0.33 Hz.

From the experimental and computational (Figs. 25 & 26 imaging, a liquid film covering the outer cylinder and a gas core with flakes of liquid is visible, there is also a stream of gas passing through liquid near the contact line. The liquid film is periodically backflow, most prominently near the contact line between the two cylinders. The flow regime is most likely wispy annular or churn flow, possibly a transitional flow between the two flow regimes. The wispy annular flow regime was first identified by Bennett et al. (1965) and consists of a thin liquid film on the walls and long streaks or flakes of liquid within the gas core. The pressure gradient transients are referenced for further analysis.

The mean pressure gradients for the four vertical cases (Tables 20 & 21-22) are within 21% of and 36% of each threshold value. The pressure gradient can be sensitive to mesh density near the walls and contact line.

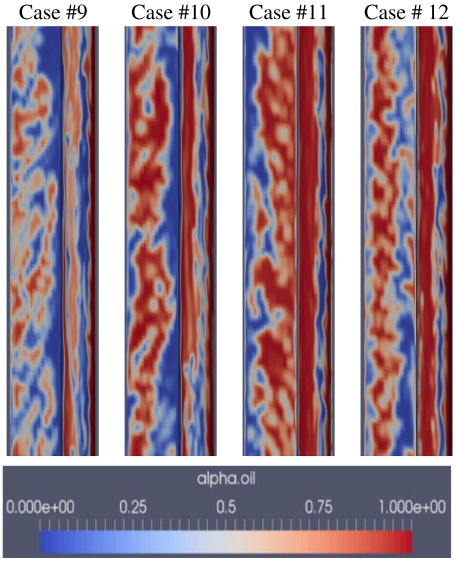

Fig. 25. Streamwise snapshots of simulated flow regime for vertical eccentric annulus cases.

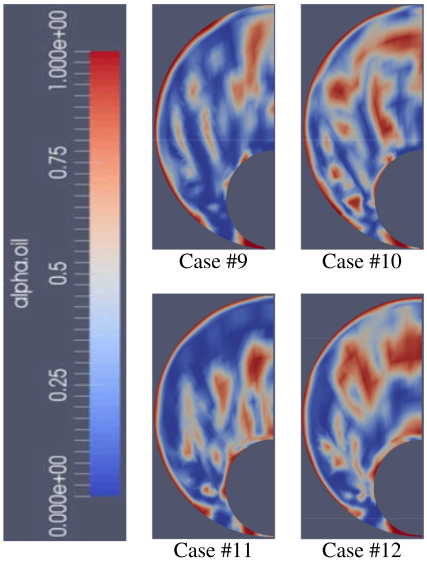

Fig. 26. Snapshots of cross-section of vertical eccentric annulus simulation cases.

In addition, any measurement error from the experiments related to, for example, the holdup fractions, will result in an error that follows through into the simulations as the initial conditions constrain the holdup fractions, and thereby affect the pressure gradient. Regardless, as

100

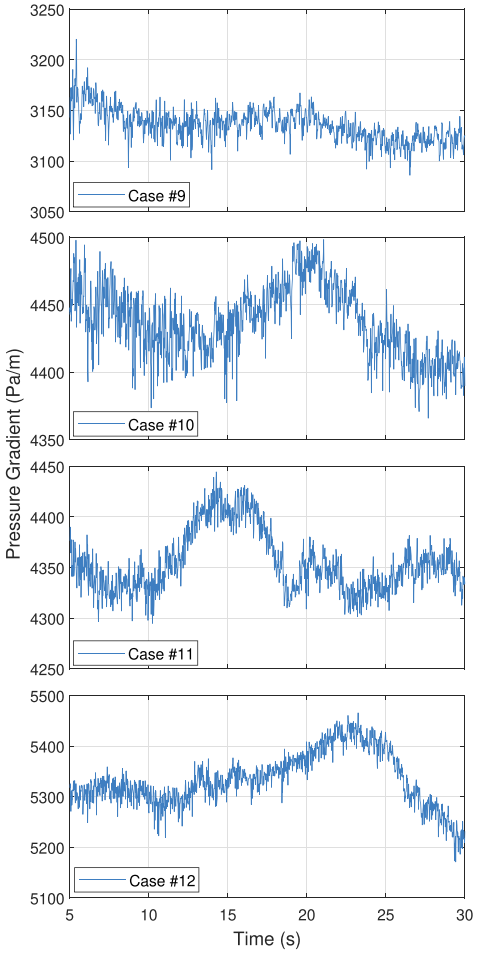

Fig. 27. Simulated pressure gradient as a function of time for 90° eccentric annulus (E = 0.983) cases 9–12 with sulphur hexafluoride (gas) and Exxsol D60/Marcol 82 mixture (liquid).

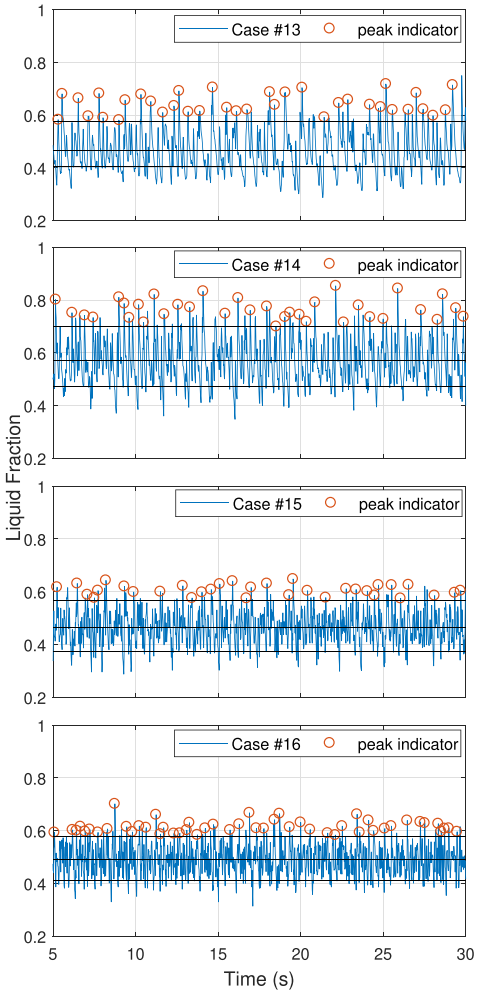

Fig. 28. Simulated liquid holdup fraction for 10° inclined eccentric annulus (E=.0983) cases 9–12 with sulphur hexafluoride (gas) and Exxsol D60/Marcol 82 mixture (liquid).

mentioned in Friedemann et al. (2019) interFoam in combination with a coarse mesh tends to over-predict the pressure gradient. see Table 23.

Concerning internal variations within the experiments themselves, by down-sampling to several distinct 25 s intervals, there are no noticeable changes in the experimental statistics. The simulations, on the other hand, for cases 10 and 11, appear to have two dominant frequencies (Fig. 27), with long-periodic oscillations of 100–150 Pa/m, which conforms to Hawkes et al. (2000) description of wispy annular flow. In order to confirm if there are multiple dominant frequencies, the time-series would have to be extended.

8.4. Simulated pressure gradient and holdup fraction results for eccentric annulus (E = 0.983) cases 13–16 at 10° inclination with sulphur hexafluoride (gas) and Exxsol D60/Marcol 82 mixture (liquid)

Cases 13–16 are the 10° versions of cases 5–9. The primary difference in flow development occurs for case # 13, which is reminiscent of a proto slug flow. The frequency of the proto slug is 1.4 Hz, which represents a significant increase of nearly 40% compared to the 4° case. The

Table 16
Summarized pressure gradient information for simulated 4° inclined fully eccentric annulus (E = 0.983).

Case #	5% (Pa/m)	mean (Pa/m)	95% (Pa/m)
5	641.9	661.5	681.7
6	941.2	965.3	989.7
7	1277.7	1299.7	1322.2
8	1609.5	1635.9	1661.7

Table 17
% Difference between simulated and experimental pressure gradient for 4° inclined eccentric annulus (E = 0.983) with sulphur hexaflouride (gas) and Exxsol D60/ Marcol 82 mixture (Liquid).

Case #	5% (%)	mean (%)	95% (%)
5	146	33.0	−15.1
6	45.8	−5.2	−28.0
7	50.2	9.4	−18.0
8	−0.42	−8.7	−15.1

Table 18
Summary of the pressure gradient and slug frequency for case # 6 at increasing mesh count and 4° inclination with E = 0.983

cells/m	5% (Pa/m)	mean (Pa/m)	95% (Pa/m)	f (Hz)
115 k	941.2	965.3	989.7	1.36
700 k	858.8	929.5	1000.4	1.24
2 m	830.7	916.5	1015.5	3.2
exp.	645.6	1018.7	1375.5	0.83

Table 19
Simulated holdup peak frequencies for 90° inclined eccentric (E = 0.983) with sulphur hexafluoride (gas) and Exxsol D60/Marcol 82 mixture (liquid).

Case #	frequency (Hz)
9	2.04
10	2.12
11	2.16
12	2.24

Table 20
Summary of simulated pressure gradient information for 90° eccentric annulus (E = 0.983) cases 9–12 with sulphur hexafluoride (gas) and Exxsol D60/Marcol 82 mixture (liquid).

Case #	5% (Pa/m)	mean (Pa/m)	95% (Pa/m)
9	3111.4	3135.6	3162.5
10	4395.0	4437.4	4480.5
11	4316.8	4355.0	4414.1
12	5248.7	5334.0	5426.6

Table 21
% Difference between simulated and experimental pressure gradient for vertical eccentric annulus cases 9–12.

Case #	5% (%)	mean (%)	95% (%)
9	36.4	28.5	22.3
10	14.3	9.4	6.3
11	28.6	20.7	14.4
12	0.96	1.1	1.5

Table 22
Simulated Wave and slug frequencies for eccentric annulus (E=.0983) cases 13–16 at 10° inclination with sulphur hexafluoride (gas) and Exxsol D60/Marcol 82 mixture (liquid).

Case #	Slug frequency (Hz)	Wave frequency (Hz)
13	–	1.40
14	1.40	–
15	1.32	–
16	2.0	–

Table 23
Summarized pressure gradient information for 10° inclined eccentric annulus simulation cases 13–16 (E = 0.983).

Case #	5% (Pa/m)	mean (Pa/m)	95% (Pa/m)
13	1020.6	1051.4	1078.7
14	1415.3	1453.7	1497.3
15	1678.7	1705.5	1730.8
16	2032.5	2061.9	2092.0

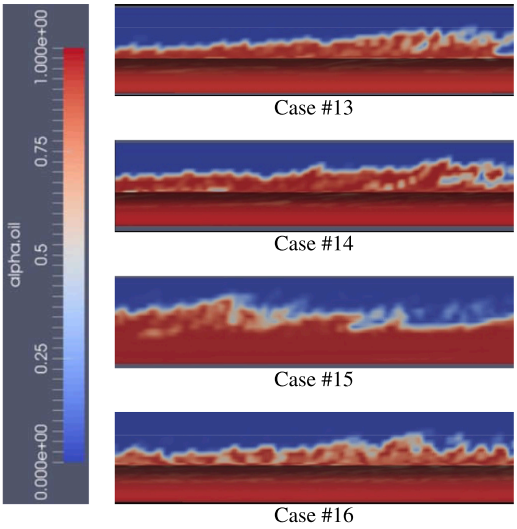

Fig. 29. Snapshots of simulated flow regime for 10° inclined eccentric annulus with E = 0.983.

added inclination results in steeper waves and higher peak holdup readings for all cases as well as higher peak frequency for most cases, although cases 14 and 15 show only minor frequency differences compared to the 4° cases.

The snapshots of the 10° inclined cases (Fig. 29) are consistent with the observations made for the 4° cases. However, there is an increased wave steepness and peak amplitude. There is also noticeably more spray ejected from the peaks of the waves and proto-slugs.

If the flow regimes across the 4° and 10^0 cases are consistent, there should be a pressure gradient increase dominated by hydrostatic forces. By increasing the inclination and enforcing a mixture velocity, the pressure gradient is increased in order to maintain the velocity. For sufficiently high inclination or sufficiently low Froude number, the gas velocity would most likely be significantly increased accompanied by a modest increase in the liquid velocity near the interface, while the lower liquid layer is stagnating or even moving backward.

The increase in mean pressure gradient from 4° to 10° is 389.9, 490.4, 405.8, and 426 Pa/m, respectively. The respective liquid holdup fractions are 0.45, 0.57, 0.46, and 0.49; by calculating the hydrostatic pressure component based on $P_{hydro} = \rho \cdot g \cdot L \cdot sin(\theta)$ and finding the pressure gradient by dividing by the domain length (L), then the expected change in mean pressure gradient due to hydrostatic pressure is 416.3, 515.5, 424.7 and 450.4 Pa/m. The difference between the actual increase and expected increase is within 18 to 27 Pa/m or 4 to 6.5%, this would be the change in the frictional pressure loss. Because these values are so close to the theoretical value, there is most likely only a minor effect of inclination on the flow regime in these cases.

9. Conclusions

In the present work, flow regime and pressure gradient behavior of

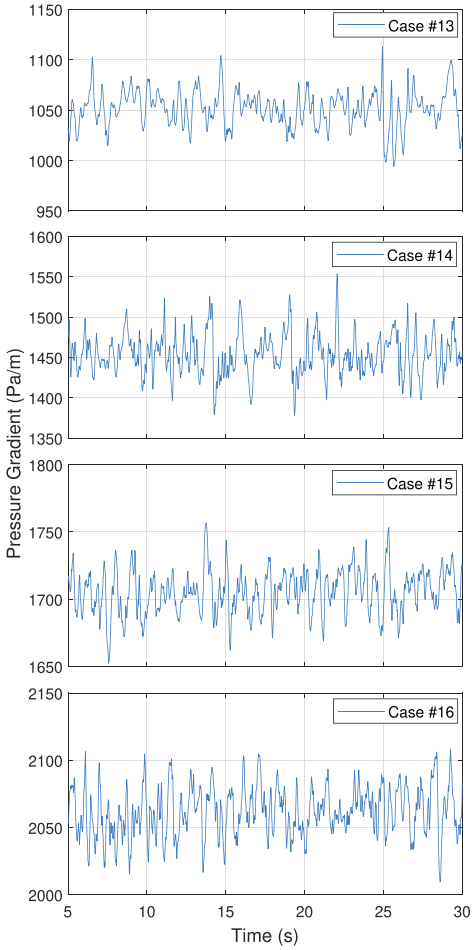

Fig. 30. Simulated pressure gradient as a function of time for eccentric annulus (E = 0.983) cases 13–16 at 10° inclination with sulphur hexafluoride (gas) and Exxsol D60/Marcol 82 mixture (liquid).

two-phase eccentric annulus simulations were analyzed and compared with experimental data at 0, 4, and 90° inclination, as well as flow prediction at 10° inclination.

- As found in previous work, conventional slugs are difficult to produce within this computational frame. There are several factors which can impede the development of slugs.
- The first possible contributing cause to the lack of the development of slugs, is the restricted fluid mixing and bubble permeation in the simulations. This issue can be overcome through excessively fine meshes, which can resolves minuscule gas bubbles entrapped within the liquid layer. We are aware that we can easily simulate slugs by artificially creating them through the initial conditions; however, that does not solve the issue of having them form naturally through physical interactions.
- Second, the surface tension affects the simulations, as several researchers have shown in hollow pipes when simulating water and gas. It is well known that the surface tension coefficient in such a flow is significantly higher than for the present studies, which lead us to believe that we could potentially force slugs by altering the surface tension. However, in doing so we would be deviating from attempting to replicate physical flows and instead creating imaginary compositions to a higher degree than the VOF mixture averaging procedure currently does. Other possible reasons for the lack of slug formation include, boundary conditions, the VOF model, and initial conditions.
- Running the simulations in a similar software program, such as Ansys Fluent, under the same conditions could help in understanding the root cause of the lack of conventional slugs.
- The horizontal cases (1–4) were previously studied within a partially eccentric domain (E = 0.5). Apart from case number 2, there was a reduced pressure gradient of 30–40% in the fully eccentric cases when compared to the simulations in the previous publication. This follows the established theory that the friction coefficient is reduced as eccentricity approaches 1 and is in line with existing literature that is available for single-phase flows.
- For the cases where the inclination was increased by 6 degrees (cases 13–16), there was only a small effect on the flow regime compared to cases 5–8.
- For the cases described above (5–8, 13–16), a pressure gradient increase within 6.5% of the theoretical increase due to hydrostatic pressure increase was detected. This 6.5% increase is due to the change in frictional pressure gradient and was found by subtracting out the hydrostatic component. We believe this indicates that the inclination change had little effect on the resultant flow regime of the 10° cases compared to the cases at 4°.
- Simulation cases 1–12 are compared to experiments of the same mixture velocity and phase fractions. For all cases except 1 and 2, the mean pressure gradient is within 33% of the expected behavior. While there is a larger discrepancy for the minimum pressure gradient, the maximum pressure gradient is within 30% for cases 3–12.
- The wave and slug frequencies for cases 1–12 are consistent with observed behavior of the experiments. All analyzed cases are within 0.5 Hz, which in some cases appears as a significant discrepancy. However, by down-sampling the experiments to 25 s, it is found that there are large variations of the wave and slug frequency in the experiments themselves, which include the sampled simulation frequency.
- Comparing the simulated and experimental flow regimes with predicted flow regimes using the Barnea unified model, and a Taitel flow regime map, the flow regime is correctly predicted for all but 3 experimental cases and 4 simulated cases.

Through the present study, the effect on the pressure gradient by increasing the eccentricity of the annulus is measured. In comparing these results to previously published work, it was found to be in line with existing literature and the simulations are in reasonable agreement with the experimental data, even at low mesh densities. Lastly the effect of a minor increase in inclination was determined to have only a small effect on the flow regime, and the increased pressure gradient due to inclination was nearly an exact match to the theoretical increase.

Declaration of Competing Interest

The authors declare that they have no known competing financial interests or personal relationships that could have appeared to influence the work reported in this paper.

Acknowledgements

This work is part of a larger project called Multiphase Flow in Concentric and Eccentric Annulus Spaces (project number 255481) and has been performed thanks to funding from the Research Council of Norway through the PETROMAKS2 programme.

References

Adachi, T., Imai, S., 2007. Three-dimensional linear stability of natural convection in horizontal concentric annuli. Int. J. Heat Mass Transf. 50, 1388–1396. https://doi.org/10.1016/j.ijheatmasstransfer.2006.09.029.

Axtmann, G., Rist, U., 2016. Scalability of OpenFOAM with Large Eddy Simulations and DNS on High-Performance Systems. https://doi.org/10.13140/RG.2.1.2395.8000.

Barnea, D., 1987. A unified model for predicting flow-pattern transitions for the whole range of pipe inclinations. Int. J. Multiph. Flow 13 (1), 1–12. https://doi.org/10.1016/0301-9322(87)90002-4.

Bennett, B.A.W., Hewitt, G.F., Kearsey, H.A., Keeys, R.K.F., Lacey, P.M.C., 1965. Paper 5: Flow visualization studies of boiling at high pressure. Proceedings of the Institution of Mechanical Engineers, Conference Proceedings 180 (3), 260–283. https://doi.org/10.1243/PIME_CONF_1965_180_119_02.

Berberovic, E., 2010. Investigation of Free-surface Flow Associated with Drop Impact: Numerical Simulations and Theoretical Modeling (Ph.D. thesis). Technische Universität; Darmstadt. URL: http://tuprints.ulb.tu-darmstadt.de/2319/.

Berberovic, E., Hinsberg, N.V., Jakirlic, S., Roisman, I., Tropea, C., 2009. Drop impact onto a liquid layer of finite thickness: Dynamics of the cavity evolution. Phys. Rev. E, Stat., Nonlinear, Soft Matter Phys. 79, 036306 https://doi.org/10.1103/PhysRevE.79.036306.

Caetano, E., 1985. Upward Vertical Two-Phase Flow Through an Annulus (Ph.D. thesis), The University of Tulsa.

Das, G., Das, P., Purohit, N., Mitra, A., 1998. Rise velocity of a taylor bubble through concentric annulus. Chem. Eng. Sci. 53 (5), 977–993. https://doi.org/10.1016/S0009-2509(97)00210-8.

Denton, J., 1963. Turbulent Flow in Concentric and Eccentric Annuli. Master's thesis;. The University of British Columbia. https://doi.org/10.14288/1.0105462.

Erge, O., Vajargah, A.K., Ozbayoglu, M.E., van Oort, E., 2015. Frictional pressure loss of drilling fluids in a fully eccentric annulus. J. Natural Gas Sci. Eng. 26, 1119–1129. https://doi.org/10.1016/j.jngse.2015.07.030.

Ferroudji, H., Hadjadj, A., Haddad, A., Ofei, T.N., 2019. Numerical study of parameters affecting pressure drop of power-law fluid in horizontal annulus for laminar and turbulent flows. J. Petrol. Explor. Prod. Technol. 9 (4), 3091–3101. https://doi.org/10.1007/s13202-019-0706-x.

Frank, T., 2005. Numerical simulation of slug flow regime for an air-water two-phase flow in horizontal pipes. In: The 11th International Topical Meeting on Nuclear Reactor Thermal-Hydraulics. Avignon, France.

Friedemann, C., Mortensen, M., Nossen, J., 2019. Gas-liquid slug flow in a horizontal concentric annulus, a comparison of numerical simulations and experimental data. Int. J. Heat Fluid Flow 78. https://doi.org/10.1016/j.ijheatfluidflow.2019.108437.

Friedemann, C., Mortensen, M., Nossen, J., 2020. Two-phase flow simulations at 0-4° inclination in an eccentric annulus. Int. J. Heat Fluid Flow 83.https://doi.org/10.1016/j.ijheatfluidflow.2020.108586.

Gomez, L.E., Shoham, O., Schmidt, Z.C., N.R., Brown, A., Northug, T., 1999. A unified mechanistic model for steady-state two-phase flow in wellbores and pipelines. Soc. Petrol. Eng.https://doi.org/10.2118/56520-MS.

Hamad, F., Khan, M., 1998. Natural convection heat transfer in horizontal and inclined annuli of different diameter ratios. Energy Convers. Manage. 39 (8), 797–807. https://doi.org/10.1016/S0196-8904(97)10010-3.

Hanks, R.W., Bonner, W.F., 1971. Transitional flow phenomena in concentric annuli. Ind. Eng. Chem. Fundamentals 10 (1), 105–113. https://doi.org/10.1021/i160037a018.

Harvel, G., Hori, K., Kawanishi, K., Chang, J., 1999. Cross-sectional void fraction distribution measurements in a vertical annulus two-phase flow by high speed x-ray computed tomography and real-time neutron radiography techniques. Flow Meas. Instrum. 10 (4), 259–266. https://doi.org/10.1016/S0955-5986(99)00008-4.

Hawkes, N., Lawrence, C., Hewitt, G., 2000. Studies of wispy-annular flow using transient pressure gradient and optical measurements. Int. J. Multiph. Flow 26, 1565–1582. https://doi.org/10.1016/S0301-9322(99)00104-4.

Hernandez-Perez, V., 2008. Gas-liquid two-phase flow in inclined pipes (Ph.D. thesis).

Hills, J., Chéty, P., 1998. The rising velocity of taylor bubbles in an annulus. Chem. Eng. Res. Des. 76 (6), 723–727. https://doi.org/10.1205/026387698525423.

Ibarra, R., Nossen, J., 2019. Investigation of oil-water flow in concentric and fully eccentric annuli pipes. Chem. Eng. Sci.: X 4. https://doi.org/10.1016/j.cesx.2019.100042, 100042, URL: http://www.sciencedirect.com/science/article/pii/S2590140019300498.

Iyer, S., Vafai, K., 1998. Buoyancy induced flow and heat transfer in a cylindrical annulus with multiple perturbations. Int. J. Heat Mass Transf. 41 (20), 3025–3035. https://doi.org/10.1016/S0017-9310(98)00053-2.

Julia, J.E., Hibiki, T., 2011. Flow regime transition criteria for two-phase flow in a vertical annulus. Int. J. Heat Fluid Flow 32 (5), 993–1004. https://doi.org/10.1016/j.ijheatfluidflow.2011.06.001.

Kalitzin, G., Medic, G., Iaccarino, G., Durbin, P., 2005. Near-wall behavior of rans turbulence models and implications for wall functions. J. Comput. Phys. 204 (1), 265–291. https://doi.org/10.1016/j.jcp.2004.10.018. URL: http://www.sciencedirect.com/science/article/pii/S0021999104004164.

Kelessidis, V., Dukler, A., 1989. Modeling flow pattern transitions for upward gas-liquid flow in vertical concentric and eccentric annuli. Int. J. Multiph. Flow 15 (2), 173–191. https://doi.org/10.1016/0301-9322(89)90069-4.

Kelessidis, V., Dukler, A., 1990. Motion of large gas bubbles through liquids in vertical concentric and eccentric annuli. Int. J. Multiph. Flow 16 (3), 375–390. https://doi.org/10.1016/0301-9322(90)90070-Y.

Kiran, R., Ahmed, R., Salehi, S., 2020. Experiments and cfd modelling for two phase flow in a vertical annulus. Chem. Eng. Res. Des. 153, 201–211. https://doi.org/10.1016/j.cherd.2019.10.012.

Liu, F., 2016. A thorough description of how wall functions are implemented in openfoam. In: Nilsson, H., (Ed.) Proceedings of CFD with OpenSource Software. URL: http://www.tfd.chalmers.se/hani/kurser/OS_CFD_2016.

Mizushima, J., Hayashi, S., Adachi, T., 2001. Transitions of natural convection in a horizontal annulus. Int. J. Heat Mass Transf. 44, 1249–1257. https://doi.org/10.1016/S0017-9310(00)00188-5.

Nikitin, N., Wang, H., Chernysenko, S., 2009. Turbulent flow and heat transfer in eccentric annulus. J. Fluid Mech. 638:95–116.https://doi.org/10.1017/S002211200900812X.

Nuland, S., 1999. Bubble fraction in slugs in two-phase flow with high viscosity liquid. In: Proceedings of the 2nd International Symposium on Two-phase Flow Modeling and Experimentation. Pisa, Italy. https://doi.org/10.1088/1757-899X/121/1/012018.

Ozar, B., Jeong, J., Dixit, A., Juliá, J., Hibiki, T., Ishii, M., 2008. Flow structure of gas-liquid two-phase flow in an annulus. Chem. Eng. Sci. 63, 3998–4011. https://doi.org/10.1016/j.ces.2008.04.042.

Ozbayoglu, A.M., Yuksel, H.E., 2012. Analysis of gas-liquid behavior in eccentric horizontal annuli with image processing and artificial intelligence techniques. J. Petrol. Sci. Eng. 81, 31–40. https://doi.org/10.1016/j.petrol.2011.12.008.

Ozbayoglu, E., Sorgun, M., 2010. Frictional pressure loss estimation of non-newtonian fluids in realistic annulus with pipe rotation. J. Can. Petrol. Technol. 49, 57–64. https://doi.org/10.2118/141518-PA.

Rusche, H., 2002. Computational fluid dynamics of dispersed two-phase flows at high phase fractions (Ph.D. thesis). Imperial College London; Exhibition Road, London SW7 2BX. URL: https://spiral.imperial.ac.uk/handle/10044/1/8110.

Shoham, O., 2006. Mechanistic modeling of gas-liquid two-phase flow in pipes. Soc. Petrol. Eng.

Shuard, A., Ben, Mahmud H., King, A., 2016. Comparison of two-phase pipe flow in openfoam with a mechanistic model. IOP Conf. Ser.: Mater. Sci. Eng. 121, 012018 https://doi.org/10.1088/1757-899X/121/1/012018.

Taitel, Y., Barnea, D., Dukler, A.E., 1980. Modelling flow pattern transitions for steady upward gas-liquid flow in vertical tubes. AIChE J. 26 (3), 345–354. https://doi.org/10.1002/aic.690260304.

Taitel, Y., Dukler, A., 1976. A model for predicting flow regime transitions in horizontal and near horizontal gas-liquid flow. AIChe J. 22, 47–55. https://doi.org/10.1002/aic.690220105.

Vaughn, R., 1963. Laminar flow of non-newtonian fluids in concentric annuli. Soc. Petrol. Eng. 3, 274–276. https://doi.org/10.2118/615-PA.

Wongwises, S., Pipathattakul, M., 2006. Flow pattern, pressure drop and void fraction of two-phase gas-liquid flow in an inclined narrow annular channel. Exp. Thermal Fluid Sci. 30, 345–354. https://doi.org/10.1016/j.expthermflusci.2005.08.002.

Yoo, J., 2003. Dual free-convective flows in a horizontal annulus with a constant heat flux wall. Int. J. Heat Mass Transf. 46, 2499–2503. https://doi.org/10.1016/S0017-9310(02)00539-2.

Yu, B., Kawaguchi, Y., Kaneda, M., Ozoe, H., Churchill, S., 2005. The computed characteristics of turbulent flow and convection in concentric circular annuli. part ii. uniform heating on the inner surface. Int. J. Heat Mass Transf. 48, 621–634. https://doi.org/10.1016/j.ijheatmasstransfer.2004.08.022.